University of South Florida
Scholar Commons

Graduate Theses and Dissertations   Graduate School

9-30-2010

Field-Coupled Nano-Magnetic Logic Systems

Javier F. Pulecio
University of South Florida

Follow this and additional works at: http://scholarcommons.usf.edu/etd

Part of the American Studies Commons

Field-Coupled Nano-Magnetic Logic Systems

by

Javier F. Pulecio

A dissertation submitted in partial fulfillment
of the requirements for the degree of
Doctor of Philosophy
Department of Electrical Engineering
College of Engineering
University of South Florida

Major Professor: Sanjukta Bhanja, Ph.D.
Shekar Bhansali, Ph.D.
Sudeep Sarkar, Ph.D.
Rudy Schlaf, Ph.D.
Aaron Stein, Ph.D.

Date of Approval:
September 30, 2010

Keywords: Magnetic Cellular Automata, Quantum Cellular Automata, Nano-Fabrication, Magnetic Force Microscopy, Micromagnetics

Dedication

To my late grandparents Elfa and Tiberio Lemos.

Acknowledgements

Table of Contents

List of Tables

List of Figures

Abstract

The following dissertation addresses the study of nano-magnetic devices configured to produce logic machines through magnetostatic coupling interactions.

The ability for single domain magnets to reliably couple through magnetostatic interactions is essential to the proper functionality of Magnetic Cellular Automata (MCA) devices (p. 36). It was significant to explore how fabrication defects affected the coupling reliability of MCA architectures. Both ferromagnetic and anti-ferromagnetic coupling architectures were found to be robust to common fabrication defects. Experiments also verified the functionality of the previously reported MCA majority gate [1] and a novel implementation of a ferromagnetic MCA majority gate is reported.

From these results, the study of clocking Magnetic Cellular Automata (MCA) interconnect architectures was investigated (p. 54). The wire architectures were saturated under distinct directions of an external magnetic field. The experimental results suggested ferromagnetic coupled wires were able to mitigate magnetic frustrations better than anti-ferromagnetic coupled wires. Simulations were also implemented supporting the experimental results. Ferromagnetic wires were found to operate more reliably and will likely be the primary interconnects for MCA.

The first design and implementation of a coplanar cross wire system for MCA was constructed which consisted of orthogonal ferromagnetic coupled wires (p. 68). Simulations were implemented of a simple crossing wire junction to analyze micro-magnetic dynamics, data propagation, and associated energy states. Furthermore, two systems were physically realized; the first system consisted of two coplanar crossing

wires and the second was a more complex system consisting of over 120 nano-magnetic cells. By demonstrating the combination of all the possible logic states of the first system and the low ground state achieved by the second system, the data suggested coplanar cross wire systems would indeed be a viable architecture in MCA technology.

Finally, ongoing research of an unconventional method for image processing using nano-magnetic field-based computation is presented (p. 79). In magnetic field-based computing (MFC), nano-disks were mapped to low level segments of an image, and the magnetostatic coupling of magnetic dipole moments was directly related to the saliency of a low level segment for grouping. A proof of concept model for two MFC systems was implemented. Details such as the importance of fabricating circular nano-magnetic cells to mitigate shape anisotropy, experimental coupling analysis via Magnetic Force Microscopy, and current results from a complex MFC system is outlined.

Chapter 1

Introduction

1.1 Motivation

As the term "nano" has become more mainstream, at times it would seem the neoteric phenomenology of nano-science has been whittled into a chic prefix which is often misused. The physical constraints of nano-dimensions create fundamentally unique behaviors of materials and particles thought to be thoroughly understood. For example, a material such as gold at macroscopic scales is chemically inert but when reduced to nano-particles can be used as an energetic catalyst, or carbon, when found in a nanotube structure exhibits ballistic electron transportation properties mimicking conductivity only found in superconducting materials. These are just two natural examples of nano-science that substantiates unique opportunities for the technological advancement of humanity and should not be lost in translation. The study and understanding of nano-phenomena presents a defining opportunity to fundamentally discover and alter the way "stuff" works.

The United States of America formally acknowledged the importance of Nanotechnology in 2000 with the creation of The National Nanotechnology Initiative (NNI), which defined Nanotechnology as "…the understanding and control of matter at dimensions between approximately 1 and 100 nanometers, where unique phenomena enable novel applications." The semiconductor technology sector is particularly

1

interested in nano-phenomena as it is directly related to the profit model of the industry. In 2003, the CEO of Intel Craig Barnett stated,

> "The importance of Moore's Law, and its promise of smaller, more powerful products built at lower cost, remains the focus of continuing investments by those in our industry who are determined to remain competitive. For Intel, the path is clear. The fundamental value of silicon innovation and integration is certain for future product generations ahead, as it continues to create customer benefits and serve as the foundation for outstanding new products."

Moore's law states that every 2 years the density of devices doubles and has held true since the prediction in 1965 [2], but it is nearing the end of its life due to quantum effects at critical scaling dimensions. This presents dilemmas for current CMOS technology, yet it also actualizes new opportunities to explore alternative novel technologies. Dr. Paola Gargini, the director of strategy at Intel, believes around 2015 hybrid chips will emerge with other technologies such as grafted nanotubes and novel materials [3]. Nano-electro-mechanical field effect transistors (NEMFET) and Carbon Nanotube Tunnel field effect transistors (CNTFET) are excellent examples of nanotechnology creating interesting alternatives to resolve issues of mainstream devices, such as CMOS. In the following paragraphs NEMFETs and CNTFETs are briefly discussed to emphasize how nanotechnology can provide creative solutions to issues with current technology.

As the dimensions of CMOS transistors continue to scale, parasitic leakage currents have become more problematic and are non-ideal for low power applications. A non-traditional approach to resolve sub-threshold leakage in CMOS transistors is the Nano-Electro-Mechanical Field Effect Transistor (NEMFET) [4-6]. A NEMFET uses a nano-

2

electro-mechanical transducer to convert electrical energy into mechanical displacement which is attached to the FET's gate electrode. When the gate voltage is off (V_G=0), the electrostatic forces between the FET's gate and the dielectric above the channel, pulls in the gate electrode into direct contact with the dielectric. This causes the channel to fully deplete, cuts current flow from the source to the drain, and becomes the *off* state of the NEMFET. To turn the device *on*, the gate voltage is increased, which reduces the depth of the depletion region and allows for current to flow from the source to drain. Once a threshold is reached, the gate voltage is sufficient to overcome the electrostatic forces and the gate breaks contact with the dielectric above the channel. This device demonstrates a sub-threshold swing smaller than 60mV/decade at room temperature, which is the fundamental limit of MOSFETs, and is ideal for low power applications. It is interesting to observe the likeness of the first 1947 transistor, which was a mechanically suspended point contact switch, and how its contemporary state-of-the-art counterpart NEMFET returns to those roots.

Similarly, Carbon Nanotube Tunnel Field Effect Transistors (Tunnel CNFET) provide solutions to issues such as thermally limited sub-threshold swing, source-drain leakage current, and higher device density when compared to traditional CMOS devices [7-9]. Carbon nanotubes have been heavily researched due to their unique properties, such as high strength, ballistic transportation, and the ability to mimic semiconductors. When designing a FET the semiconducting single wall carbon nanotube (CN) is particularly interesting. By altering the doping profile throughout the length of the nanotube such that a P-I-N (p-doping, intrinsic-doping, n-doping) junction is formed, a transistor can be created using the carbon nanotube as the channel. The CN is connected to a source, drain, and a gate similar to MOSFET device. By changing the voltage of the gate, the

3

field effect is able to bend the conduction/valence bands and reduce the band gap. Carriers are then able to use the quantum tunneling effect to tunnel from the conduction to valence band or vice-versa. The Schottky barriers between the contacts at the source/drain and the carbon nanotube are typically minimal and the energy barrier needed to be overcome is of the band gap in the carbon nanotube.

Both NEMFETs and CNTFETs provide alternatives to overcome physical design issues with field effect transistors, which are enabled by nanotechnology, and were specifically discussed to demonstrate solutions offered by nano-science. The scope and breath of nanotechnology is quite considerable and affects many aspects of humanity, from enhancing the structural properties of cement mortar through the use of nano-particles for construction [10], to the use of magnetic nano-particles for drug targeting and cancer therapy [11]. Using the unique properties of nanotechnology, the focus of this work is to demonstrate a logic paradigm that utilizes a ferromagnetic nano-structure as a logical switch in a fundamentally different magnetic computing machine.

1.2 Significance

In the past, there has always existed an alternative technology to continue the advancement of computational technology. From punch cards to vacuum tubes to bipolar transistors to current complementary metal oxide semiconductor field effect transistors; scientists and engineers have made great advancements in the computational power and physical minimization of logic devices. At the initial stage of many successor technologies, history has shown them to be inferior to their respective predecessor and often impractical to implement; but as the devices continued to be developed, the successor technology eventually provided greater benefits to industry and ultimately the consumer. Currently, conventional CMOS technology is predicted to

4

reach its full potential by 2015, after which there is no clear front runner to continue the rapid improvement of technology. The impact of CMOS technology is clearly evident by the public consumption of electronic devices from the late 1980s to the present day. The research presented in this dissertation explores a new computing paradigm where the single domain magnetic dipole moment of a ferromagnetic nano-structure is used as a logical switch. The nano-magnets are arranged to couple with one another to create larger complex networks of a magnetic computing machine and has been labeled by the industry as an emergent technology.

Every year an international consortium of experts from the technology sector, called the International Technology Roadmap for Semiconductor (ITRS), gather to provide a roadmap for the future with the sole purpose of identifying significant technologies to advance the industry. Companies such as Intel Corporation, Hewlett-Packard, Texas Instruments, and IBM Corporation, rely on this roadmap as a guide to help determine what significant technologies are materializing. In 2009, the ITRS Emerging Research Devices identified Magnetic Logic as an emerging technology and stated,

> "Nano-magnetic logic has potential advantages relative to CMOS of being non-volatile, dense, low-power, and radiation-hard. Such magnetic elements are compatible with MRAM technology, which can provide input-output interfaces. Compatibility with MRAM also promises a natural integration of memory and logic. Nano-magnetic logic also appears to be scalable to the ultimate limit of using individual atomic spins" [12].

Detailed within is the study of that fundamental shift from the displacement of the electron as a basic switch, as found in transistor technology, to using the intrinsic spin of the electron to create a switch for logic. By fabricating ferromagnetic structures at nano-

5

dimensions a unique phenomenon occurs, the formation of a single magnetic domain (as opposed to multiple domain structures found at larger scales). This distinct magnetic state, which occurs only at the nano scale, presents unique opportunities to create a new type of computation machine based on the interaction of magnetic dipole moments. Magnetic logic exhibits extraordinary innovation possibilities, such as the potential to scale the size of a magnetic switch down to an atom, and could conceivably be the next significant advancement in computational logic.

1.3 Contributions

The use of nano-phenomena at the device level is relatively modern, and the use of nano-magnetism as a logical switch in computation is even earlier in its development. Therefore, the intention of this study was to simulate, implement, and test fundamental aspects of different magnetic logic systems. In particular, the focus was on the interaction between neighboring magnetic cells and how several factors, such as surface roughness or coupling architectures, affected nano-magnetic systems. Within this study, not only were previously reported pioneering results verified [13, 14], but the design, simulation, fabrication, and testing of novel nano-magnetic logic systems under various conditions were explored. Specifically the following contributions are detailed:

- The effect of size, surface, and shape irregularities of rectangular nano-magnets and the associated magnetostatic coupling reliability in Magnetic Cellular Automata (MCA) was analyzed (p. 36). The first implementation of a ferromagnetic majority gate, as well as two ferromagnetic majority gates feeding into a third ferromagnetic majority gate was presented. This was the largest known logic circuit demonstrated in MCA. The investigations demonstrated a highly predictable interaction of ferromagnetic and anti-

6

ferromagnetic coupling and a robustness to nominal fabrication defects associated with bottom up fabrication techniques.

- The first direct comparison of magnetic frustrations for ferromagnetic and anti-ferromagnetic MCA wires under external magnetic clocking fields in the in-plane hard axis, out-of-plane hard axis, in-plane easy axis, and spinning magnetizing field was experientially investigated (p. 54). Simulations were also implemented to attain the magnetic energy associated with magnetic frustrations and correctly coupled ground states. The results showed that ferromagnetic wires were able to mitigate magnetic frustrations better than anti-ferromagnetic wires and suggest out-of-plane magnetic fields as a possible clocking solution.

- The design, implementation, and testing of a novel ferromagnetic coplanar crossing wire systems was also presented (p. 68). The simulation of two ferromagnetic wires intersecting at a 90 degree angle has been discussed as well as the experimental implementation of two coplanar crosswire systems was reported. The novel crosswire system was found to be functional and offered a unique architecture for Magnetic Cellular Automata.

- The analysis of a unique Magnetic Field-Based Computing (MFC) system consisting of nano-magnetic disks to implement perceptual grouping of segmented edges through magnetic energy minimization for image processing was explored (p. 79). A proof of concept was explained and fabricated. The results showed that the circular disk can indeed be used to establish a saliency between edges of an image by exhibiting coupling along a particular magnetization direction. This can reduce a computational

7

bottleneck found in the perceptual organization process of grouping segments in computer vision.

These contributions helped to bolster the foundation of magnetic computational devices and provided perspective to the feasibility of realizing magnetic logic. Potential benefits of using magnetism for computation range from the prospect of ultra-low power devices for mobile applications to radiation tolerant circuitry for space exploration and other extreme environments.

1.4   Outline of the Dissertation

The outline of this dissertation is as follows:

- Chapter 2 Nano-Magnetic Systems reviewed current state-of-the-art nano-magnetic systems.

- Chapter 3 Fabrication of Nano-Structures via Electron Beam Lithography provided an overview and details of the Electron Beam Lithography fabrication process used in the physical realization of the magnetic nano-structures.

- Chapter 4 Introduction to Single Domain Nano-Magnets for Cellular Automata investigated rectangular single domain magnetic structures and discussed how physical parameters of fabrication, such as defects, affect the coupling interaction between neighboring cells. MCA majority gates structures are also discussed.

- Chapter 5 Magnetic Cellular Automata Interconnects discussed ferromagnetic and anti-ferromagnetic wire architectures for MCA under various external

8

magnetic clocking fields. Details on the ability of the wire architectures ability to mitigate frustrations were discussed.

- Chapter 6 Magnetic Cellular Automata Coplanar Cross Wire Systems detailed the design and implementation of a novel cross wire system that could intersect on the same device plane without undesired cross talk.

- Chapter 7 Magnetic Field-Based Computing for Image Processing explored the proof of concept and physical implementation of mapping the quadratic energy minimization of coupled dipole moments to the maximization of the quadratic edge affinity in the grouping process of perceptual organization.

Chapter 2

Nano-Magnetic Systems

2.1 Introduction

Nano-magnetic systems have recently shown great promise in the advancement of logic and memory. Novel emerging magnetic systems have been reviewed in the following sections. In particular, Magnetic Cellular Automata was discussed in great detail as it demonstrated very promising results such as scalability, room temperature operation, and functioning logic components.

2.2 Magnetic Cellular Automata

In Cellular Automata (CA), a basic cell has distinct enumerated states which are determined by its current state and the state of its neighbors. These cells are positioned such that direct neighbors will influence and change each other's current state. A good example of a cellular automaton is John Conway's Game of Life [15, 16]. Quantum Cellular Automata, or QCA, is a flavor of CA in which the intrinsic and extrinsic properties of the cell(s) are based on the quantum effects of an electron(s). An interesting fact of CA is that it is not limited to a specific technology; meaning that there are several physical implementations of a CA cell which embody the electron differently and make use of distinct quantum effects. Currently, there are three prominent variants of CA; Magnetic, Electronic, and Molecular [17-42]. The beauty of CA is that each cell is a self-contained element, needing no external energy to maintain a state. The desired state will always be one of the possible energy minimum configurations of the cell.
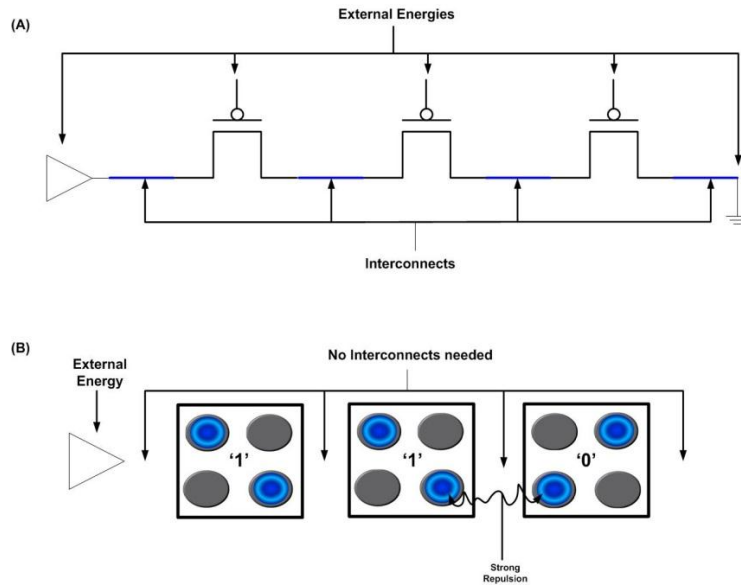
Figure 2-1 (A) is a diagram of transistors in series which depicts various external energies and interconnecting wires. Transistors require a constant energy supply to operate which is not necessary for QCA. (B) is an abstract representation of a QCA wire. The leftmost cell can be considered a state of '1' and the rightmost cell state '0'. The external source forced the leftmost cell to change its state to a '1' which forced the neighboring center cell to a logical '1'. The last rightmost cell, which is a '0' and will eventually change to a logic '1' because of the coupling force experienced from the neighboring cell.

There is no need for constant power to operate a CA system; external energy is only provided during switching of states, making CA an inherently low power system. Another excellent characteristic of CA is that it is a lead-less system, meaning there is no need for physical interconnects between all of the CA cells. Cells interact with neighbors via coupling forces which depend on the particular CA schema. This significantly reduces the already stringent requirements to fabricate any real nano-scale device. Figure 2-1 depicts a simple comparison of transistor and QCA technologies. Thus far, of the various CA schema, only Magnetic QCA has been able to demonstrate successful operation at room temperature [43] [44].

In Magnetic Cellular Automata (MCA), a basic cell is a nano-magnet; these magnetic cells are arranged in various grid-like fashions to accomplish computing. Cells in MCA

11
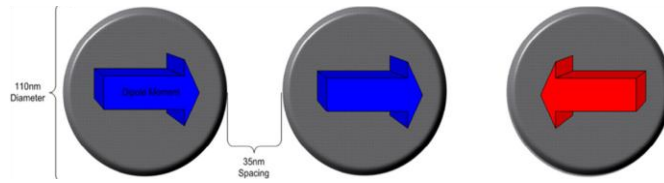
Figure 2-2 is a depiction of Cowburn's *et al.* circular MCA chain. The leftmost magnetic dot can be assumed to be a logical '1', while the rightmost can be assumed to be a logical '0'. In this wire the two leftmost magnetic dots have coupled. Assuming information is being driven from left to right, the final dot which has a state of '0' will flip to a logical '1' to minimize local magnetic energies.

are enumerated based on their single domain magnetic dipole moments and are inherently energy minimums. The single domain phenomenon only occurs in nano-scale magnets, and if engineered properly can reduce the cell's coercivity. This enables lower magnetic fields to alter the magnetic moment of a cell and provides desired switching characteristics. Two distinct and significant advancements in MCA have been made and are summarized in following subsections.

2.2.1 Single Domain Nano-Dots

In this scheme, a computing network is created by placing an elongated elliptical input dot followed by circular dots to form a wire as shown in Figure 2-2 [43, 45-52]. The elliptical input dot requires a greater magnetic field to change states than the circular dots due to the shape anisotropy. Once the state of the input dot has settled, it is propagated down the circular MCA wire. The input dot's state is set to a logical '1' or '0' by applying a single magnetic field pulse along the wire of dots at +300 Oe (returning to 0 Oe) or -300 Oe (returning to 0 Oe), respectively. To ensure that the magnetic pulse used to set the input dot did not set the circular dots states as well, the same magnetic pulse of ±300 Oe was sent along the wire without the presence of the input dot. The

12
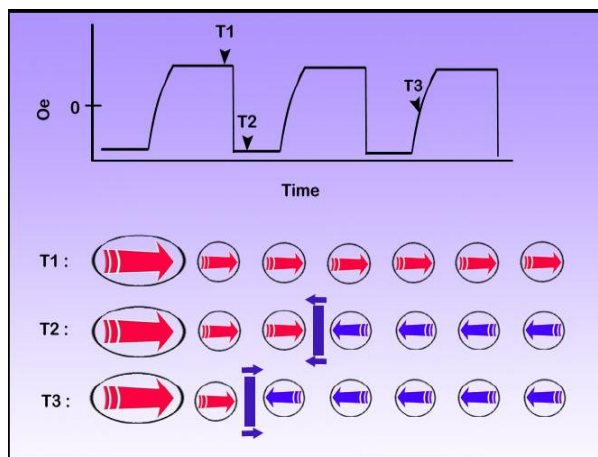
Figure 2-3 shows the operation of a chain of circular nano-dots propagating information. The graph depicts an oscillating external magnetic field with a -10 Oe bias which is used to drive information along the wire. At time T1, the majority of the circular wire has followed suit with the larger elliptical input dot. At T2, the negative phase of oscillation combined with the bias has sufficient energy to reverse the state of the circular wire by propagating a soliton. At time T3, the soliton has begun to move forward along the chain during the positive phase of oscillation of the applied field.

dipole moments of the circular nano-dots were not uniformly aligned to the external field, which ensured the propagation of information was due to the magnetostatic coupling forces and not the external field applied to set the input dot. A weak oscillating magnetic field of ±25 Oe at a 30Hz frequency, combined with a -10 Oe bias magnetic field was also applied to the entire network of dots to propagate the state of the input dot down the wire of circular dots. To propagate or reverse the state of the network a soliton was created [43]. Once created, usually near the end of the QCA wire, the soliton can move back and forth along the chain depending on the magnetic oscillating field. Figure 2-3 depicts how the propagation of states could occur. Notice at T2 when the soliton (dark blue bar) reaches the input dot, it will stay between the input dot and the first circular nano-dot. Once the magnetic oscillating field begins to rise, the soliton will begin to move forward along the chain, as depicted at T3. Had the input dot been set to 0 (magnetic dipole moment pointing to the left) and the soliton moving backward,

13

as depicted at time T2, the soliton would be lost and another would need to be created. In the network described above, the circular dots were fabricated to a diameter of 110 nm, at a thickness of 10 nm, on a pitch of 135nm as shown in Figure 2-2. The size and shape ensured that the ferromagnetic circular dots made of a Supermalloy ($Ni_{80}Fe_{14}Mo_5X_1$, where X was other metals) had single domain magnetic moments. This is important, considering that the enumeration of states is based on the orientation of magnetic dipole moments and switching dynamics. It was found that the circular dots with a diameter of 100 nm and thickness of 10 nm exhibited ideal switching characteristic [53]. The minute amount of energy required to saturate the dots, starting at about 5 Oe, and the high residual magnetization, about 80%, are prime characteristics produced by these single domain nano-dots [53]. The magnetostatic energy (PE in the magnetic field) between two dots in this network was about 200 kbT, (where kb is the Boltzmann's constant and T is the temperature) and should be at least 40 kbT to keep thermal errors below one per year [53].

2.2.2 Field-Coupled Nano-Pillars

In a nano-pillar network, a basic cell consists of a shape engineered single domain magnet as shown in Figure 2-4 (A) [1, 13, 22-25, 29, 30, 44, 54-60]. Due to the shape anisotropy, the pillars develop easy and hard axis of magnetization. A magnetic dipole moment experiences lower demagnetization energy when aligned along the easy axis of magnetization, and hence, is in an energetically favorable state. Conversely, when aligned along the hard axis, the magnetic dipole moment is unstable and will eventually align itself along the easy axis to reduce the demagnetization energy. This allows for the enumeration of states along the easy axis of magnetization and creates a digital mode of operation for Magnetic Cellular Automata.

14
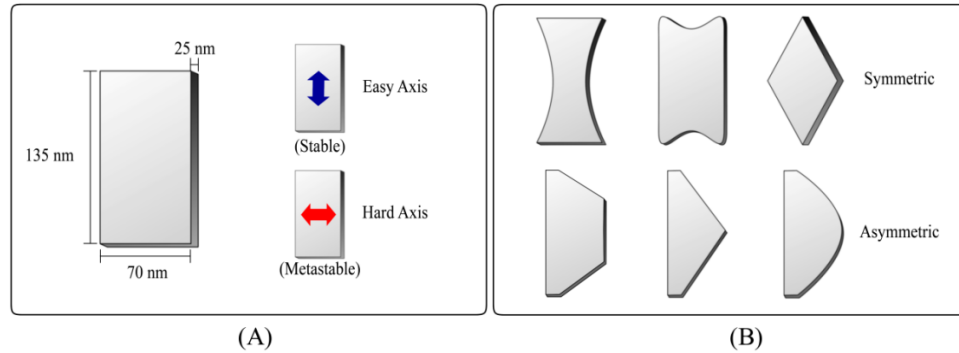
Figure 2-4 (A) shows the fabrication dimensions of a permalloy nano-pillar. Due to the shape anisotropy, an easy and hard axis of magnetization were created. (B) are various shapes that were studied under different demagnetization fields to determine coupling order lengths.

A MCA wire is constructed by placing nano-pillars side by side, as shown in Figure 2-5 (A). Proper data propagation occurs when all the magnetic dipole moments of each cell in the MCA wire are in an anti-parallel arrangement. Assume the wire's initial state in Figure 2-5 (A) was with each cell's magnetic dipole moments pointing along the hard axis of the magnets. Csaba *et al.* suggested an "adiabatic pumping" scheme [55] where the energy barrier required for switching is reduced by first applying a magnetic field along the hard axis. This causes the nano-pillar's magnetic dipole moment to align itself along the hard axis which is the initial state before an input is given. This state is energetically unfavorable, making it possible to supply a weaker external magnetic input field to the system. Once an input is given, magnetostatic coupling energies between the magnets causes data to propagate down the wire. Several shapes, shown in Figure 2-4 (B), were also studied under an adiabatic and rotating demagnetization fields to investigate the anti-ferromagnetic coupling order [23]. It was determined that symmetric shapes demonstrate longer data propagation lengths with an adiabatic demagnetization field, while the asymmetric shapes performed better under the rotating demagnetization field.

15
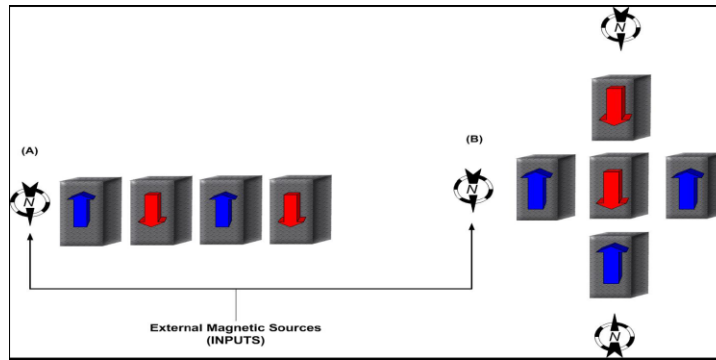
Figure 2-5 (A) depicts a magnetic QCA wire. An external input is given to the wire which had sufficient strength to coerce the rest of the wire to change its state accordingly. (B) is a Magnetic QCA Majority Gate. The gate has three inputs (external energies); the output will depend on the dipole moments of the inputs. In this example, the topmost and leftmost inputs have the positive end of the dipole moment pointing downward and the bottom input has its moment pointing upward. The majority of the inputs are pointing downward so the center pillar is the result of the majority.

Figure 2-5 (B) is a MCA majority gate, which was the first logic gate fabricated in this type of CA [1]. The shape of the rectangular nano pillar was chosen because of the bi-stable nature. The shape anisotropy of the nano-pillars introduced a high energy barrier between the two stable states, thereby making them less error prone. The higher energy barrier also led to more power dissipation but was mitigated by an adiabatic switching/pumping mentioned previously. The nano-pillars dimensions were 35nm thick, had a width of 70nm, height of 135nm, and were made of permalloy. The nano-pillars were fabricated via an electron beam lithography process. The MCA majority gate was shown to have performed all possible logic combinations of a three input gate and operated at room temperature. This was significant since a majority gate can implement the essential logic gate functions necessary to implement any Boolean function.

Research studies have also been conducted to investigate the low power operation and defect characterization of MCA devices. MCA devices will need a clock implementation for synchronous operation and many have proposed using an external magnetic field as a clocking mechanism [44, 61, 62]. The clock energy along with the

16

energy necessary to provide an input is the total energy of an MCA system. The energy loss was calculated for a 32-bit MCA ripple carry adder and was found to be 0.004 - 0.285 pJ at a switching frequency of 10^8, which is in the worst-case scenario on par with larger low power CMOS devices [61]. MCA devices have also been found to be robust to common fabrication defects and have shown long range ordering [23, 63].

This particular implementation of Magnetic Cellular Automata, which uses rectangular nano-magnets as the basic cell, was of primary interest in this dissertation due to their bi-stable nature and room temperature operation [44]. The formation and reliability of a single domain magnetic moment of a ferromagnetic nano-structure, and the magnetic coupling between neighbors are discussed in detail Chapter 4. Chapter 5 explores how ferromagnetic and anti-ferromagnetic wire architectures perform under different clocking fields. A novel ferromagnetic cross wire system, investigated in Chapter 6, is also presented which utilizes rectangular ferromagnetic nanostructure as a basic cell for MCA. The research presented within this dissertation, coupled with the pioneering work previously reported, continues to move MCA to the forefront of magnetic logic devices.

2.2.3 Biaxial Magnetocrystalline Anisotropy

MCA will most likely need a clocking structure to align magnetic cells into a hard axis of magnetization. Alignment into the hard axis allows for previous states to be erased and lowers the work needed to overcome the energy barrier to 'flip' a nano-magnet. Once a nano-magnet is aligned in a hard axis of magnetization, for example via an external magnetic field, the external energy is removed to allow the magnetic cells to settle into a lower energy state along the easy axis of magnetization. During this relaxation time the nano-magnets are very easily influenced by the external forces of a

17
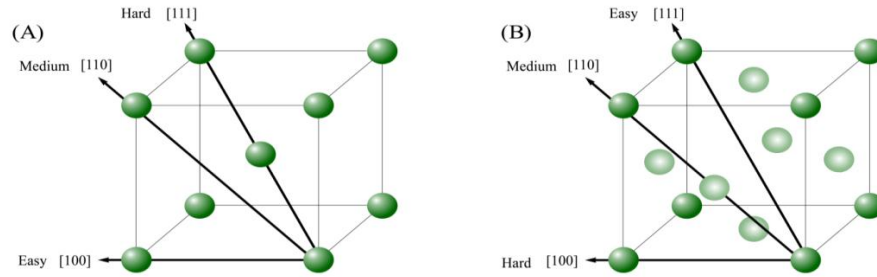
Figure 2-6 (A) is a BCC crystal of iron which exhibits magnetic anisotropy along different crystal planes. Image (B) is a FCC crystal of cobalt. Note for cobalt the [111] crystal direction is the easy axis of magnetization.

neighboring cell, which is the very essence of cellular automata. If an input is given to one nano-magnet it will drive its neighbor which in turn drives its neighbor and so on.

Recently, Carlton *et al.* has suggested introducing a magnetocrystalline biaxial anisotropy energy into magnetic simulations to increase the relaxation time of a nano-magnet [64]. Many ferromagnetic materials exhibit magnetic anisotropy such that magnetic properties differ along crystal planes, as shown in Figure 2-6. If a magnetic cell is engineered such that the clock is provide along the hard axis, the magnetocrystalline anisotropy will provide energy to increase the relaxation time. The benefit of the biaxial anisotropy energy is it will allow time for an input to flow throughout a system. For example, if the propagation time for a magnetic cell is 100 picoseconds , as estimated by Carlton et al. [64], the relaxation time for a clock domain of a wire will have to be less than that propagation time to insure signal integrity. The extra energy provided by the biaxial anisotropy will increase the relaxation time, and therefore allow for proper data propagation within clocking boundaries and mitigate magnetic frustrations.

(A)   (B)   (C)   (D)
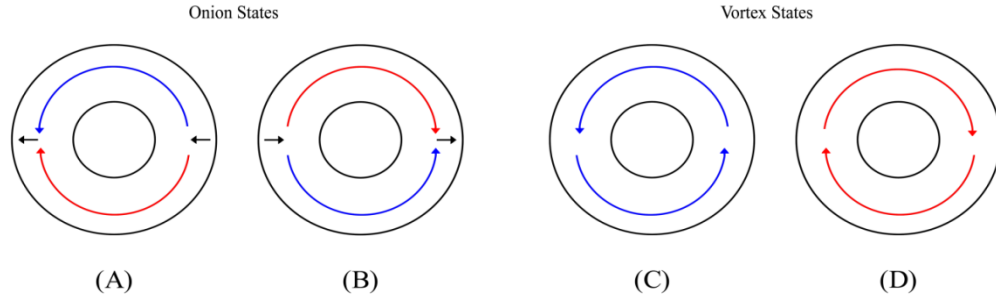
Figure 2-7 (A) and (B) show the two stable configurations of the onion state in a magnetic nano-ring. The arrows represent the magnetic moment of the nano-rings. The onion states are similar to single domain magnets due to the production of stray fields. Image (C) and (D) are the stable vortex configurations of the nano-rings. This configuration has zero stray fields.

2.3   Magnetic Nano-Rings

Magnetic nano-rings present an interesting architecture, particularly for storage elements [54, 65-69]. Magnetic Random Access Memory (MRAM) has many of the same benefits as magnetic logic, such as non-volatility, extreme longevity, radiation hardness, etc., but one of the current dilemmas in the technology is the neighbor-neighbor magnetostatic interaction. Magnetic nano-rings have shown a propensity to reduce this interaction as well as controllability via external magnetic fields and more recently through spin torque transfer [68, 70, 71].

Magnetic nano-rings consist of circular soft magnetic disk with the center removed as shown in Figure 2-7. An intriguing feature of the magnetic nano-rings design is the possible onion or vortex states. Figure 2-7 (A) and (B) show the magnetic onion states. What is striking about these configurations is the fact that similar magnetic poles are in close proximity and the presences of magnetic flux where the poles coincide. The other two stable configurations are given in Figure 2-7 (C) and (D). These closed-flux states are in a vortex configuration. The benefit of a vortex state for memory is the zero

19
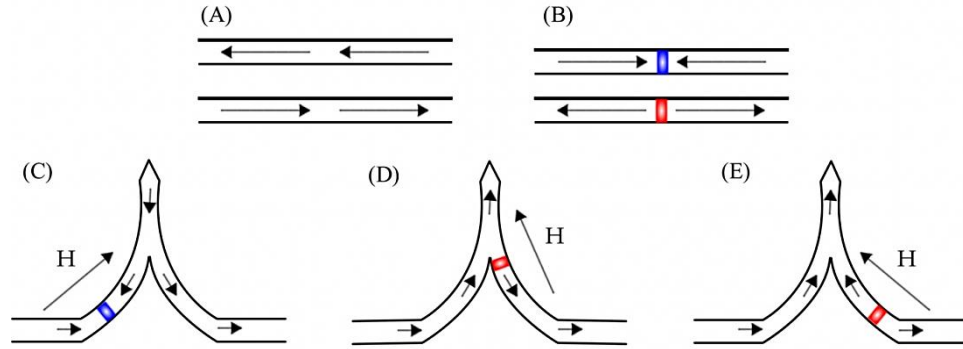
Figure 2-8 (A) shows two different nano-wires with a contiguous magnetic domain in opposite directions. (B) depicts two different types of domain wall configurations, one with a head to head configuration and the other with a tail to tail. Whenever there is a domain wall present the magnetization opposing the motion of the domain wall is considered a logical '0'. Figures (C), (D), and (E) are progressions of the operation of a NOT gate. For this abstraction an external magnetic field (H) was applied to move the domain wall into and through the kink which performs an inversion of the logical state.

stray field of the closed-flux configurations. This reduces any significant magnetostatic interaction with neighboring bits allowing for higher bit densities.

Magnetic nano-rings can also act similar to single domain nano-disks. The flux created by an onion state is similar to the stray fields created by single domain magnets. By placing nano-rings in close proximity, they can interact through their magnetostatic fields. Experiments have also demonstrated a structure where the nano-rings are linked together and magnetic information is coupled between rings [72].

2.4 Magnetic Domain Wall Logic

Another type of nano-magnetic system is driven by the motion of a domain wall. A domain wall is the boundary where a magnetic dipole moment gradually transitions from one direction to the opposite direction, such as a Bloch wall. By constructing a magnetic nanowire magnetic dipole moments are formed parallel to the length of the wire due to magnetic shape anisotropy, as shown in Figure 2-8 (A). In a sufficiently long nanowire, multiple domains form along the length of the wire, and in between these magnetic

20

domains are domain walls, as shown in Figure 2-8 (B). Researchers have demonstrated the manipulation of domain walls through the use of external magnetic fields and spin torque moment transfer [73-77].

A pioneering experiment in domain wall logic was the demonstration of a NOT gate [78]. By introducing a kink in the nanowire, as shown in Figure 2-8 (C), the inverse of the logical state can be attained. The manipulation of the domain wall was done through a rotating external magnetic field (H) which moved the domain wall through the kink, as shown in Figure 2-8 (C)-(E). To enumerate the logic the flow of the domain wall must be taken into account. In the example given in Figure 2-8 (C) the domain wall was moving from left to right. To the left of the domain wall was considered a logical '1' while the opposite magnetization on the right side of the domain wall was a logical '0'. The domain wall was then propagated up and through the corner, and then down the wire via an external rotating field (H). As can be seen in Figure 2-8 (D), once the domain wall passed through the corner, the state of the wire was inverted and could be shifted along the rest of the wire. Using this structure, a magnetic shift register was also demonstrated [73, 78]. Shift registers are used in many logical components and are an essential component of a central processing unit. The magnetic shift register was successfully operated at 27 MHz and inverted the same domain wall approximately 100,000 times. This demonstrated the stability of the domain wall.

Subsequently a logical AND gate was experimentally proven and is shown in Figure 2-9 (A) [75]. The AND gate consisted of two input wires which taper down to a junction point. This junction point was connected to a thicker output wire where the domain wall was propagated along via an external magnetic field. The junction point acts as a valve,

21
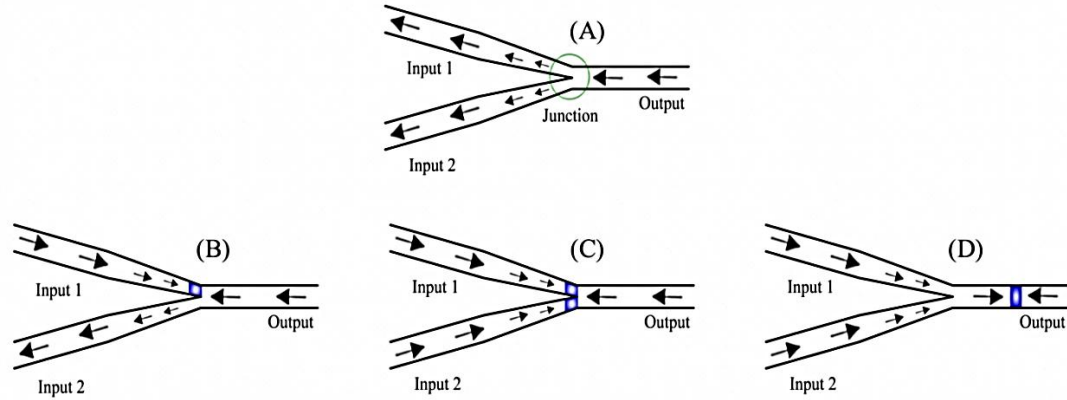
Figure 2-9 (A) shows the basic domain wall logic structure of an AND gate. It is made of two tapered input wires which meet at a junction point. Assuming that (A) was the initial state (B) shows where a logical '1' was injected into Input 1. (C) depicts a logical '1' being injected into both Input 1 and Input 2. Due to the energy barrier at the junction point, (D) can only be reached from (C).

providing an energy barrier. Using the same logical nomenclature as the NOT gate, a magnetic moment that opposes the flow of the domain wall was considered a logical '0'. Figure 2-9 (B) depicts a logical '1' injected into Input 1 (domain wall motion from left to right). Once the domain wall reached the junction, the external magnetic field could not overcome the energy barrier. Therefore the output remained a '0'. Figure 2-9 (C) has both Input 1 and Input 2 set to a logical '1'. With the injection of a domain wall into both inputs, and the external magnetic field, there now was enough energy to overcome the barrier of the junction point and Figure 2-9 (D) proceeds. Domain walls were introduced in the referenced work through the use of injection pads. It is also possible to induce domain walls through the use of short current pulse or via magnetic fields from current carrying wires [73, 76]. With the demonstration of an AND and NOT gate, all the necessary requirements to produce any logic circuit had been achieved. More recently domain walls have shown the propensity to be controlled via spin torque momentum transfer [76, 77, 79, 80]. This could lead to more practical implementation of controllers and integration with other technologies such as CMOS and MRAM.

22

Chapter 3

Fabrication of Nano-Structures via Electron Beam Lithography

3.1   Introduction

Electron beam lithography (EBL) is a high resolution fabrication method often used to repair/create masks for photolithography and nano-imprint lithography. The shorter wavelength of an electron and the lack of diffraction limitations found in traditional photolithography light sources allows for features down to 4 nanometers to be realized using EBL [81]. Although the throughput of an EBL direct write process is much lower than photolithography, research continues to create a commercially viable EBL system. For the purpose of investigating ferromagnetic nano-structures, EBL provides the flexibility of easily prototyping several different structures with the high resolution necessary for the fabrication of nano-magnetic logic systems. In the following sections the EBL process used throughout this research is detailed.

3.2   Overview of Electron Beam Lithography Process

The bottom up EBL approach began by coating a silicon substrate with an electron sensitive positive resist, namely polymethylmethacrylate (PMMA). The resist was then exposed using a JEOL 840 thermionic Scanning Electron Microscope (SEM) retrofitted with a Nabity NPGS lithography system to create the desired mask patterns [82]. The exposed areas were removed via a chemical developer using a solvent of methyl isobutyl ketone (MIBK): isopropanol 1: 3. A soft ferromagnetic material was then deposited via a Varian Model 980-2462 Electron Beam Evaporator. A bond was formed between the

23

ferromagnetic material on the resist in the non-developed areas, as well as on the substrate where the developed resist had been removed. The final liftoff step involved using a solvent (acetone) which removed the resist from the substrate leaving behind only the ferromagnetic metal on the exposed substrate areas.

Several variations of the EBL process outline above were used in the fabrication of the nano-magnetic structures, such as molecular weights of electron sensitive resists, development times, and metal thickness. Specific details pertaining to each phase of the research can be found in the respective chapters. In the proceeding sections background information on the theory for each step of the process and the rationale for specific methods used are discussed.

3.3   Electron Beam Resists

Electron sensitive resists may be classified into two categories, positive and negative. When exposed to an electron beam, a chemical reaction is induced in a negative electron beam resist which causes crosslinking between polymer chains. The crosslinked polymer chains become insoluble, while the unexposed polymer chains are soluble creating selectivity. A positive electron beam resist also has chemical reactions induced by the electron beam energy which degrades the polymer molecules into smaller chain scission molecules. The chain scission molecules are more soluble than the unexposed polymer and can be developed using an organic solvent.

For the purpose of fabricating nano-structures with thickness ranges and lateral dimensions in the nano-regime, polymethylmethacrylate (PMMA) is the positive resist standard for high resolution lithography. Although the low sensitivity of PMMA reduces the commercial usability of the resist, the high contrast and low swelling during development are significant factors contributing to the high lateral resolution. The

24

PMMA Main Chain   PMMA Main Chain Scission
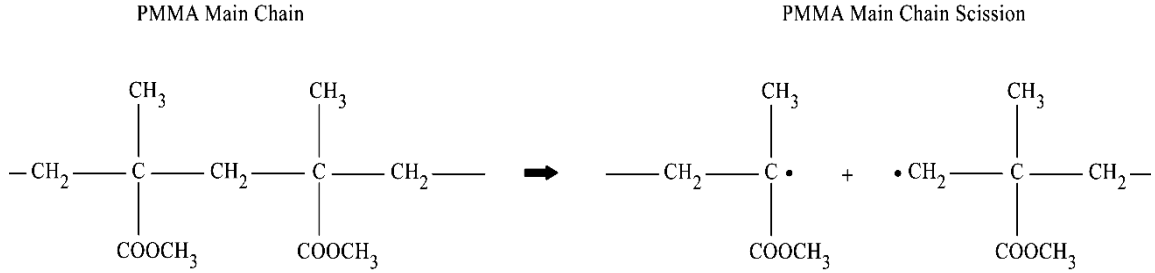
Figure 3-1 shows a chemical reaction induced by the exposure of the positive resist polymethylmethacrylate (PMMA). The main molecular chain is given on the left and the scission of the main chain is shown on the right. The lower molecular weight of the chain on the right makes the resist more soluble in a developing solvent.

dissolution rate of PMMA can be understood via the exposure resist model given in equation 3-1, where R is the dissolution rate for the exposed resist, R_O is the dissolution rate for the unexposed resist, M_0 is the initial molecular weight, M_n is the molecular weight post exposure, a is the developers kinetic solubility dissolution parameter, and G_s is the scission efficiency [83].

$$R / R_0 = k(M_0 / M_n)^{-a} = (1 + kQG_sM_0)^a \qquad (3\text{-}1)$$

From the model, it is given that the dissolution rate is inversely proportional to the molecular weight. As the electron beam induces chain scissions in the positive resist, the molecular weight of PMMA is reduced and therefore more soluble than the unexposed higher molecular weight PMMA. Figure 3-1 shows a main chain scission for polymethylmethacrylate which lowers the molecular weight of the resist creating the desired selectivity between exposed and unexposed areas.

3.4 Preparation and Application of PMMA Resist

In order to fabricate a device, a substrate is needed. N-type 250mm thick silicon wafers were used throughout the fabrication process as the substrate due primarily to

25

Table 3-1 outlines and describes the process steps used for the RCA cleaning procedure.

Process	Description
Rinse wafers with DI water for two rinsing cycles	Rinses any superficial debris
Dip in HF (50:1) for 20 seconds	Removes native oxide
Rinse with DI water for two rinsing cycles	Rinses off any residue
Dip in SC1 for 10 minutes @ 60ºC	2000ml of DI water; 330ml of Hydrogen Peroxide; 330ml of Ammonium Hydroxide (6:1:1)
	Removes insoluble organic contaminants
Rinse with DI water for two rinsing cycles	Rinses off residue
Dip in HF (50:1) for 20 seconds	Removes chemical/native oxide
Rinse with DI water	Rinses off residue
Dip in SC2 for 10 minutes @ 60ºC	2000ml of water; 330ml of Hydrogen Peroxide; 330ml of Hydrochloric acid (6:1:1)
	Removes ionic and heavy metal contaminants
Rinse with DI water for two rinsing cycles	Rinses off residue
Dip in HF (50:1) for 20 seconds	Removes chemical/native oxide
Rinse with DI water for two rinsing cycles	Rinses off residue
Dry with Nitrogen Gas	Removes possible water spots

the atomically smooth surface and lack of magnetic response. The surface was prepared

for resist coating using the RCA cleaning procedure outlined in Table 3-1. The purpose

of the RCA cleaning procedure was to remove organic, ionic, and heavy metal

contaminants in order to prepare the Si wafer surface for the application of the electron

sensitive resist. A spray on solvent clean of acetone, followed by isopropanol, and dried

Table 3-2 outlines the resist spinner recipe used for 495K and 950K PMMA ranging from 30-120 nm of thickness.

Process Step	Description
1	Dispensed a 25mm diameter drop of PMMA resist
2	Pre-ramp up: 0-500 rpm 5 seconds
3	Ramp up: 500-5000 rpm 45 seconds
4	Ramp down: 5000-0 rpm 5 seconds
5	Prebake: 170°C for 30 minutes

using nitrogen gas was also done prior to the resist application to remove any possible contaminates from handling. The substrates were spun dried at 5000 rpm for 2 minutes to promote the evaporation of any residual solvents without altering the temperature of the substrate.

The application of the PMMA onto the wafer was accomplished using a Laurell Technologies WS-400A-8NPP/Lite Spin Processor. Due to the nature of the research, most of the fabricated devices were less than 40 nm thick and therefore thin layers of resist were necessary. A Teflon pipette was used to deposit a 25mm circle of PMMA at room temperature. The recipe used to apply a uniform coating of PMMA is given in Table 3-2. After the resist was spun, a prebake was done in a convection oven at 170°C for 30 minutes to remove any excess solvent. The spin recipe was successfully used for applying resist layers ranging from 30 nm to 120 nm with no adhesion issues.

The two molecular weights of PMMA used were 495,000 and 950,000 in anisole, which were commercially available from MicroChem [84]. The percentage of PMMA to anisole was diluted to less than 2% for the desired film thickness by adding anisole. For high resolution electron beam lithography, a single layer of 950k MW PMMA was able to
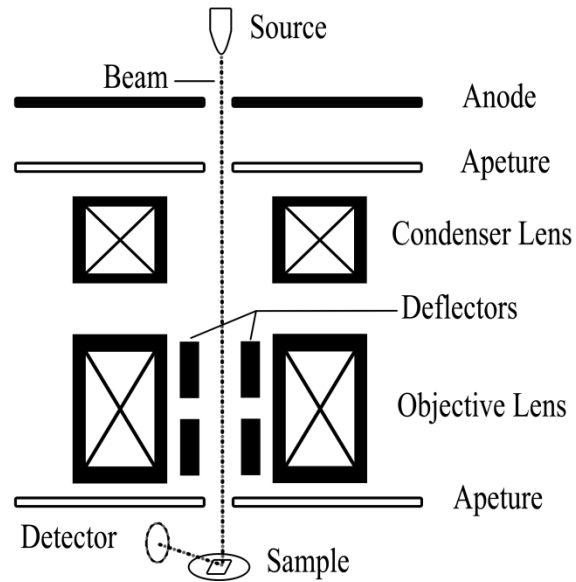
Figure 3-2 is an abstraction of a scanning electron microscope column. For electron beam lithography, thermionic emission filaments are often used due to the stable emission current.

successfully meet the critical dimensions of 20 nm between each nano-magnetic device. A bilayer resist process was also used where the lower molecular weight PMMA was spun as bottom layer, prebaked, followed by the same procedure for the higher molecular weight for the top layer. The higher molecular weight PMMA provided the better contrast while the more sensitive bottom layer created an undercutting profile ideal for a clean liftoff.

3.5 Scanning Electron Beam Exposure

Traditional exposure methods use light to develop photoresist down to just below a micron, but for high resolution lithography, electron beam exposure systems continue to offer researchers low cost rapid prototyping of submicron feature sizes. Figure 3-2 shows a typical Scanning Electron Microscope (SEM) column. The beam is focused via magnetic lenses and is scanned across the surface of a sample via deflectors. SEMs have several possible electron gun sources, such as thermal field emission cathodes, cold field
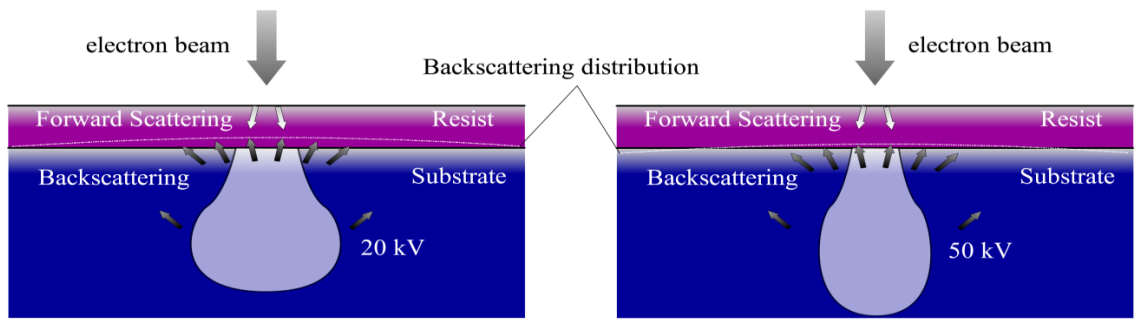
Figure 3-3 represents two different electron beam energies entering an electron sensitive resist and substrate. The figure on the left is at a lower acceleration voltage and the backscattered electrons expose the resist as well as the forward scattered electrons. The figure on the right is at a higher acceleration energy and the resist is exposed primarily by forward scattered electrons.

emission cathodes, and thermionic emission sources which are preferred electron beam lithography. Field emission sources are excellent for imaging via secondary electron excitation due to the high brightness of the source, but are prone to contamination from gases in the vacuum system which can cause a drift in the emission current [85]. The stability of a SEM's emission current is critical to the proper exposure of resists and is not an issue with thermionic sources. A tungsten thermionic emission source emits electrons by providing thermal energy to overcome the work function of the metal; breaking the electron free from the material into the vacuum. A uniform thermionic source's emission current density can be model by the Richardson-Dushman (equation 3-2) where J is emission current density, A_G is the Richardson constant (1.20 x 10^6 Am^{-2} K^{-2}), T is temperature, W is the metal's work function, and k is the Boltzmann constant ($8.617\,343 \times 10^{-5}$ eV K-1) [86].

$$J = A_G T e^{\frac{-W}{kT}}$$

(3-2)

The exposure mechanisms of electron sensitive resists depend on several factors, such as the atomic number of the substrate, beam energy, and resist thickness. Figure 3-3 depicts how electrons scatter as they traverse the resist and substrate mediums. As electrons move through the resist, energy is deposited into the medium through interactions between the primary beam and the resist molecules. When the incident beam of accelerated electrons (where acceleration voltages range from 20-50kV) enters the resist, interactions with a thin resist (<100nm) are small, and only minute amount of initial energy is deposited into the resist. The transparent resist allows most of the energy to enter the substrate which induces several types of reactions such as x-rays, auger electrons, and secondary electrons. As the incident electrons interact with the substrate, several scatter back into the resist known as backward scattered electrons. Higher energy beams penetration deeper into the substrate and have less resist exposure due to backscattered electrons, while lower energy beams have a broader lateral profile in the resist and can suffer from the proximity effect. Higher energy electron beams offer improved resist exposure profiles but require higher doses of energy to expose the resist. The energy deposited by energetic electrons into resist can be modeled using the Bethe energy model, where E is the electron energy, x is the distance of the electron trajectory, n_e is the electron density of the atoms, e is the charge, and I is the mean excitation energy [87].

$$\frac{dE}{dx} = \frac{-2\pi e^4 n_e}{E} \ln((\frac{E}{I})(\frac{e}{2})^{1/2}) \qquad (3\text{-}3)$$

From this equation it can be understood that as electron beam energy is increased, the amount of energy imparted to the resist per unit length decreases. As higher acceleration energies are used, higher doses are needed to expose the resist.

30
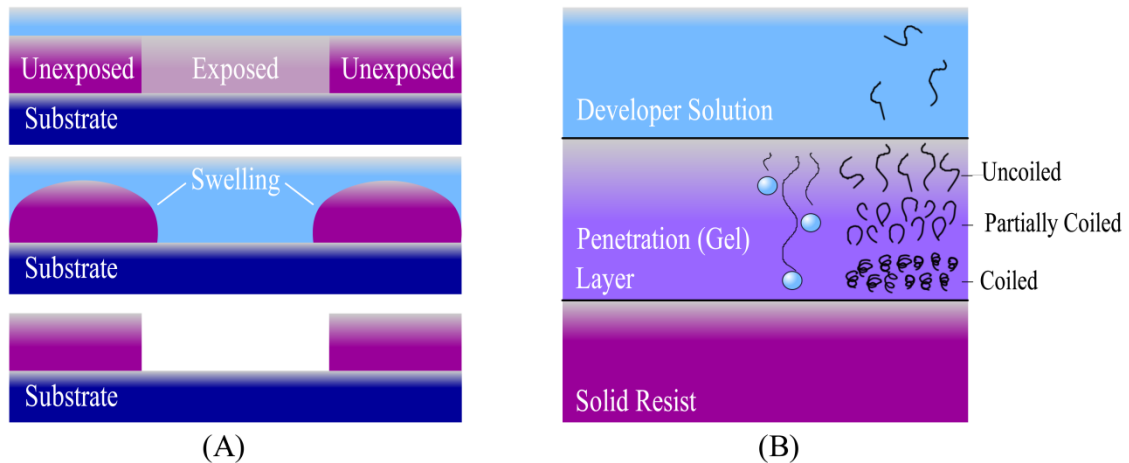
Figure 3-4 (A) depicts the sequential development process (top to bottom) for a positive resist such as PMMA. Figure (B) shows the interaction between the developer solution and resist. As the developer penetrates the resist, a gel layer is formed. The activation energy necessary for the PMMA to uncoil is provided by the penetrating developer molecules.

3.6   Resist Development

In order to selectively remove resist, a developer solution normally removes a resist of lower molecular weight more effectively than the same resist of a higher molecular weight. The developer solution is specific to the particular chemistry of a given resist and the necessary activation energy needed to dissolve it. Figure 3-4 (A) depicts the developing process of a sample that has both exposed and unexposed areas of a positive resist placed into a developer solution. The developer penetrates the lower molecular weight resist removing it from the substrate, while the higher molecular resist areas swell as a resistance mechanism to dissolution. Swelling is normally an undesired condition of developing and can cause negative effects such as bridging [87]. Once the developer is removed and the resist is dried a mask is created. In order for the dissolution of the lower molecular weight resist to occur, a solvent must provide the necessary activation energy to uncoil the resist molecules. The solubility parameter and resist contrast for various developers of PMMA have been studied and are used to

31

Table 3-3 outlines the development process used for a single layer of 950K PMMA and for s bilayer 495K-950K PMMA (bottom-top) resist.

Process Step	Description
Development	MIBK:Isopropanol 1:3 for 60 seconds constant stirring
Rinse	Isopropanol 20 seconds constant stirring
Dry	Nitrogen gas

calculate the dissolution rate in equation 3-1[83]. A poor developer with low activation energy will provide insufficient energy to efficiently break intermolecular and intramolecular forces of the resist. This increases the dissolution time which in turn increases swelling, deforming the desired mask pattern. The combination of a high molecular weight PMMA resist, and a developer solution of MIBK:Isopropanol 1:3 was used in this research to attain the high resolution lithography necessary for the creation of magnetic logic devices.

The same development recipe was used for a single layer of 950K PMMA and the bilayer 495K-950K (bottom-top layer) of PMMA and is given in Table 3-3. Since the top 950K PMMA layer of the bilayer resist provides the desired mask dimension it dictates the development time and is the same when using only single layer of 950K PMMA. The lower molecular weight bottom layer of 450K PMMA dissolves at a fast rate, which created the desired undercutting profile and ensured proper liftoff.

3.7   Film Deposition

For the fabrication of nano-magnetic logic devices, a soft ferromagnetic metallic material demonstrates ideal characteristics for logical switching [14, 49]. There are several methods available for the deposition of thin ferromagnetic films such as electroplating and sputtering. Both aforementioned techniques are ideal for specific

32
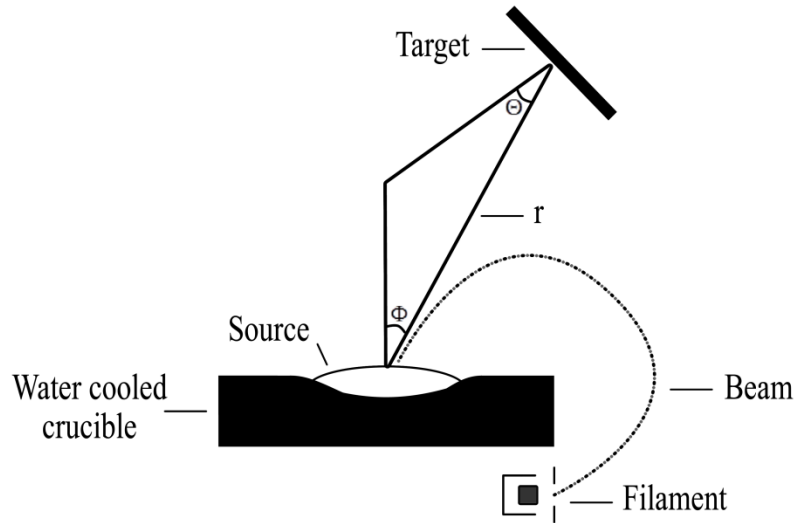
Figure 3-5 is a schematic of an electron beam evaporator. The electron beam from the filament provides thermal energy to the solid source which causes the matter to transition into a gas phase. The evaporated source proceeds to grow a thin film of the material as it interacts with the surface of the target.

fabrication situations, particularly when the conformal coating of a surface is desired. In this research electron beam evaporation was used for thin film deposition; primarily due to line of sight deposition which aids in the liftoff process and the preservation of the ferromagnetic alloy stoichiometry [88].

An electron beam evaporation uses an electron filament (as known as an electron gun) to vaporize a solid material source shown schematically in Figure 3-5. As the source material is heated via the thermal energy provided by the electron beam, it under goes a matter phase transitions from a solid to a gas. The phase transitions of a source are dependent on the physical material properties and can be characterized by the vapor pressure. If the vapor pressure for a material is above 10^{-2} Torr it will typically go through a standard matter transition (solid to liquid to gas), and are readily evaporated. Other elements such as Chromium (Cr) have vapor pressure below 10^{-2} Torr and transition directly from a solid to a gas in a process known as sublimation. These materials are harder to evaporate and have lower evaporation rates. Most of the devices

reported in this research were made of commercially available permalloy and nickel pellets. Both materials were readily evaporated in a vacuum of 10⁻⁶ Torr using a Varian Model 980-2462 Electron Beam Evaporator at rates of 1-8 Å sec⁻¹.

Once the source material is evaporated into a gas using a vacuum deposition system such as an electron beam evaporator, the gas can be modeled using the ideal gas law. An important parameter to consider during deposition is the pressure at which the material is evaporated. The vacuum pressure at the time of the evaporation determines the mean free path of a gas molecule and is given in equation 3-4, where p is the pressure of the vacuum system, and d is the diameter of the gas molecule.

$$\lambda = \frac{kT}{\sqrt{2}\pi p d^2}$$ (3-4)

Assuming the source material travels in a straight line from the evaporation source to the intended target, the mean free path of a material dictates how far a molecule can travel before it interacts with another molecule in its environment. For example, a molecule with a diameter of 4 Å at a vacuum pressure of 10⁻⁷ Torr has a mean free path of 60 meters [89]. It was determined that for the physical setup of the Varian evaporator used in this research, a vacuum pressure of 10⁻⁶ Torr would ensure minimal contamination during deposition. The position of the target in relation to the evaporation source was also considered and the growth rate can be predicted using equation 3-5, where p is the density, m is the mass evaporation rate, Φ is the angle normal to the source plane, and Θ is the angle normal to the target plane, as shown in Figure 3-5.

$$G = \frac{m}{\pi p r^2}\cos\Phi\cos\Theta$$ (3-5)

34
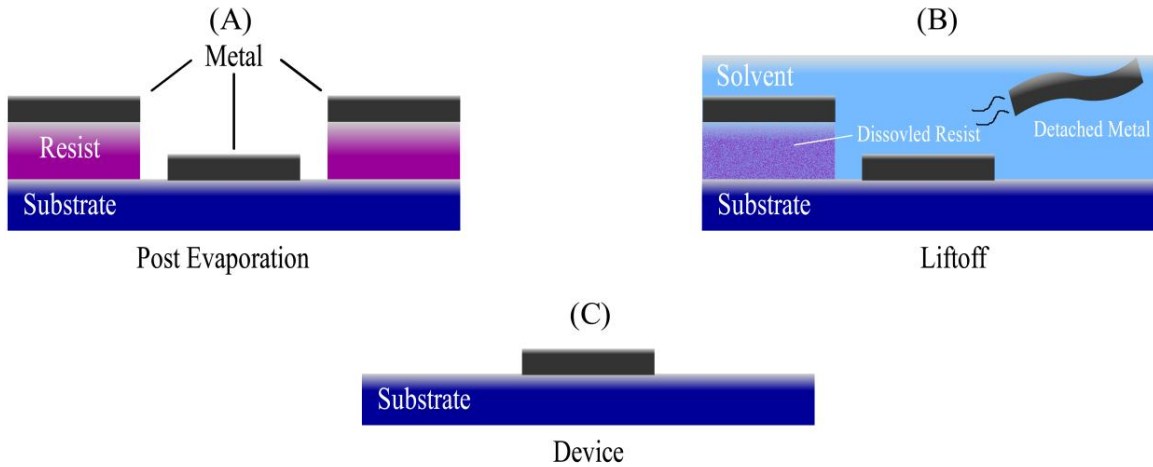
Figure 3-6 is cross-sectional view of the liftoff process. After the ferromagnetic metal layer has been evaporated, the sample is placed in a solvent which dissolves the resist and removes the unwanted metal layers. The final metal device layer is left in place bonded to the substrate's surface.

3.8 Liftoff

The final step in the additive electron beam lithography process involved selectively dissolving the remaining resist mask. Similar dissolution kinetics for the chemical development of a resist applies to the liftoff process. Instead of having dissimilar dissolution rates for a resist of different molecular weights as with the development step, in the liftoff process a solvent has to select between an organic resist material and, in this case, an inorganic ferromagnetic metal. The process used for the dissolution of the PMMA resist consisted of an ultrasonic agitation of the sample in a warm bath of acetone. The sample was agitated for approximately 10 minutes followed by an isopropanol rinse and dried using nitrogen gas. Once the resist was dissolved, the only remaining metal was the metal which formed a bond directly with the substrate and a cross-sectional diagram of the liftoff process is given in Figure 3-6.

Chapter 4

Introduction to Single Domain Nano-Magnets for Cellular Automata

4.1   Introduction

The interactions of orderly fabricated nano-magnets and the viability of nano-magnetic structures as logical building blocks is an area of great interest [12]. With few examples of orderly coupled nano-magnetic logic systems published, in this chapter the study of coupling between single domain dipole moments is discussed. A transitory introduction to magnetism is given leading into a discussion on the formation of single domain dipole moments. The coupling dependences of physical parameters such as size, surface roughness, and shape irregularities are also discussed. In particular, nano-magnets with an aspect ratio near 2:1 were of interest due to their bi-stable nature and functionality [1, 44]. The bi-stability created by the shape anisotropy (i.e. the 2:1 aspect ratio of the cell) significantly reduces meta-stable states, which in turn allows proper coupling between neighboring nano-magnetic cells. The objective of this chapter was to alter physical parameters of the cells and examine the resultant magnetostatic coupling interaction of single domain rectangular nano-magnetic.

4.2   Magnetism and Magnetic Materials Overture

The phenomenon known as magnetism arises from the angular momentum of a charged particle, generally the electron. Magnetism from an atom can originate from the orbital angular moment of an electron (L), the intrinsic angular momentum (S), or a combination of the two. The energies of both quantities are defined in quantum

36

mechanics by the quantum numbers l and s. The other two quantum numbers associated with magnetism, m_l and m_s; correspond to the angular momentum component along an external magnetic field (B). Following Pauli's exclusion principle and Hund's rule, it is possible for an atom to exhibit a net magnetic resultant force, known as a magnetic dipole moment. Based on the electron configurations of elements, materials can be classified into five magnetic categories: diamagnetic, paramagnetic, anti-ferromagnetic, ferrimagnetic, and ferromagnetic.

Diamagnetism is defined by materials that have a generally weak, negative magnetic susceptibility ($X_m = -10^{-6}$). Magnetic susceptibility is defined in equation (4-1), where

$$M = X_m H \qquad (4\text{-}1)$$

M is the material's magnetization vector, X_m is the magnetic susceptibility, and H is an external magnetizing field. From this relationship it is clear if the magnetic susceptibility is negative, the magnetization of the material M will be in the opposite direction of the applied magnetizing field H. Materials made of elements with closed shells and subshells, as well as many organic materials, are diamagnetic.

Paramagnetic materials have a small positive magnetic susceptibilities ($10^{-5} \sim 10^{-4}$) which are comprised of atoms with unpaired electrons. These unpaired electrons have a net resultant magnetic moment but are weakly coupled to neighboring atoms. Each atomic magnetic moment can be considered independent such that in the absence of a magnetic field the magnetic moments are aligned in random directions and the material has no net magnetization. Once an external magnetic field is applied, the magnetic moments experience a torque which causes them to align in the direction of the field causing a net magnetization. When the external field is removed, the alignment of the

37
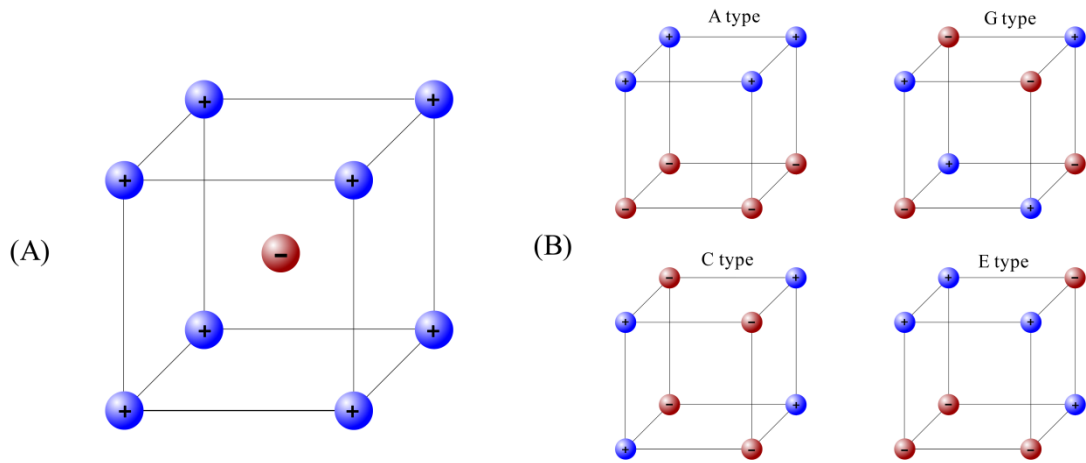
Figure 4-1 (A) depicts the anti-ferromagnetic ordering of a Chromium BCC crystal. The (+) and (-) signs represent the two possible spin states. The center atom contributes one atomic magnetic moment and the corner atoms combine to contribute a total of one opposing atomic magnetic moment to the unit cell. The magnetic moment for the unit cell is zero, which is the definition of an anti-ferromagnetic material. (B) shows several different anti-ferromagnetic atomic magnetic orderings for a simple cubic lattice.

moments are randomized again and the net magnetization is lost. Anti-ferromagnetic, ferrimagnetic, and ferromagnetic material also exhibit paramagnetic behavior above a critical temperature, were the atomic magnetic ordering energy is dominated by thermal energy.

Anti-ferromagnetic materials also have small positive magnetic susceptibilities similar to paramagnetic materials, but demonstrate atomic magnetic ordering as shown in Figure 4-1 (A). Below the Neel temperature T_N, a Body Centered Crystal (BCC) unit cell of Chromium ($T_N \sim 37.5°C$), exhibits anti-ferromagnetic ordering such that the total net magnetic moment of the crystal is zero. Above the Neel temperature, anti-ferromagnetic materials become paramagnetic. Different types of anti-ferromagnetic ordering exist for compounds such as cubic perovskites, which are shown in Figure 4-1 (B). For perovskites, the G-type ordering is due to an indirect superexchange interaction of the oxygen atoms which force the magnetic moments of neighboring atoms into an anti-ferromagnetic arrangement.
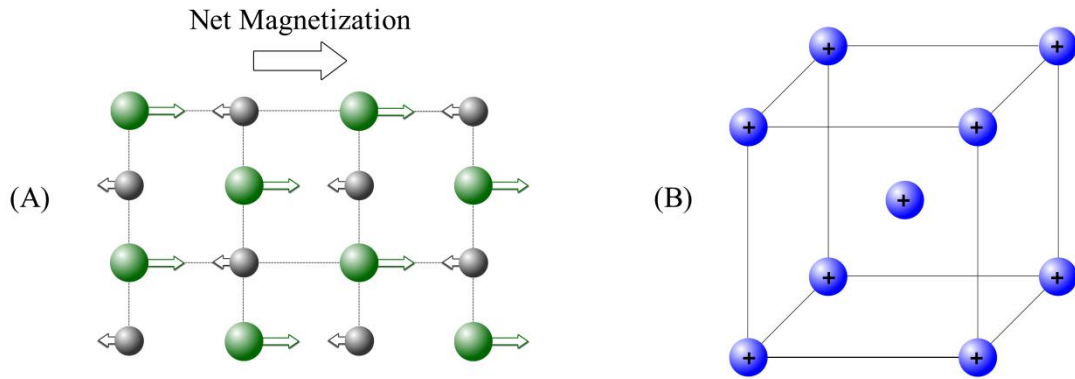
Figure 4-2 (A) is a two dimensional slice of a ferrimagnetic crystal lattice. The larger magnetization of the green atoms creates a total net magnetization along that particular direction. (B) is a BCC unit cell of an iron crystal. A ferromagnetic material is defined by each atomic magnetic moment having the same spin. The (+) signs indicates all the atoms are of the same spin.

Ferrimagnetism is very similar in nature to anti-ferromagnetism with regards to magnetic atomic ordering, but the magnetic sublattices are not equivalent as shown in Figure 4-2 (A). This causes a net magnetization difference between sublattices and, unlike anti-ferromagnetism where there is no net magnetization, a ferrimagnetic material exhibits a net magnetization ($M > 0$) below the Curie temperature (T_c). Ferrimagnetic materials have very large, positive magnetic susceptibility and become paramagnetic above the Curie temperature. Ferrimagnetic materials are often electrical insulators and do not suffer from eddy currents caused by rapidly changing magnetic fields. This makes ferrimagnetism very useful for automated applications and is used in many electronic devices.

If all the atomic magnetic dipole moments of a material are aligned in the same direction, as shown in Figure 4-2 (B), this material is defined as ferromagnetic. Ferromagnetic materials have very large positive values of magnetic susceptibility and vary based on the strength of the magnetizing field. The origin of ferromagnetic and

39

anti-ferromagnetic ordering between nearest neighbor atoms is actually not so classically intuitive. If two bar magnets were placed near each other it understood that they would couple in an anti-ferromagnetic or ferromagnetic manner, but this direct dipole-dipole interaction is actually not the origin of magnetic atomic ordering between nearest neighbors. Indeed, within a ferromagnetic material a quantum mechanical exchange interaction (direct and/or indirect) is the basis for magnetic ordering. The exchange interaction is governed by the lowering of electrostatic columbic energies within Pauli's exclusion principle. The energy associated with the direct Heisenberg exchange interaction is given in equation (4-2), where S_1 and S_2 are two interacting

$$U_{exch} = -J(r)S_1 \cdot S_2 \qquad (4-2)$$

spins separated by distance $r = r_1 - r_2$, and $J(r)$ is the exchange integral with units of energy. When the exchange integral is positive the resulting coupling of the spins is ferromagnetic; conversely when the exchange constant is negative the spins are coupled in an anti-ferromagnetic fashion. The Heisenberg exchange interaction is the dominant effect for spins S_1 and S_2 that have electron clouds with considerable overlapping and are atomically separated on the order of nearest neighbor (NN) or next to nearest neighbor (next-NN). Ferromagnetic materials are used in various electronic applications and were the primarily materials used in this study.

4.3 Magnetic Domains

Although ferromagnetic transitional metals such as Ni, Fe, and Co are permanent magnets, they can also be found to exert no net magnetic force due to the formation of domains within a material. When a ferromagnetic material is sufficiently large, in general greater than the mesoscopic range, multiple magnetic domains are created inside of the

40
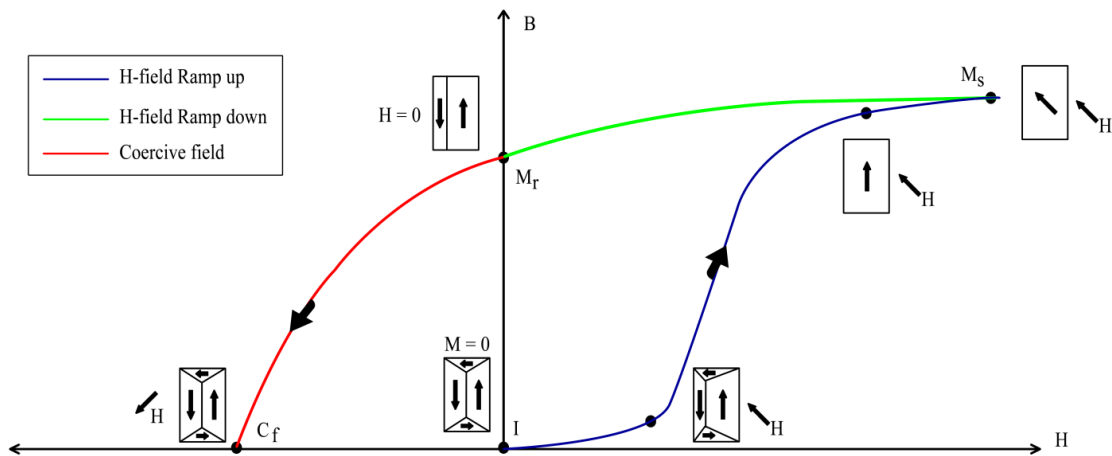
Figure 4-3 is half of a magnetic hysteresis curve. Point 'I' is the initial condition where the magnet has a net magnetization of 0. As an external magnetic field is applied (H) the appropriate magnet domains expand and contract as shown throughout the curve.

magnet, which arrange themselves to reduce the overall potential energy. These domains are commonly found in opposition to one another by 180 degrees and separated by a domain wall, as depicted in the initial state (I) of Figure 4-3 of the hysteresis curve.

Following the different points throughout the hysteresis curve provides a good example of magnetic domains and domain wall motion through the stimulus of an external field. It also presents the concepts of multiple domain structures and single domain magnetic dipole moments. At point (I) in Figure 4-3, a magnet was found with a total magnetization of zero due to the minimization of magnetostatic energy through the creation of multiple domains. As an external magnetizing field (H) was applied the total magnetization of the magnet increased. The magnetic domain with a larger component in the direction of the applied field expanded and is shown on the subsequent point on the curve. Eventually all the magnetic domains became aligned in the same direction as the applied field. The absence of domain walls is known as a single domain magnetic

41

dipole moment. As can be seen at the next point, the magnet was still not completely aligned in the direction of the applied magnetic field. This was due to an easy axis of magnetization, which in this case was due to the shape anisotropy of the magnet. Magnetic saturation (M_s) is defined as the point where the magnet has all possible magnetic moments aligned in the direction of the external field and is indicated by the image at the following point on the curve. Any external field applied greater than (M_s) will not change the magnitude or direction of magnetization. As (H) was ramped down until there was no external field present, the curve shows that the magnet still had a net magnetization. This is known as the remanent magnetization (M_r). Finally, another field was applied known as the coercive field. The energy necessary to demagnetize the remanent magnetization is defined as the coercivity. The final point on the curve demonstrates the formation of closure domains, which removed all magnetic flux. The formation of multiple domains is a complicated process and for the purpose of MCA is undesirable. The objective was to produce switches that couple with one another through magnetostatic field interactions and therefore the intent was to create magnetic cells that were single domain in nature.

Figure 4-4 is of a nickel anti-ferromagnetic MCA wire. In Figure 4-4 (A) each magnetic cell was approximately 400(l) x 200(w) x 30(th) nm^3. The image on the left was an atomic force microscopy (AFM) height image which represented the physical dimensions of the system, and on the right was the magnetic force microscopy (MFM) image illustrating the magnetic moments. The complicated magnetization found in the MFM image was due to the multiple domains formed within each magnetic cell in the wire. The formation of multiple domains is dependent on energy minimizations

42

(A)

(B)
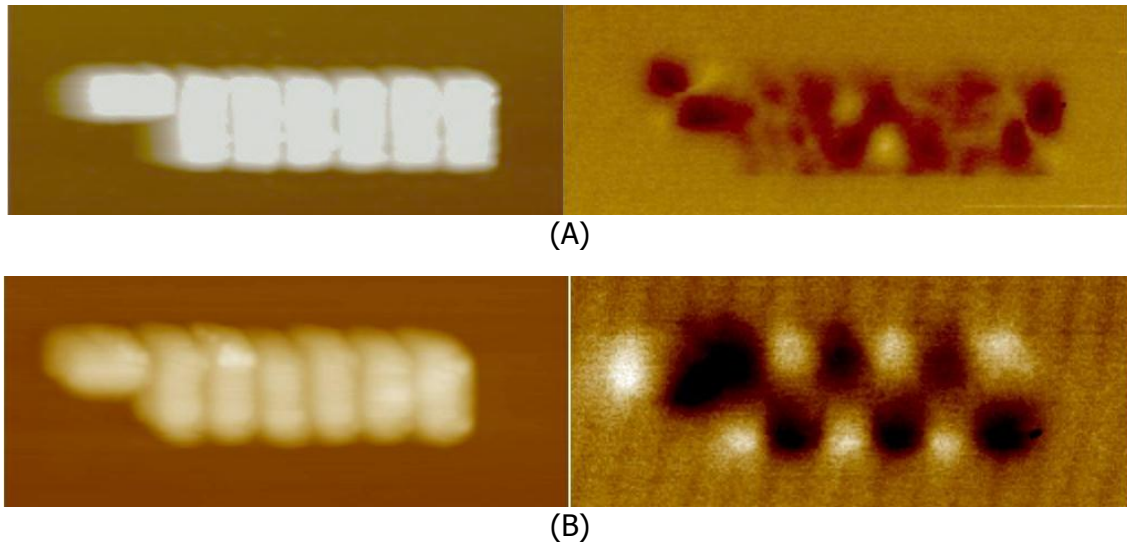
Figure 4-4 (A) is an AFM height amplitude plot (left) and a MFM phase plot (right). The dimensions of each Nickel rectangle in (A) were 200(w) x 400(l) x 30(th) nm^3. The complicated multiple domain structures arose from the physical dimensions and material properties of nickel. (B) is a nickel system with dimensions of 100(w) x 200(l) x 30(th) nm^3. The MFM image clearly shows a single domain magnetization as well as an anti-ferromagnetic coupling order.

factors such as crystalline anisotropy and shape anisotropy [90]. Figure 4-4 (B) is another chain with the same aspect ratio of 2:1, where each cell was approximately 200(l) x 100(w) x 30(th) nm^3. It was evident that the each magnet had a more regular single domain magnetic dipole moment. Furthermore, the magnetic dipole moments appear to be coupled to one another via magnetostatic fields. The reduction of size caused single domain moments of each cell to couple in a digital fashion between neighbors and is the essence of MCA systems. A single domain magnetic system affords the opportunity for a new logic and memory paradigm to be explored.

4.4 Fabrication Process

The electron beam lithography process began by coating a Si wafer with a resist, namely PMMA. This was accomplished by using a Laurell Technologies WS-400A-8NPP/Lite Spin Processor, which spun the wafer at high speeds causing the PMMA resist

43

to spread evenly over the entire wafer. A bilayer PMMA recipe was chosen using 495K molecular weight as the bottom layer and 950K molecular weight as the top layer. The 495K bottom layer was spun first and, then baked, followed by the 950K top layer being spun and baked. The purpose of the bilayer PMMA was to ensure a clean liftoff, which was aided by the undercutting profile created in the low molecular weight PMMA.

A pattern was designed using DesignCAD2000 NT. The most effective line spacing, exposure doses, points, and focus were determined by using diagnostic designs, such as the wheel pattern and spot burn process. A sample of the Si wafer coated with bi-layer PMMA was then loaded into the JEOL 840m retrofitted with the NPGS lithography system and a beam blanker. The SEM was then focused, and the stigmation was adjusted for optimal resolution. The pattern was selected and written via the NPGS system. Afterwards, the sample was unloaded and prepared for chemical development. It was placed in a bath of MIBK and Isopropanol (1:3) for approximately seventy seconds, followed by a twenty second Isopropanol bath, and finally nitrogen dried.

A ferromagnetic material was chosen for deposition, in this case nickel and permalloy (Ni80Fe20), and was evaporated via a Varian Model 980-2462 Electron Beam Evaporator. A vacuum of approximately 2 μTorr was achieved and the material was evaporated at a rate of 5 Å sec^{-1}. Once the desired thickness of the material was deposited, the next stage was the liftoff step. The sample coated with the ferromagnetic material was placed in a heated ultrasonic acetone bath for approximately 15 minutes, which selectively lifted off the unwanted PMMA and left the fabricated magnetic structure intact.

44

Figure 4-5 is four different sets of data of the same MCA interconnect. The top figure is a SEM image, followed by a 3D representation of an AFM plot. Next is an image of a 2D AFM plot and the bottom image is a MFM phase plot. From these images significantly irregularities in the cell structure and surfaces are visible. The fourth cell from the right has no in-plane moment detected due to the surface imperfection.

4.5 Magnetic Coupling of Single Domain Nano-Magnets

For magnetic logic systems to be considered a viable technology, reliable interaction between magnetic switches must be realized. Interactions between magnetic switches are accomplished through the coupling of spins which create magnetic dipole moments. There are different ways for spins to interact but here the interaction was based on magnetostatic field interactions. The field interaction between magnetic cells will intuitively be affected by the physical dimensions of each magnetic cell. Particularly, how factors such as surface roughness and shape irregularities affect coupling interaction is important since the surface area begins to dominate volume at the nano-scale.

Figure 4-5, Figure 4-6, and Figure 4-7, are a set of images of three different chains of nano-magnetic cells and have the following images from top to bottom: a SEM surface image, an AFM 3-D surface plot, an AFM 2-D surface image, and a MFM image. Each figure is of the same chain of nano-magnetic cells and each cell has the

45

Figure 4-6 is another four sets of data of a different MCA wire. The top figure is a SEM image followed by a 3D representation of an AFM plot. Next is an image of a 2D AFM plot and the bottom image is a MFM phase plot. In this chain, the cells with a smoother surface have better defined symmetrical dipole moments.

dimensionality of approximately 160nm height x 80nm width x 40nm thickness. The rational was to compare the magnetic moments of each cell and the resulting magnetic coupling of neighbors to: surface roughness, shape regularity, cell spacing, and cell size. These results showed that nickel had single domain characteristics parallel to the substrate (in-plane) at dimensions mentioned above as evident in Figure 4-5, Figure 4-6, and Figure 4-7. It can also be noted that strong magnetic coupling is exhibited due to the anti-parallel alignment of the cells.

In Figure 4-5, there are several nano-magnetic cells with very irregular shapes, irregularly spaced, and with uneven surfaces. The AFM images clearly show the surface roughness where the SEM images present the shape irregularities, cell spacing, and cell spatial orientation. Here it can be seen that even if the magnet did not have a uniform shape and neighbors are not completely parallel to one another, that single domain magnetic dipole moments still formed and data propagation still occurred, evident via the anti-parallel coupling of cells 5 through 10 (left to right). Cells 1 and 2 had an
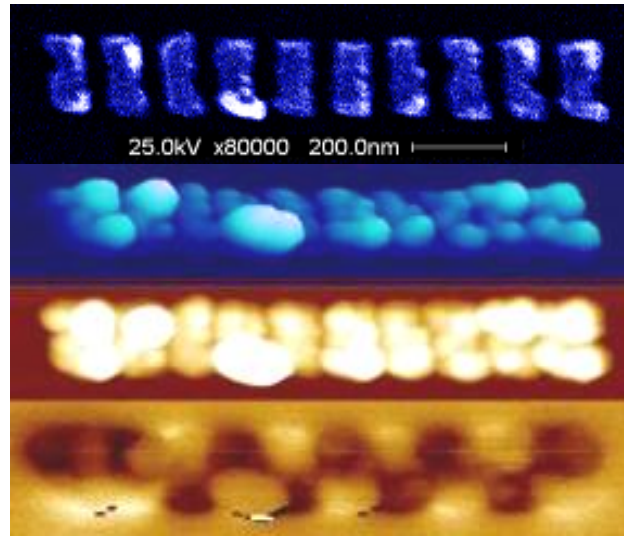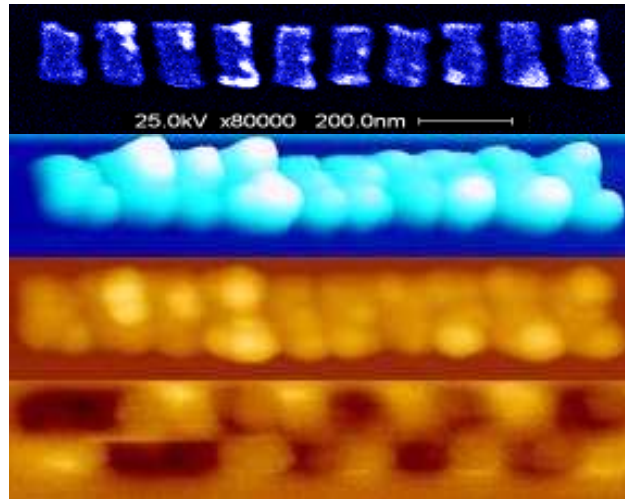
46
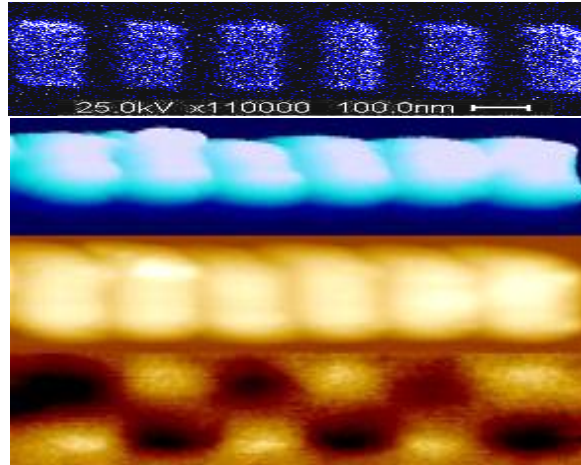
Figure 4-7 is another four different sets of data of an ideal MCA wire. The top figure is a SEM image followed by a 3D representation of an AFM plot. Next is an image of a 2D AFM plot and the bottom image is a MFM phase plot. This is an ideal chain, where the shape of the cells was regular and the surface roughness had been reduced. As a result the single domain dipole moments are were strongly coupled with no magnetic frustrations.

unwanted coupling state which can be attributed to the surface irregularities. It is also noted that where there are large protrusions on the surface of a cell, the magnetic moment seems to be voided as evident in cell 4.

Figure 4-6 is a different chain of nano-magnets. Overall the various cells had a smoother surface and more regular shape than the chain presented in Figure 4-5. Cells 2 and 4 had large bulges on the surfaces and the MFM image depicted magnetic voids in corresponding areas. Cells 2 and 3 were in an undesired configuration, with like orientations of their magnetic moments, which was attributed to the irregular surfaces. It was also noted that even though cell 1 had a very irregular shape (almost square) it still managed to form a desired single domain magnetic moment.

Figure 4-7 was an ideally fabricated chain of nano-magnetic cells. It was seen that the shape, surface, spacing, and orientation were better than that of the previous chains mentioned above. In this fabricated chain of nano-magnetic cells, there was no configuration errors, all magnets were in an anti-parallel orientation and thus

47

propagating information correctly. This could mainly be attributed to the surface evenness of the nano-magnetic cells.

These experiments demonstrated that for an anti-ferromagnetic coupling scheme, shape uniformity was a much more lenient requirement than the surface roughness for reliable data propagation. Several irregularly shaped rectangular nano cells were able to establish single domain magnetic moments. The irregularly shaped cells were also able to propagate data to neighboring cells which was exhibited via an anti-parallel magnetic coupling. It was noted that configuration errors, where neighbors have similar magnetic dipole moment orientations, occurred near cells that had irregular surfaces. The reliability of anti-ferromagnetic MCA wires therefore relied on the fact the surface must be uniformly smooth in order to propagate data properly.

The arrangement of how nano-magnets couple with one another and the robustness to fabrication defects was a more subtle aspect of MCA. As mentioned previously, an anti-ferromagnetic arrangement was susceptible to significant fabrication defects. In Figure 4-8, a ferromagnetic chain was shown with similar dimensions to the anti-ferromagnetic wires mentioned earlier in this section. The top image was an AFM image and the bottom was the corresponding MFM image. The AFM image clearly showed substantial irregularities in both shape irregularities and surface roughness. Similar types of defects showed magnetic frustrations in an anti-ferromagnetic wire, but the ferromagnetic wire demonstrated the robustness to such defects in the MFM image of Figure 4-8. The reproducibility of ferromagnetic coupling in wires with surface irregularities was confirmed in Figure 4-9. Overall, ferromagnetic coupled wires were found to be more robust to fabrication defects when compared to anti-ferromagnetic MCA wires due to coupling energies and is explored in Chapter 5.
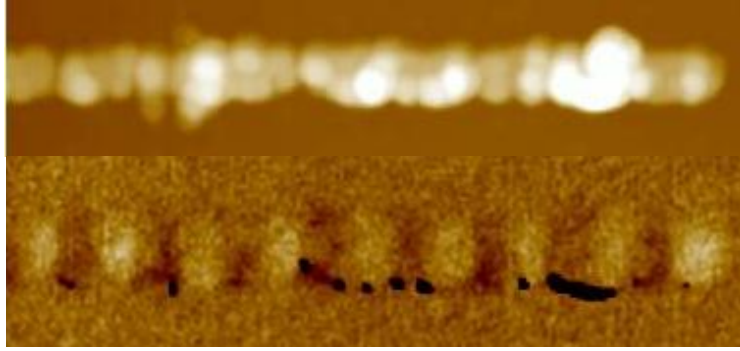
Figure 4-8 is an AFM amplitude height plot of a ferromagnetic chain which shows the highly irregular shape and surface roughness. The image on the bottom is the MFM phase plot of the chain and shows the single domain magnetic moments. In general ferromagnetic coupling was found to be more robust to large fabrication defects. The sizes of the nano-magnetic cells were 100(l) x 50(w) x 30(th) nm^3.
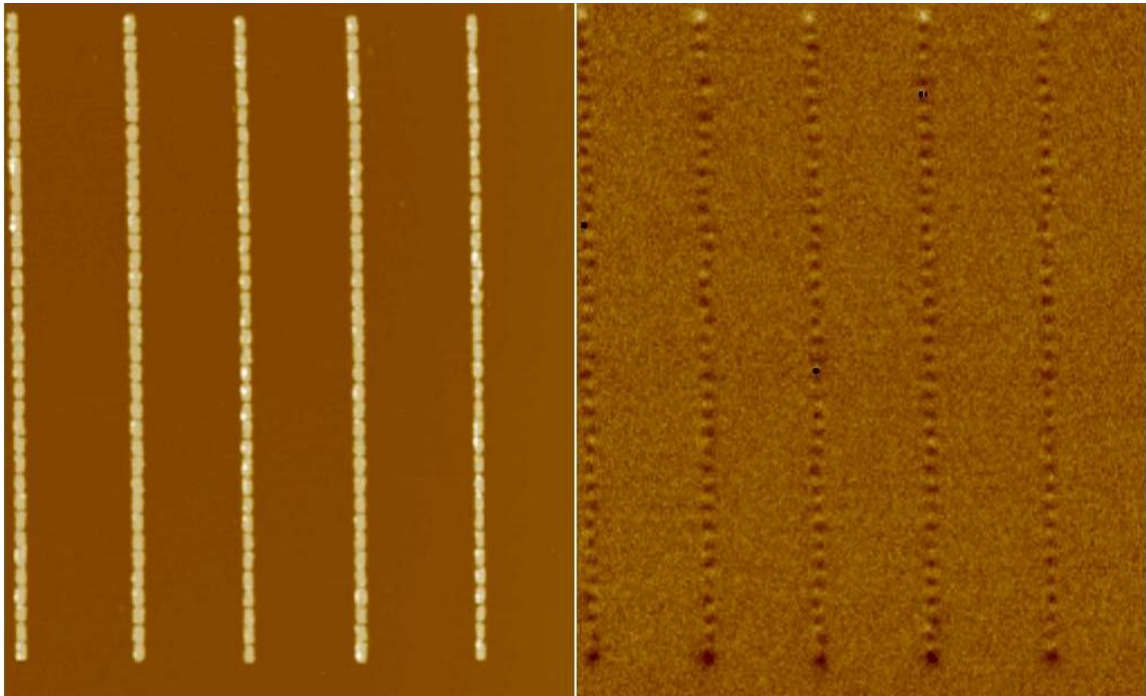
Figure 4-9 is the AFM height amplitude plot of five ferromagnetic chains (left). The image to the right is the corresponding MFM phase plot. Although the AFM image shows irregularities in the structures the MFM image shows the highly ordered coupling of the chains.

49

Although fabrication defects such as surface roughness, shape irregularities, and spacing irregularities may cause erroneous data propagation; these defects could be significantly reduced through the perfection of the fabrication process. The levels of irregularities, at these dimensions, needed to seriously affect the coupling dynamics was very significant and most fabrication defects could be avoided through the fine tuning of the fabrication process such as having a constant evaporation rate without significant evaporation spikes. Therefore it could be concluded that magnetic cells for MCA had the capability to mitigate erroneous coupling due to common fabrication defects. If the magnetic coupling of MCA cells were reliable it follows that more complicated arrangements of MCA should be able to perform complex logical operations.

Imre *et al.* demonstrated the first MCA logic gate to function at room temperature [14]. The gate was a majority voter which can also be considered to have the functionality of both a two bit OR gate or a two bit AND gate by fixing an input to a logical '0' or '1'. All the possible combinations of the 3 bit majority gate were demonstrated and Figure 4-10 is an expansion of the majority gate. The majority gate presented in Figure 4-10 had a total of 9 extra magnetic cells added to the logic gate's inputs and output then the previously reported gate. As can be seen in Figure 4-10, the logic operation performed a majority vote of the inputs given.

Figure 4-11 is a ferromagnetic majority gate, which was the first to be proposed and demonstrated. The difference between this layout and the previously reported MCA majority gate was that the coupling at the input cells as well as the output cells was ferromagnetic, unlike Figure 4-10 that had both ferromagnetic and anti-ferromagnetic coupling. As mentioned earlier in the section, ferromagnetic coupling seemed to be more

50
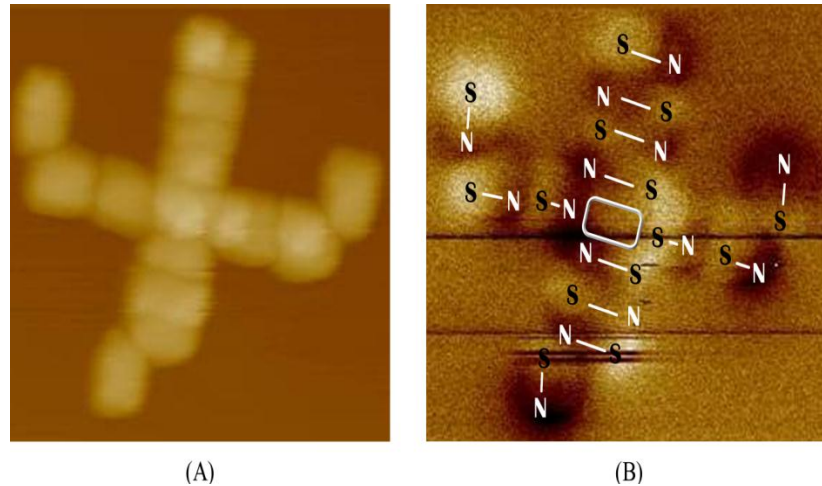
Figure 4-10 (A) is an AFM height amplitude plot of a MCA majority gate. Notice that there is anti-ferromagnetic coupling as well as ferromagnetic coupling in the design of the structure. (B) is a MFM phase plot. The poles have been overlaid with identifiers to help interpret the image. The rectangle in the center outlines the voter cell which "votes" based on the inputs. The inputs were the vertical cells at the bottom, left and right of the image.

robust to fabrication defects. The AFM image of the ferromagnetic majority gate shown in Figure 4-11 (A) clearly showed some surface roughness present. The logic operation of a ferromagnetic majority gate also differed from the previously demonstrated mixed coupled gate. The logical state of a wire was defined by the direction of the informational flow as shown in the MFM image Figure 4-11. The white arrows represented the inputs to the voter cell which was outlined by a white rectangle. Based on the given inputs to the voter cell, the correct output was propagated along the black arrow. What was particularly interesting about the configuration in this MFM image was the opposing result of the voter cell to the vertical input wire. The fact that the voter cell was opposed to the vertical input wire was a direct result of the dipole moments provided by the horizontal inputs. This demonstrated the functionality of the voter cell responding to the inputs provided by the gate and shows the possibility of a ferromagnetic MCA majority gate structure.

51

(A)   (B)
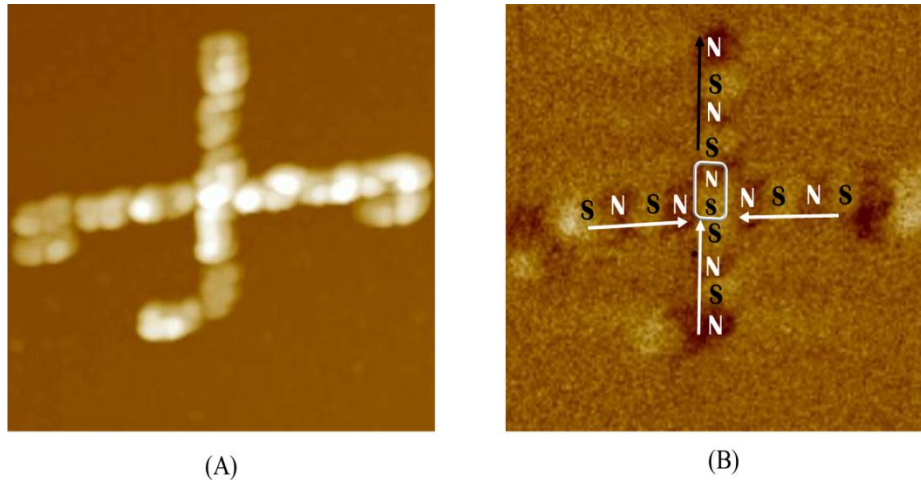
Figure 4-11 (A) is an AFM height amplitude plot of a ferromagnetic MCA majority gate. Notice that all the coupling between the input chains and the output chains were ferromagnetic. (B) is the corresponding MFM phase plot. The poles have been overlaid with identifiers to help interpret the image. The rectangle in the center outlines the voter cell which "votes" based on the inputs. An important configuration to notice is the voter cell has voted based on the two horizontal input chains and opposed the vertical input chain.

Figure 4-12 was a set of ferromagnetic majority gates feeding into a third majority gate. This was one of the largest systems of MCA logic to be demonstrated. There was one magnetic frustration found in the entire system. Through experimentation it was found that one frustration was predictably present in a three majority gate system. It was also important to note that there was not a frustration at the voter cell; all magnetic frustrations had been found at the peripherals of the gates. Since ferromagnetic coupling was determined to be reliable, as shown in several examples in this chapter, it was reasoned the issue arose from the ability to control informational flow. How the magnetic system was driven from input to output was a non-trivial issue. It was also reasoned that propagation errors, such as the one shown in Figure 4-11, were directly related to the fact that there was no control of where the data started and ended.

Without a means of synchronous computation via a clocking mechanism, magnetic frustrations and the orderly operation of logic would not be possible. The following

52
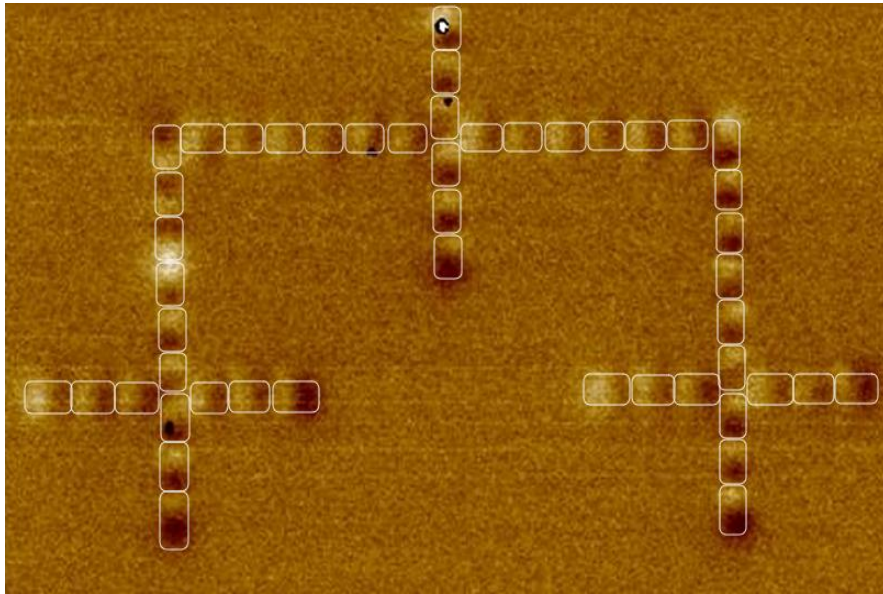
Figure 4-12 is a MFM phase plot of two ferromagnetic MCA majority gates feeding into a third majority gate. All voter cells in the design had no magnetic frustrations.

chapter explores how different types of external fields interacted with ferromagnetic and anti-ferromagnetic MCA wires along different magnetization axes. By studying the interaction of MCA wires with an external clocking field a more realistic clocking mechanism may be realized. A thorough understanding of signal propagation, switch delay, and system clocking will be a necessity if MCA logic systems are to materialize as a viable technology.

53

Chapter 5

Magnetic Cellular Automata Interconnects

5.1 Introduction

In order for any logic machine to work, there must be communication between the various logic components throughout a design. One can observe this at several different levels throughout the design automation process with transistor technology. From individual transistor level, to inter-gate signaling, or the signaling between logical black boxes, the interconnecting wire is fundamental to every aspect of any logic system. Without a means of communicating results from one logic structure to another, computation is inconsequential. Hence, the reliability of an interconnecting wire providing accurate information is crucial to the functionality of a system. In MCA, there have been wires prototyped demonstrating a high order of coupling [23]; encouraged by these results, similar work was produced and the results indeed verified successful operation [91].

To progress towards implementing more complex circuitry, it was necessary to control information propagation of an interconnecting wire via a clock. Csaba *et al.* proposed using an adiabatic clocking method that used an external magnetic field [13]. The external magnetic clocking field saturated the nano-magnets, causing the overall magnetic dipole moment to align itself along the in-plane hard axis of the nano structure. The clocking field would then be reduced as an input was provided. The study

54
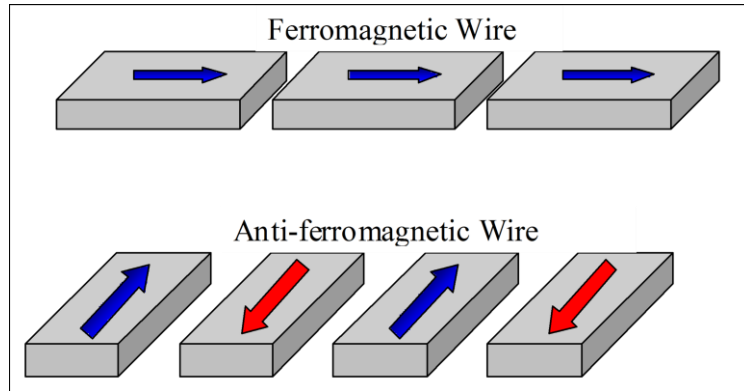
Figure 5-1 depicts correct data propagation for ferromagnetic and anti-ferromagnetic wires, which are the lowest ground state energy. For the ferromagnetic wire the magnetic dipole moments are oriented in the same direction, where anti-ferromagnetic wires are in opposing directions.

of wire architectures under such clocking fields was significant to the advancement MCA systems and presented here.

5.2 Wire Architectures

In MCA there were two types of interconnects that had been proposed, ferromagnetic coupled wires and anti-ferromagnetic coupled wires. The different types of interconnects were created through fabricating the wires in the different arrangements shown in Figure 5-1. For both wire architectures the desired state was always the lowest possible local energy minimum. Since magnetic systems worked to lower their overall magnetization energy MCA has taken advantage of the physics.

Anti-ferromagnetic wires had several intriguing factors associated with them, such as a built in inverter. When information was properly propagated down a wire each magnet had the inverted state of its immediate neighbor as shown in 1. This occurred due to the repulsion forces experienced by similar magnetic poles. A logical

55
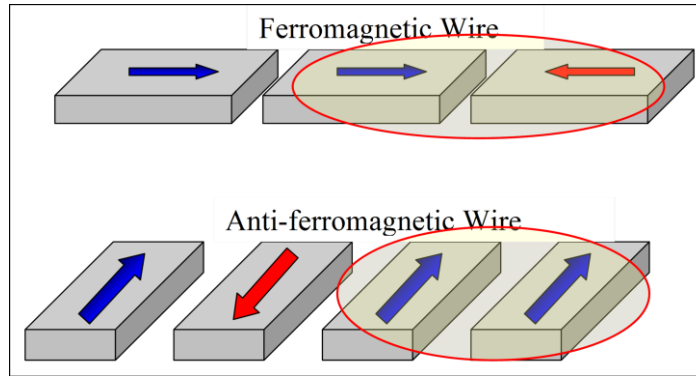
Figure 5-2 depicts incorrect data propagation for ferromagnetic and anti-ferromagnetic wires. The presence of like poles in close proximity makes this an undesired high energy state. This is called a magnetic frustration.

error occurred when neighboring magnets had like states, shown in Figure 5-2. This is known as a magnetic frustration because of the high demagnetization energy experienced by pinning like poles next to each other.

Ferromagnetic wires were arranged in a head to tail fashion as shown in 1. Data propagation occurred through magnetic field interactions of each cell. Proper logical exchange occurred when all magnetic dipole moments were arranged in the same direction as shown in 1. Magnet frustrations occurred when neighboring cells had dissimilar magnetic dipole moments as depicted in Figure 5-2.

In the proceeding sections the first experimental results were presented comparing shape engineered ferromagnetic and anti-ferromagnetic wires under various magnetic clocking fields. The experimental observations show that ferromagnetic wires were less likely to have magnetic frustrations. Simulations were also implemented which bolster the conclusion that ferromagnetic wires operate in a more reliable manner than anti-ferromagnetic wires.

56

5.3 Fabrication Process

The electron beam lithography process began by coating a Si wafer with a resist, namely PMMA. This was accomplished by using a Laurell Technologies WS-400A-8NPP/Lite Spin Processor, which spun the wafer at high speeds causing the PMMA resist to spread evenly over the entire wafer. A bilayer PMMA recipe using a 495K molecular weight as the bottom layer and 950K molecular weight as the top layer was chosen. The bottom layer was spun, then baked, followed by the top layer being spun then baked. The purpose of the bilayer PMMA was to ensure a clean liftoff which was aided by the undercutting profile created in the low molecular weight PMMA.

A pattern was designed using DesignCAD2000 NT. The most effective line spacing, exposure doses, points, and focus were determined by using diagnostic designs such as the wheel pattern. A sample of the Si wafer coated with bi-layer PMMA was then loaded into the JEOL 840m retrofitted with the NPGS lithography system and a beam blanker. The SEM was then focused and the stigmation was adjusted for optimal resolution. The pattern was selected and written via the NPGS system. Afterwards, the sample was unloaded and prepared for chemical development. It was placed in a bath of MIBK and Isopropanol (1:3) for approximately seventy seconds, followed by a twenty second Isopropanol bath, and finally nitrogen dried.

Permalloy (Ni80Fe20), was then deposited via a Varian Model 980-2462 Electron Beam Evaporator in a vacuum of approximately 5 µTorr at a rate of 2 Å sec^{-1}. The sample coated with the ferromagnetic material was placed in a heated ultrasonic acetone bath for approximately 15 minutes which selectively lifted off the unwanted PMMA and left the fabricated magnetic structure intact.

57

(A)

(B)
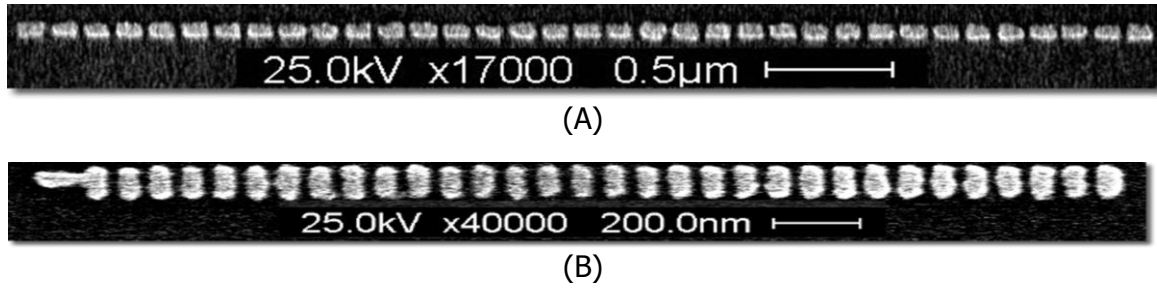
Figure 5-3 (A) is an SEM image of the ferromagnetic wire and (B) is of the anti-ferromagnetic wire. The dimensions of the magnets were approximately 100 (l) x 50 (w) x 30 (th) nm^3.

5.4 Experimental Setup

The specific ferromagnetic and anti-ferromagnetic wires used for the experiment are shown in Figure 5-3. A Veeco DI 3100 was used to collect all Magnetic Force and Atomic Force Microscopy data. SEM metrology was accomplished using a Hitachi S-800. The dimension each nano-magnetic cell was approximately 100 (l) x 50 (w) x 30 (th) nm. The spacing between each cell was approximately 20 nm and the nano-magnets were not annealed.

An electromagnet powered by a 300W regulated dc power supply was used to provide uniform magnetic fields of approximately 200mT (2000 Gauss). A NIST traceable Gauss meter from AlphaLab Inc. was used to measure the fields provided by the electromagnet. The remanent magnetization was recorded via Magnetic Force Microscopy and the binary states of a nano-magnetic cell were enumerated based on the alignment of the magnetic dipole moment along the easy axis.

The following procedure was used to provide the different directions of external magnetic excitations to the MCA wires. The sample was placed inside of an electromagnet which had an approximate remanent field of 0T. It was followed by a

58

(A)

(B)
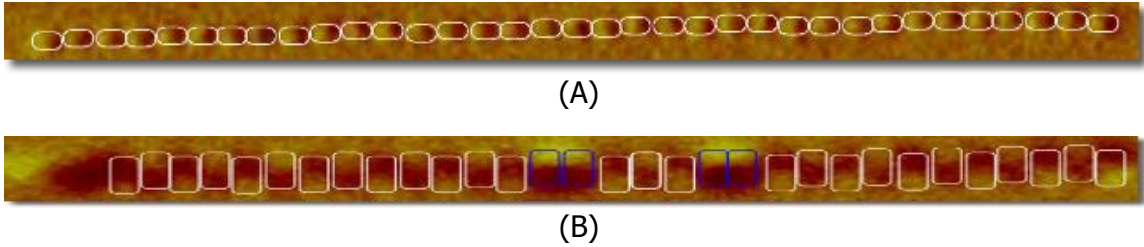
Figure 5-4 (Spin magnetic field) (A) is a MFM image of the ferromagnetic wire and (B) is the anti-ferromagnetic wire. There were very few frustrations in (B) and the ferromagnetic wire had no frustrations.

(A)

(B)
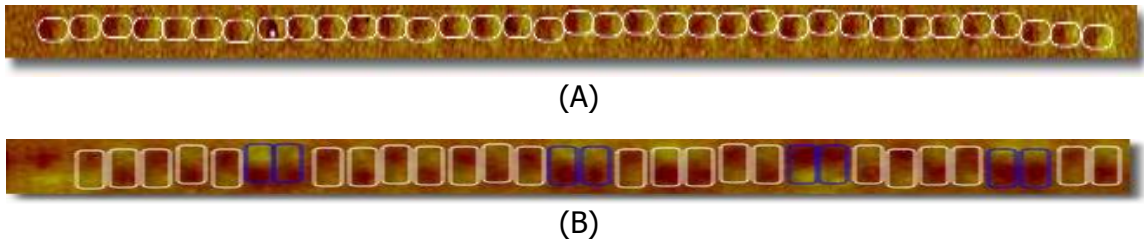
Figure 5-5 (Z-axis magnetic field) (A) is the ferromagnetic wire and (B) is anti-ferromagnetic wire. The number of incorrect alignments increased in (B). The ferromagnetic wire had no frustrations.

(A)

(B)
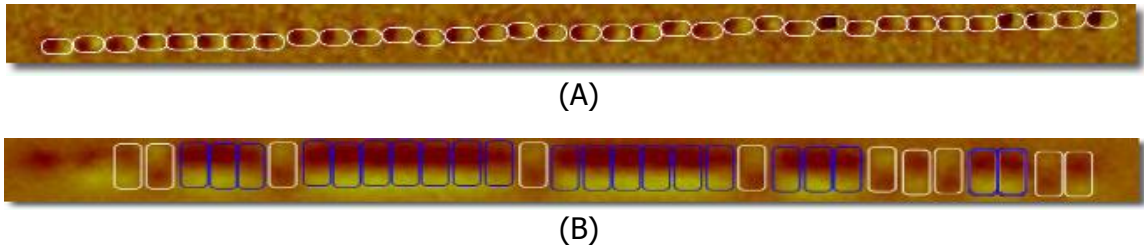
Figure 5-6 (Easy axis magnetic field) (A) is the ferromagnetic wire and (B) is anti-ferromagnetic wire. In (B) there was a significant amount of frustrations. For anti-ferromagnetic wires, this type of clocking field is was undesirable. The magnetic moments must overcome the shape anisotropy energy to align in an anti-ferromagnetic fashion. The ferromagnetic wire had no frustrations.

(A)

(B)
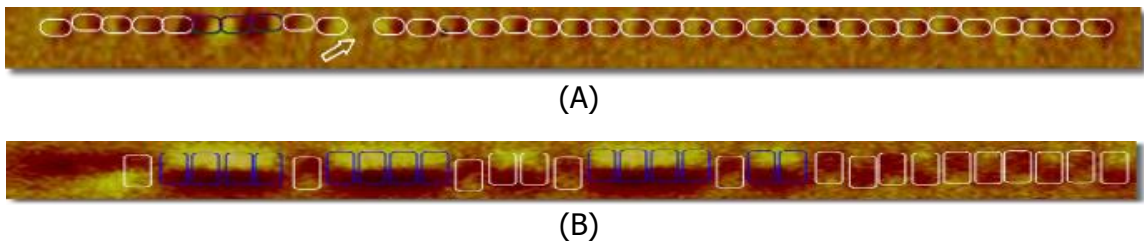
Figure 5-7 (Hard axis magnetic field) (A) is the ferromagnetic wire and (B) is anti-ferromagnetic wire. In (A) an interesting configuration occurred as pointed out by the arrow. The cell's magnetic dipole moment appeared to be void. It can could be seen that the cell is was surrounded by like poles, hence forcing the peculiar state.

59
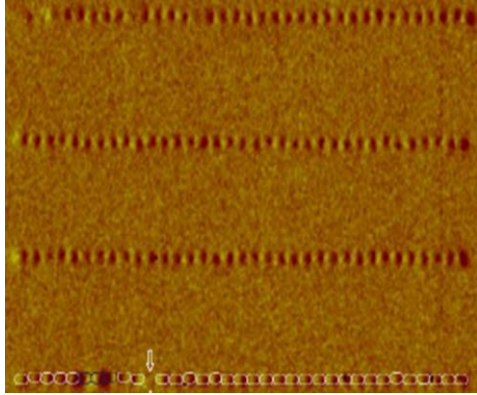
Figure 5-8 is an MFM image where a magnetic field was provide to ferromagnetic wires along the hard axis. The bottom most wire was the same wire shown in Fig 5-7. Although that particular wire had frustrations, the three neighboring wires above it did not.
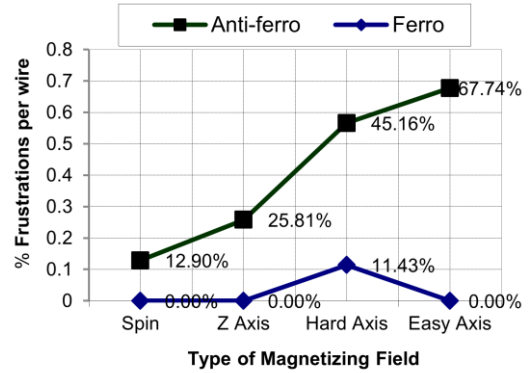
Figure 5-9 is a graph which summarizes the percentage of frustrations per wire based on the direction of the magnetic field. The field strength for all fields was approximately 200mT (2000 Gauss).

ramp up period of approximately 2 seconds to 200mT. The sample was left in the saturating field for 5 seconds, followed by a ramp down over 2 seconds.

Simulations were calculated using the NIST provided OOMMF tool. The following parameters were used to simulate Permalloy systems via OOMMF; magnetic saturation (M_s) 860e3 A/m, exchange stiffness (A) 13e-12 J/m, and a damping co-efficient 0.5.

5.5 Results

In Figure 5-4 through Figure 5-7, the MFM images depict the remanent magnetization of both the ferromagnetic (top) and anti-ferromagnetic (bottom) MCA wires. Each individual magnet has been overlaid with an outline to help interpret results. A blue outline was used to point out an undesired condition, i.e. a frustration.

In Figure 5-4, the wires were rotated while inside of the magnetic field, similar to the method used by Bernstein *et al.* [24]. The magnetic field was provided to both wire architectures using the procedure outlined above. Afterwards, the nano-magnets were allowed to settle into the lowest possible ground state. As shown in Figure 5-4, there

60

were a few frustrations present in the anti-ferromagnetic wire architecture. Interestingly, the ferromagnetic wire was able to reach the lowest possible energy state with no frustrations present.

In Figure 5-5, the magnetic field was provided along the z-axis of the wires (out-of-plane hard axis). This aligned the magnetic moments in a high energy state due to the shape anisotropy of the nano-magnets. The field was removed and the wires were allowed to settle. It was evident that the number of frustrations present in the anti-ferromagnetic wire architecture increased, whereas the ferromagnetic MCA wire architecture was able to settle with no frustrations.

Similarly, in Figure 5-6, a magnetic field was provided along the easy axis of the magnets for both wire architectures. In this instance, the differences in behavior between the architectures became clearly evident. For the anti-ferromagnetic wires this was the least desirable type of field to provide. It forced the magnetic moments of each magnet to arrange itself in a high energetically unfavorable state, by forcing repelling poles to exist next to each other. Once the field was removed, the repelling forces of like poles must overcome the shape anisotropy energy to align in a more energetically favorable anti-ferromagnetic state. It was clear that the number of frustrations in Figure 5-6, for the anti-ferromagnetic wire architecture, was significantly worse. In the case of the ferromagnetic wire architecture though, this would clearly be the preferred type of field to provide. Since the magnetic field lies along the easy axis of the nano-magnets, this would lead to the least amount of frustrations for the ferromagnetic wire architecture.

In Figure 5-7, the magnetic field was provided along the in-plane hard axis of the nano-magnets. This forced the magnetic moments to align themselves in an unfavorable

61

state due to the shape anisotropy of the nano-magnets. Once the magnetic field was removed, the magnetic moments attempted to align themselves along the easy axis of the nano-magnetic cells. In the anti-ferromagnetic wire, there were several frustrations present. The ferromagnetic wire also showed some susceptibility to magnetic frustrations, with a few undesired states. A very interesting configuration is pointed out by an arrow in Figure 5-7. There were two similar poles on either side of the nano-magnet. The magnetic moment for the trapped nano-magnetic cell appears to absent. It is possible that the stray field of the out of plane magnetic moment was too weak for the MFM to detect.

In Figure 5-8, the ferromagnetic wire from Figure 5-7 was the bottom most wire. As can be seen in the image, there were three neighboring wires above it. The MFM image shows all three neighboring wires were able to reach a ground state with no magnetic frustrations. So although the ferromagnetic wire in Figure 5-7 did have some frustrations present, when providing a field along the in-plane hard axis, neighboring wires did not.

The graph in Figure 5-9 summarizes the number of frustrations for both architectures for a given type of magnetic field. This experimental data suggested that the ferromagnetic MCA wire architecture could be more robust to fabrication defects than the anti-ferromagnetic wire and was more likely to reach a lowest possible ground state than the later.

OOMMF solved a given problem by integrating the Landau-Lifshitz equation (5-1), where M was the point-wise magnetization, H_{eff} was the effective magnetic field, $\bar{\gamma}$ was the gyro-magnetic ratio, and α was the damping co-efficient. H_{eff} was calculated in Eq.

Table 5-1 provides various energies associated with a two nano-magnet ferromagnetic and anti-ferromagnetic system. It captured the two possible states of both schemes, namely the ground state and meta-stable state.

Architecture States (G=ground, M$_S$=meta-stable)	Exchange Energy (J /m^3)	Demag Energy (J /m^3)	Total Energy (J /m^3)
↑ ↑ (M$_{eta}$)	3255.46	56798.92	60054.38
↓ ↑ (G)	3918.31	43112.37	47030.69
← ← (G)	1365.99	50932.46	52298.45
→ ← (M$_{eta}$)	2687.185	67491.31	70178.49

(5-2), where E was the total energy of the system. The total energy E, calculated in Eq. (5-3), described the total average energy density of all the magnetically active elements where; E_z was the Zeeman energy, E_d was the demagnetization energy, $E_{ex,}$ was the exchange energy, and E_A was the anisotropy energy [92].

$$\frac{d\mathrm{M}}{dt} = -|\bar{\gamma}|\,\mathrm{M}\times\mathrm{H}_{eff} - \frac{|\bar{\gamma}|\alpha}{M_s}\mathrm{M}\times(\mathrm{M}\times\mathrm{H}_{eff}),\qquad(5\text{-}1)$$

$$H_{eff} = -u_0^{-1}\frac{dE}{dM},\qquad(5\text{-}2)$$

$$E_{Total} = E_Z + E_D + E_{EX} + E_A,\qquad(5\text{-}3)$$

The total energy density of all magnetic elements (E) from the simulation is highlighted in dark blue in Table 5-1 for both the desired ground state (G) and a meta-stable state (M$_{eta}$) for anti-ferromagnetic and ferromagnetic architectures. Interestingly, it was worth noting that the total energy of both possible states for the anti-ferromagnetic scheme was lower than the total energy of the equivalent ferromagnetic state. At first glance this would lead one to believe anti-ferromagnetic wires would act more reliably, but this does not capture the observed results. In the experiments above,

63

the ferromagnetic scheme was able to minimize the total number of frustrations and therefore operate in a more reliable manner.

These results are attributed, but not limit too, the ferromagnetic wires ability to mitigate frustrations more so than the anti-ferromagnetic wires due to the energy difference between the two possible states for the local architectures, also known as the kink energy. The kink energy was defined in Eq. (5-4) where; U_{MS} was the energy associated with the meta-stable (frustrated) state, and U_G was the energy associated with the desired ground state.

$$E_{Kink} = U_{MS} - U_G,$$ (5-4)

Figure 5-10 shows an abstraction of the experiment carried out above where the external magnetic field was given along the z-axis. When the system was forced to align itself along the z-axis, the total energy was very high, and once the external field was removed both architectures attempt to minimize their local energies. As mentioned above, the total energy of the desired state for the anti-ferromagnetic wire was lower than that of the ferromagnetic wire. Nevertheless, this was not considered by the locally implemented architectures, only the kink energy or the energy between the possible ground and meta-stable states for the particular architecture was present at the time the external field was removed. As shown in Figure 5-10, the kink energy for the ferromagnetic wire was much greater than the anti-ferromagnetic wire, and therefore, the ferromagnetic architecture had a higher propensity to mitigate undesired frustrations.

The nucleation of frustrations in the experiments for both wire architectures were primarily attributed to a multiple driver scenario. Without an input driving the system, it was highly probable for a wire to have multiple drivers. This could be explained by

64
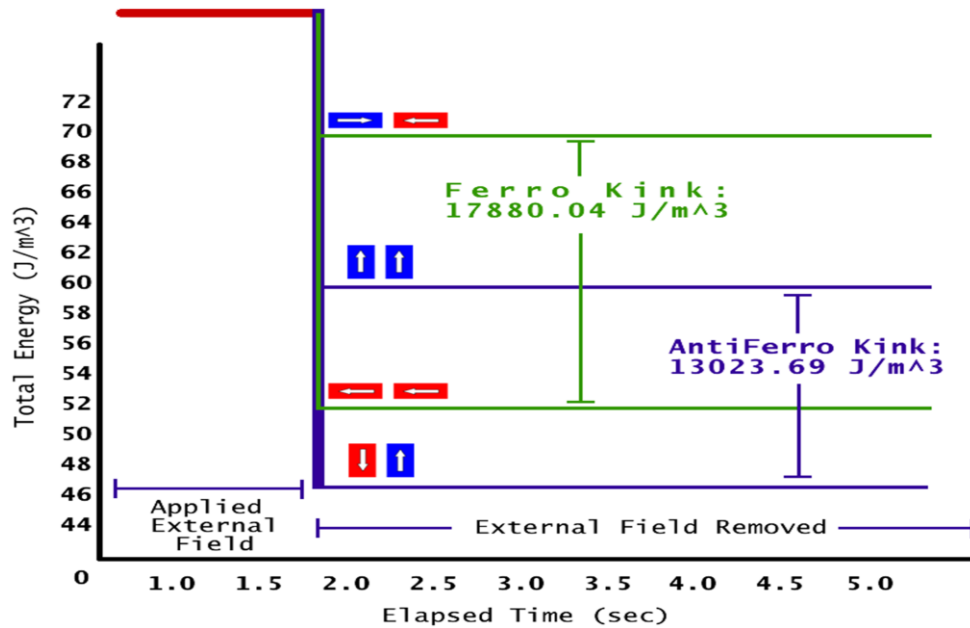
Figure 5-10 shows the possible states for the ferromagnetic and anti-ferromagnetic wires and over the duration of the experiments. The higher kink energy for the ferromagnetic wire provided an explanation of its greater ability to mitigate unwanted frustrations.

picturing a wire in a clocked state along the hard axis. Once the magnetic clocking field was removed, any nano-magnetic cell in the chain could become the driver to its neighbor. In fact, multiple drivers could occur throughout a wire, in opposing directions. This lead to magnetic frustrations and was not representative of the ideal operation of a MCA system.

A more ideal ferromagnetic wire situation was implemented in a simulation and is shown in Figure 5-11 and Figure 5-12. A driver was present as well as a clocking field. In Figure 5-11 and Figure 5-12, the leftmost magnet was used as the driving input cell by providing an external input field to this particular magnet only. The rest of the wire was in a clocked state, where a saturating magnetic field was provided along the in-plane hard axis. The clock was released instantaneously and the wire was allowed to settle. As shown in Figure 5-11 and Figure 5-12, the ferromagnetic wire settled according to the driver. For the experiment above, providing the clocking field along the

65
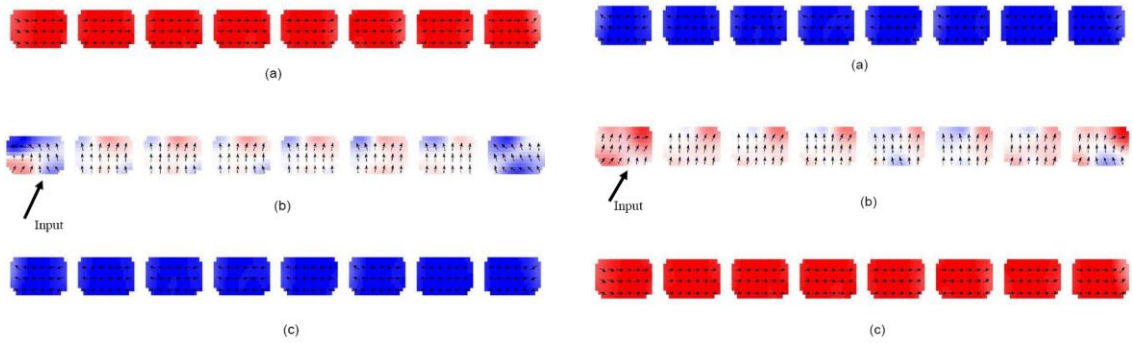
Figure 5-11 shows three snapshots of a chain switching from '0' to '1'. At time step (a) the ferromagnetic wire was in an initial state of '0'. At time step (b) a clocking field was given and an input of '1' was provided. As can be seen at time step (c) the chain completely switched to match the driver cell.

Figure 5-12 shows three snapshots of a chain switching from '1' to '0'. At time step (a) the ferromagnetic wire was in an initial state of '1'. At time step (b) a clocking field was given and an input of '0' was provided. As can be seen at time step (c) the chain completely switched to match the driver cell.

in-plane hard axis lead to only a few frustrations, but in simulation with an input present the wire operated as desired.

5.6 Conclusion

Two types of MCA wire architectures were fabricated; ferromagnetic and anti-ferromagnetic. By providing clocking fields to the wires, and investigating the remanent magnetic dipole moments, the results revealed ferromagnetic wires to exhibit exceptional data propagation. The ferromagnetic wires' superior ability to mitigate frustrations over the anti-ferromagnetic wires was attributed to the higher kink energy of the ferromagnetic scheme. Providing a clocking field along the z-axis of the nano-magnets, where experimentally there were no frustrations found in the ferromagnetic architecture, would eliminate possible clocking complexities encountered in dense layouts that contain in-plane wires at different angles. A practical and feasibly simplistic clocking method could then be implemented for ferromagnetic wire architectures by providing the clocking field along the thickness of the magnetic cells.

66

Magnetic Cellular Automata does not have to be limited to just one type of wire architecture per design though. Indeed, the ferromagnetic wires could be mixed with the anti-ferromagnetic wires in the same design and there could be some circumstances where one would be more desirable than the other. The data suggested that for relatively long data propagation, the ferromagnetic wire architecture would be the preferred implementation for MCA systems.

Chapter 6

Magnetic Cellular Automata Coplanar Cross Wire Systems

6.1   Introduction

The novelty of Cellular Automata (CA) and the associated fabrication difficulties created a great opportunity for experimental research to be conducted. An Electronic Quantum Cellular Automata (EQCA) proof of concept cell was demonstrated to work, but the experiment was conducted at a temperature of 70 mK [93]. Due to the energies involved, the dimensions necessary for EQCA to work at room temperature were approximately a few nanometers. This created a challenge for current fabrication technology. This difficulty allowed for designs such as crossing wires to be theoretically proposed and critiqued, but required a physical actualization to make such architectures viable.

Tougaw *et al.* proposed the idea of coplanar wire crossings for EQCA, and explained that by physically rotating the electron sites by 45°, as shown in Figure 6-1 (C), two coplanar crossing wires could propagate information successfully [94]. Figure 6-2 (B) shows the crossing wire system propagating information. Wire 1 was propagating a logical 1, while wire 2 was propagating a logical 0. The cells in wire 2 had a 45° rotation in order to minimize any influence that it could have had on wire 1. Walus *et al.* explained that the 45° rotated junction cell had a null effect on neighboring cells of wire 1 regardless if it was propagating a '0' or a '1' [95]. Concerns are also expressed over coplanar crossing wires. Walus *et al.* states that 45° cross wires breaks the non-rotated

68
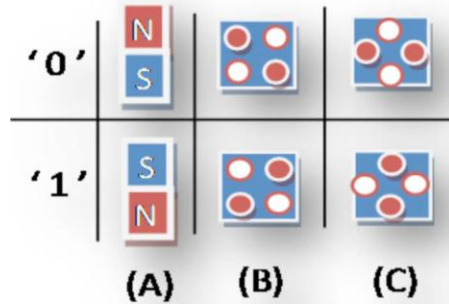
Figure 6-1 is a standard abstract representation of MCA and EQCA cells. The top row can could be interpreted as a logical zero and the bottom a logical one. (A) enumerates the nano-magnetic cells based on their magnetic dipole moments. (B) depicts the standard QCA cell. Two electrons are represented as red dots. The white dots are the alternate electron sites which the electrons tunnel to in order to reduce the cells overall energy in accordance with its neighbors. (C) shows the same EQCA cell only the sites are rotated by 45°. This is necessary for a cross wire layout in EQCA.
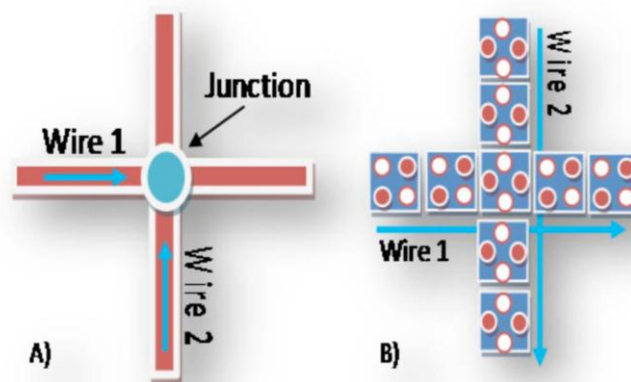
Figure 6-2 (A) is an abstract representation of two coplanar crossing wires. The area where the two wires cross is called the junction. Information propagation is shown via the arrows. (B) is a representation of QCA coplanar crossing wires. For traditional current carrying wires, the junction would create a source of error and this type of structure would not be viable.

wire into several weakly coupled segments [95]. This is due to the energies associated

with the columbic interactions of EQCA. Bhanja *et al.* further characterized various cross

wire architectures with triple modular redundancy, double-triple modular redundancy

and thick crossing wires in terms of polarization loss and thermal stability by modeling

the cross wire system as probabilistic Bayesian network model [38]. The coplanar cross

69
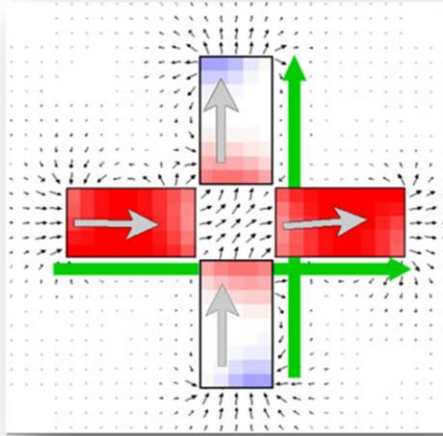
Figure 6-3 is an OOMMF simulation of our MCA cross wire system design. There are two ferromagnetic coupled wires outlined by the green arrows. The magnetic dipole moments of each nano-magnetic cell is represented by the grey arrows. The magnet moments lie along the easy axis of the nano-magnets.

wire systems were probabilistically inferred under various thermal conditions and the robustness was characterized under single missing cell defects.

The architecture was ported into a MCA construct by designing a ferromagnetic coplanar cross wire system. Figure 6-3 shows an abstract representation of the ferromagnetic cross wire system that was designed. It was composed of two perpendicularly intersecting ferromagnetic coupled wires.

As depicted by the green arrows, information was propagated along the two wires without a loss of information. The MCA cross wire systems were experimentally studied under various magnetic fields and the results are presented in the following sections.

6.2 Design

The design of the ferromagnetic coupled cross wire system is depicted in Figure 6-3. The orthogonal wires allowed for minimal interference between the crossing wires. The shape anisotropy created a preferred axis of magnetization which was also the ground states of the nano-magnet. The energy necessary to align the magnetic moment along

70

the hard axis was very high, therefore, the wires were designed perpendicular to one another. The magnetic fields produced by wire 1 interacted with the hard axis of the cells in wire 2, which mitigated undesired interference coupling.

The following parameters were used to simulate the Permalloy systems via OOMMF; a magnetic saturation of (Ms) 860e3 A/m, an exchange stiffness of (A) 13e-12 J/m, and a damping co-efficient of 0.5. The system's initial magnetization was along the thickness of the magnets. It was then allowed to settle into the ground state depicted in. It is worth noting that the interaction of the intersecting wires was neutral during the operation of the cross wire system due to the nature of ferromagnetic coupled wires. As can be seen in Figure 6-2, at the junction both north and south poles were presented to the other wire, which in essence produced a net cancelling effect. Thus, the wires were able to cross in the same plane with virtually no interference.

6.3   Fabrication Process

A Si wafer was coated with PMMA via a Laurell Technologies WS-400A-8NPP/Lite Spin Processor. It spun the wafer at high speeds causing the PMMA resist to spread evenly over the entire wafer. A single thin layer of 950K molecular weight PMMA was used. Afterwards, it was baked in an oven at 170°C to provide even heat over the entire wafer. This evaporated and removed any solvent left in the resist to ensure resist purity, which was critical to the nanometer electron beam lithography process.

The cross wire patterns were designed using DesignCAD2000 NT. The most effective line spacing, exposure doses, points, and focus were determined by using the diagnostic wheel pattern. A sample of the Si coated with 950K molecular weight PMMA was then loaded into the JEOL 840m retrofitted with the NPGS lithography system and a beam blanker. The SEM was then focused and the stigmation was adjusted for optimal results.

71
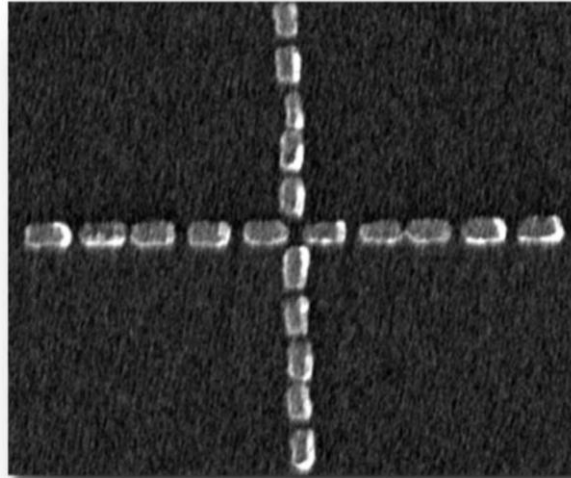
Figure 6-4 is a SEM image of the two coplanar cross wire system. Each cell was made of permalloy rectangles with the dimensions of 200(l) x 100(w) x 30(th) nm^3.

The pattern was selected and written via the NPGS system. Afterwards, the sample was unloaded and was ready to be developed. For this particular process, the developer, MIBK: Isopropanol 1:3 was cooled via liquid nitrogen. The sample was then developed at the sub-zero temperatures. This allowed for glassing to occur during the molecular chain scission process [81]. This resulted in sharper resist edges after development which translated to better defined edges for the nano-magnets.

Permalloy was then deposited, via the Varian Model 980-2462 Electron Beam Evaporator. A vacuum of approximately 2 μTorr was achieved and an evaporation rate of 2 Å sec^{-1} was used. Once the desired thickness of the material was deposited the liftoff process was done. The sample coated with Permalloy was placed in a heated ultrasonic acetone bath for approximately 15 minutes.

6.4   Experimental Setup

Two cross wires similar to the design shown in Figure 6-2 were fabricated. A Veeco DI 3100 was used to collect all Magnetic Force and Atomic Force Microscopy data. SEM

72
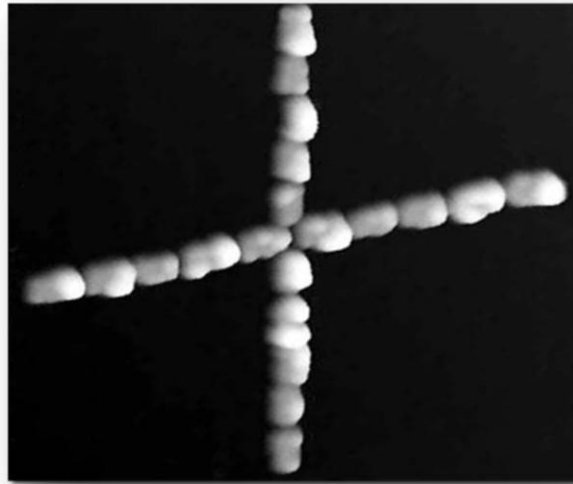
Figure 6-5 is an AFM image of the two coplanar cross wire system. The AFM height image captured the surface irregularities of the crosswire system.

metrology was accomplished using a Hitachi S-800. Figure 6-4 shows a topological SEM image of a simple cross wire system where each wire was composed of ten nano-magnets. Figure 6-5 is a 3D representation of an AFM image taken of the same cross wire structure. As can be seen in the SEM image, there were a few lateral spatial irregularities as well as some irregularly shaped cells. On average, most cells were approximately 100 x 50 nm^2 with a spacing of 20 nm between each cell. This was a non-ideal physical implementation of a ferromagnetic crosswire system, but if successful, would demonstrate the robustness of the system with respect to fabrication defects.

The following procedure was used to provide the various external excitations to the magnetic system via an electromagnet. The sample was placed inside the electromagnet followed by a ramp up period of approximately 2 seconds to 200mT along the thickness of the magnets. The sample was left in the saturating field for 5 seconds, followed by a ramp down over 2 seconds.
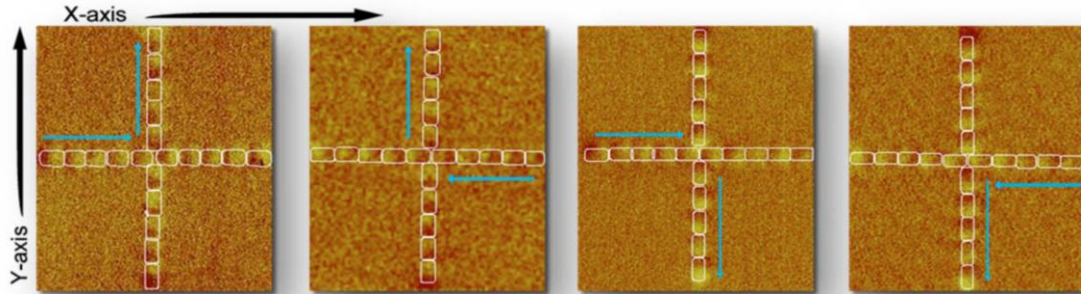
Figure 6-6 is a MFM image of all possible combinations for a simple cross wire system. White ellipses have been overlaid to outline each nano-magnet. The arrows represent the flow of data propagation for each wire.

Simulations were calculated using the NIST provided OOMMF tool. The following parameters were used to simulate permalloy systems; magnetic saturation (M_s) 860e3 A/m, exchange stiffness (A) 13e-12 J/m, and a damping co-efficient 0.5.

6.5 Results

A cross wire similar to the one shown in Figure 6-3 was fabricated. Figure 6-4 shows a topological SEM image of the cross wire system where wire 1 and wire 2 were each composed of ten nano-magnets. Figure 6-5 is a 3D representation of an AFM image taken of the same cross wire structure. By combining these types of metrology, a more accurate representation of the cross wire structure was obtained. In the SEM image, there were a few lateral spatial irregularities, as well as, some irregularly shaped cells. On average, most cells were approximately 100 x 50 nm^2 with a spacing of 20 nm between each cell. The AFM data allowed the surface roughness and thickness of the nano-magnets to be determined. In the 3D AFM image, the surfaces of the nano-magnetic cells were visibly non-uniform, with several peaks covering the surfaces. Previously, it was reported that surface roughness led to faulty data propagation for anti-ferromagnetic wires, here, the intent was to determine if surface roughness had a

74

Figure 6-7 is a SEM image of the complex cross wire system. The system consisted of six wires with nine junctions. Each wire was 20 nano-magnets long.

significant role in the coupling of ferromagnetic wires as well [91]. Bryan *et al.* also noted that edge roughness increased the coercivity of rectangular nano-magnetic structures [96]. The thicknesses of the cells are approximately 35 nm with a maximum peak height of 104 nm. We have determined, via bearing analysis, that approximately 55% of the surface is covered with peaks greater than 10 nm above the thickness. This presents a less than ideal case for the physical implementation of a ferromagnetic cross wire system, but if successful, could demonstrate the robustness to fabrication defects of the system.

Figure 6-6 shows the four possible combinations for data propagation in a two coplanar cross wire system. An external magnetic field was provided for stimulus and then removed. Afterwards, the system was allowed to settle in an energy minimum. The blue arrows represent the orientation of the magnetic dipole moments along the wires. As can be seen, there were no frustrations present in any four of the combinations and

75

the system reacted as expected. It is worth stating the particular system presented here was a non-ideal sample, due to the irregularities mentioned above. also important to mention that in all of the experiments with coplanar cross wires, frustrations at the most critical area of the system, namely, at the junction were never observed. The junction area can be considered as the four nano-magnetic cells where the two wires intersect each other, as shown in Figure 6-3. Due to the nature of magnets, if the junction performed in a reliable manner, any subsequent nano-magnetic cell in the wire would not experience signal loss. Meaning, for MCA coplanar cross wire systems, the wire was not segmented into smaller slices. The magnetization of the cell participating in the junction, once settled, would provide a self-gaining effect. This is due to the nano-magnet attempting to minimize its internal magnetic energy. For a nano-magnet neighboring the junction, the magneto-static energy it experiences would be similar to neighboring a cell in a traditional wire.

In an effort to determine if indeed the hypothesis of wires being self-gaining after the junction was true, in other words wires not becoming segmented into smaller sections at each junction, a more complex cross wire system was fabricated. The MCA system consisted of six wires, each 20 nano-magnets long, as shown in the SEM image Figure 6-7. Each magnet was approximately 100(l) x 50(w) x 35 (th) nm^3 and the system had a total of nine junctions. As mentioned before, an external field was provided for stimulus, removed, and then the system was allowed to reach a ground state. The arrows in Figure 6-8 depict the orientation of the magnetic dipole moment along the wires and there were no frustrations at any of the junctions. In fact, there were no frustrations in the entire system except in one location. This is highlighted in with a blue circle. This scenario was familiar and only occurred once in large complex
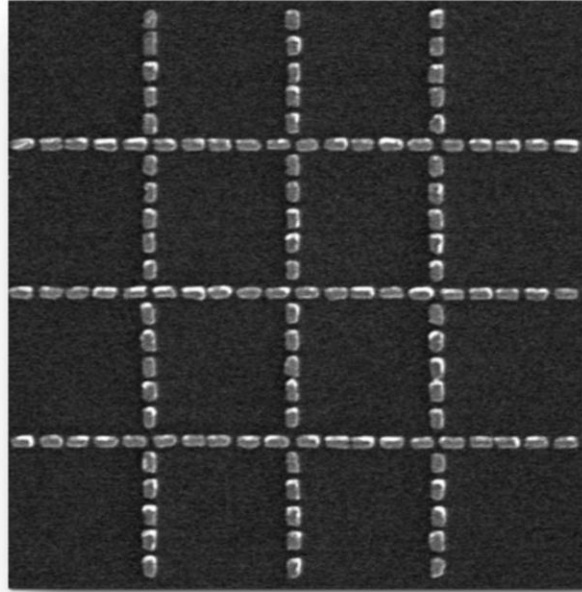
76
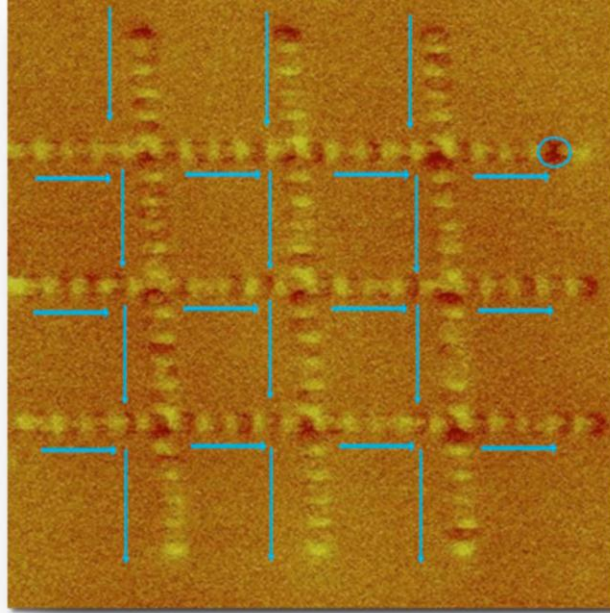
Figure 6-8 is a MFM image of the complex cross wire system. The system consisted of six wires with nine junctions. Each wire was 20 nano-magnets long. The blue circle shows the only magnetic frustration in the system.

system. Due to the complex nature of providing inputs and clocking fields at the nano-level, currently, the system was left to attain an energy minimum after the external field was removed. During this occurrence, a multiple driver scenario was created in the wire. As depicted in Figure 6-8, this occurred most frequently near the terminal locations of the wire. This result was found to bolster the viability of MCA as a technology. If a complex system such as this was able to attain an energy minimum on its own without the help of a driving input, it would seem that the system will be very capable of minimizing its total energy.

6.6 Conclusion

Unlike EQCA, where there was a rotated cell in the center of the junction (Figure 6-2 (B)), the design of an MCA cross wire system has a free area of space shown in Figure 6-3. The four possible logic combinations of a two coplanar cross wire system were

77

experimentally demonstrated, even though, physically, the system was less than ideal. This demonstrated the robustness of ferromagnetic coupled cross wires systems towards common fabrication defects. Furthermore, a complex cross wire system consisting of 120 nano-magnetic cells with nine junctions was fabricated and was able to reach an agreeable minimum energy. The concerns of segmentation of wires due to junctions, as in EQCA, did not seem to manifest themselves in these experimental investigations.

The results lead to the conclusion that MCA cross wire systems were inherently able to reach energy minimums and that ferromagnetic cross wire architectures were likely to be realized in MCA. This could possibly enable the technology to increase the density of switches, develop new layout algorithms to optimize space in the design automation process, as well as simplify the fabrication process by removing several multilayer alignment steps for signal propagation, thus increase yield.

Chapter 7

Magnetic Field-Based Computing for Image Processing

7.1   Introduction

The detection of significant features in an image is a computationally expensive process. The term perceptual organization is used to describe the act of recognizing important features of an image. It is generically broken down into three steps:

- Segmentation: extraction of features from an image such as edges, pixel intensity, etc.

- Grouping: relating low level segments of an image into larger perceptual groups such as surfaces, background, foreground, etc.

- Recognition: matching groupings identified as significant to a known model such as a building, human, etc.

Although each step has its own associated complexities, grouping is specifically important when reducing computational intensity. Particularly useful is the fact that grouping does not require exact computational accuracy, meaning that solutions that are near the optimal result are acceptable. The grouping of low level segments can be accomplished through a quadratic energy maximization process [40]. Traditional Boolean architectures found in supercomputers normally reduce problems such as the optimization of quadratic problems, into finding exact solutions to arithmetic problems and logical operations. This is very demanding on a Boolean system and is not

79

necessarily required for the grouping of visual objects, and magnetic nano-systems present a unique way to accomplish such a task [40].

The magnetic energy minimization of a nano system can provide sufficiently accurate solutions when variables are carefully mapped to nano-structures. The correlation between a variable from the segmentation of an image, in this case an edge, can be translated to a nano-magnetic disk. The magnetization of the nano-disk along a particular direction can then be related to the saliency of that particular variable (edge). The energy minimization occurs when neighboring magnets influence each other's magnetization vector through magnetic dipole field interactions. The magnetic dipole moments arrange themselves such that similar poles are far apart reducing the magneto-static energy of the system. The reduced form of the Hamiltonian for magnetic energy is given in equation (6-1), where M_i^z is the magnetization vector of nano-disk$_i$, M_j^z is the magnetization of a neighboring nano-disk$_j$, and E_{ij} is the quadratic energy term in terms of the distance between neighboring magnets given in equation (6-2) [40].

$$\mathrm{H} \approx \sum_i \sum_{j \neq i} M_i^z E_{ij} M_j^z \ , \tag{7-1}$$

$$E_{ij} = \frac{\mu_0 |V|}{4\pi d_{ij}^3}(3d_{ij}^3 - 1) \ , \tag{7-2}$$

In vision processing, edge grouping can be accomplished through assigning an affinity between edges based on factors, such as the angle between the edges, distance between edges, and continuity. Therefore, when grouping edges based on assigned affinities, the desire is to maximize the affinity energy. The affinity energy used here is

80

(A)   (B)   (C)
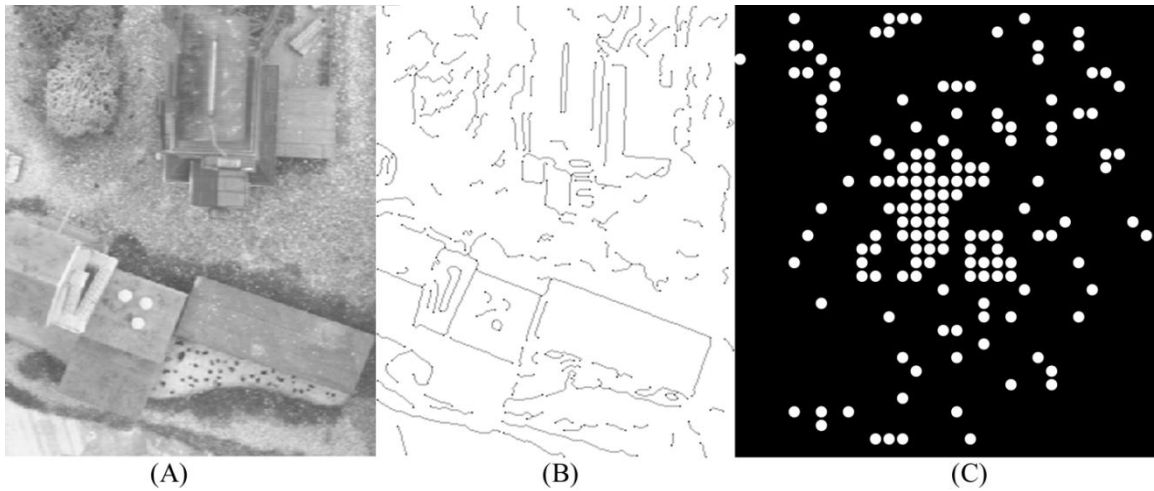
Figure 7-1 (A) is a grayscale image of a group of buildings taken from above. (B) is the same image post low level segmentation. (C) is the magnetic field based model where the white circles are nano-magnetic disk. The spacing between each magnet is carefully placed so that the quadratic dipolar interaction is proportional to the quadratic affinity between edges.

(A)   (B)   (C)
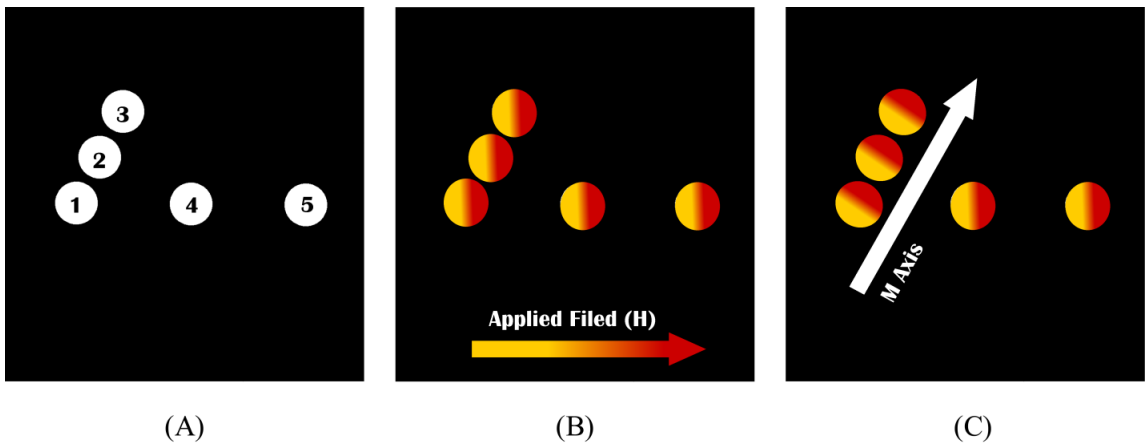
Figure 7-2 (A) is a layout of numbered magnetic nano-disk which correspond to the edges of an image. (B) depicts the magnetic initialization of the MFC system, where the red represents a positive pole and yellow represents a negative pole. (C) represent a possible ground state of the system after the external field is removed. If the magnetization is taken along axis M, the magnetization component of nano-disk 1, 2, and 3, will be larger than those of magnets 4 and 5.

81

given in equation (6-3), where x_i is an edge, x_j is another edge, and A_{ij} is the quadratic affinity term given in equation (6-4) [40].

$$A = \sum_i \sum_{j \neq i} A_{ij} x_i\, x_j \,, \qquad (7\text{-}3)$$

$$A_{ij} = \sqrt{l_i l_j}\, e^{\frac{-o_{ij}}{\max(l_i, l_j)}} e^{\frac{-d_{\min}}{\max(l_i, l_j)}} \sin^2(2\Theta_{ij}) \,, \qquad (7\text{-}4)$$

7.2   Proof of Concept

A Magnetic Field-based Computing (MFC) system is able to solve the edge grouping quadratic problem through the natural minimization of magnetic energy. By carefully spacing the magnetic cells such that the dipolar interaction energy E_{ij} is inversely proportional to edge affinity energy A_{ij}, the magnetization vector of the cells can then be related to the saliency of that edge [40]. If an image is given for feature detection, such as the one in Figure 7-1 (A), Figure 7-1 (B) is the low level segmentation of that image. The goal is to define a magnetic field-based computing (MFC) model, such as the one presented in Figure 7-1 (C), to determine the significant features of the segmented image, and group them together for the final recognition process.

A small MFC system consisting of five nano-magnets very similar to a subsection of Figure 7-1 (C) given in Figure 7-2 was the starting point of the study. The white circles represent magnetic nano-disks, enumerated from left to right. The disks were made of permalloy with the thickness being much less than the lateral dimensions to force in-plane single domain magnetic dipole moments. The experiment would proceed by applying an external magnetizing field along a particular direction as shown Figure 7-2 (B). Afterwards, the field would be removed and the magnetic cells would be allowed to

82

settle into a ground state as shown in Figure 7-2 (C). The natural tendency for magnetic energy to be minimized, in this case primarily due to magneto-static coupling, would lead magnets 1-3 to arrange themselves in a ferromagnetic fashion. It was also possible for magnet 4 to experience a degree of coupling with magnets 1-3 which could be demonstrated via an anti-ferromagnetic coupling. . The coupling exhibited by magnets 1-3 would be intentional since the inter-spacing distant was smaller than that of magnets 4 and 5, and would be part of the computational linear placement algorithm [40].

If the magnetization vector of each magnet is taken along axis M as shown in Figure 7-2 (C), the magnetization of magnets 1-3 would be greater than those of magnets 4 and 5. As mentioned previously, this magnetic interaction can be modeled via a quadratic term and is computational intensive but occurs naturally in the physical world, at least on the order of nano-seconds [97].   The magneto-static quadratic term was inversely proportional to the quadratic edge affinity, which determines the salient features of the image. So by setting appropriate affinity thresholds, the edges corresponding to magnets 1-3 would be regarded as a significant grouping, while magnets 4 and 5 would not.

7.3   Fabrication Process

A Si wafer was coated with PMMA via a Laurell Technologies WS-400A-8NPP/Lite Spin Processor. It spun the wafer at high speeds causing the PMMA resist to spread evenly over the entire wafer. A single thin layer of 950K molecular weight PMMA was used. Afterwards, it was baked in a convection oven at 170°C to provide even heat over the entire wafer. This evaporated any solvent left in the resist to ensure resist purity, critical to the nanometer electron beam lithography process.

83
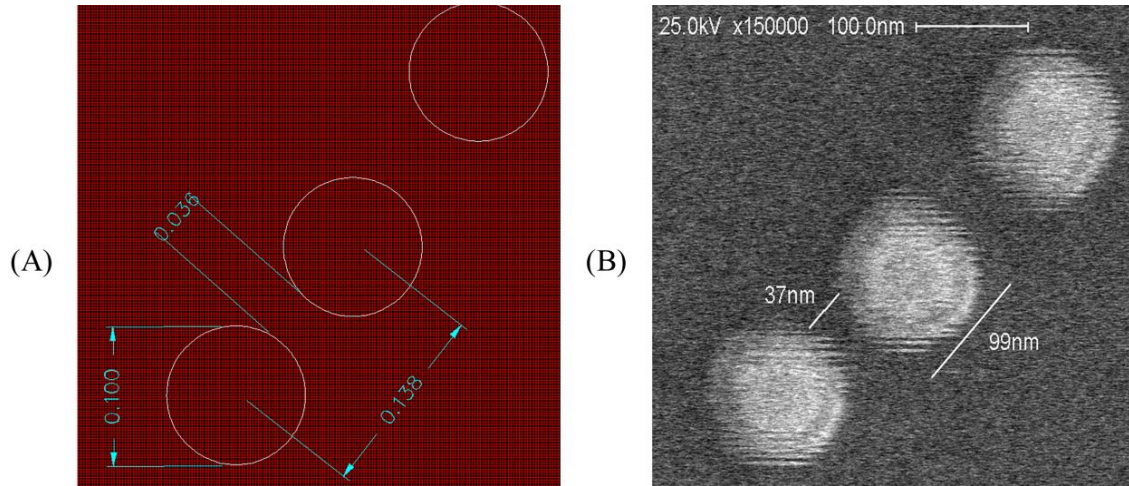
Figure 7-3 (A) is a CAD design of nano-disk in microns. Critical dimensions are given as 36nm in between 100nm disks. (B) depicts the corresponding fabricated pattern.

The MFC systems were designed using DesignCAD2000 NT. The most effective line spacing, exposure doses, points, and focus were determined by using diagnostic wheel pattern. A sample of the Si coated with 950K molecular weight PMMA was then loaded into the JEOL 840m retrofitted with the NPGS lithography system and a beam blanker. The SEM was then focused and the stigmation was adjusted for optimal results. The pattern was selected and written via the NPGS system. Afterwards, the sample was unloaded and was ready to be developed. For this particular process the developer, MIBK: Isopropanol 1:3.

Permalloy was then deposited, via the Varian Model 980-2462 Electron Beam Evaporator. A vacuum of about 2 μTorr was achieved and evaporation was conducted at a 2 Å sec^{-1}. Once the desired thickness of the material was deposited; the liftoff step was next. The sample coated with Permalloy was placed in a heated ultrasonic acetone bath for approximately 15 minutes.

Figure 7-4 (A) shows the phase graph and magnetic image of a single domain magnet taken via a MFM. (B) is the same for the vortex state which is identified by the eye in the center of the magnet. Notice that the repulsive force at the eye of the vortex was much weaker than the attractive force experienced around the eye. In fact the force experienced at the eye was on the same order of magnitude as the background noise.
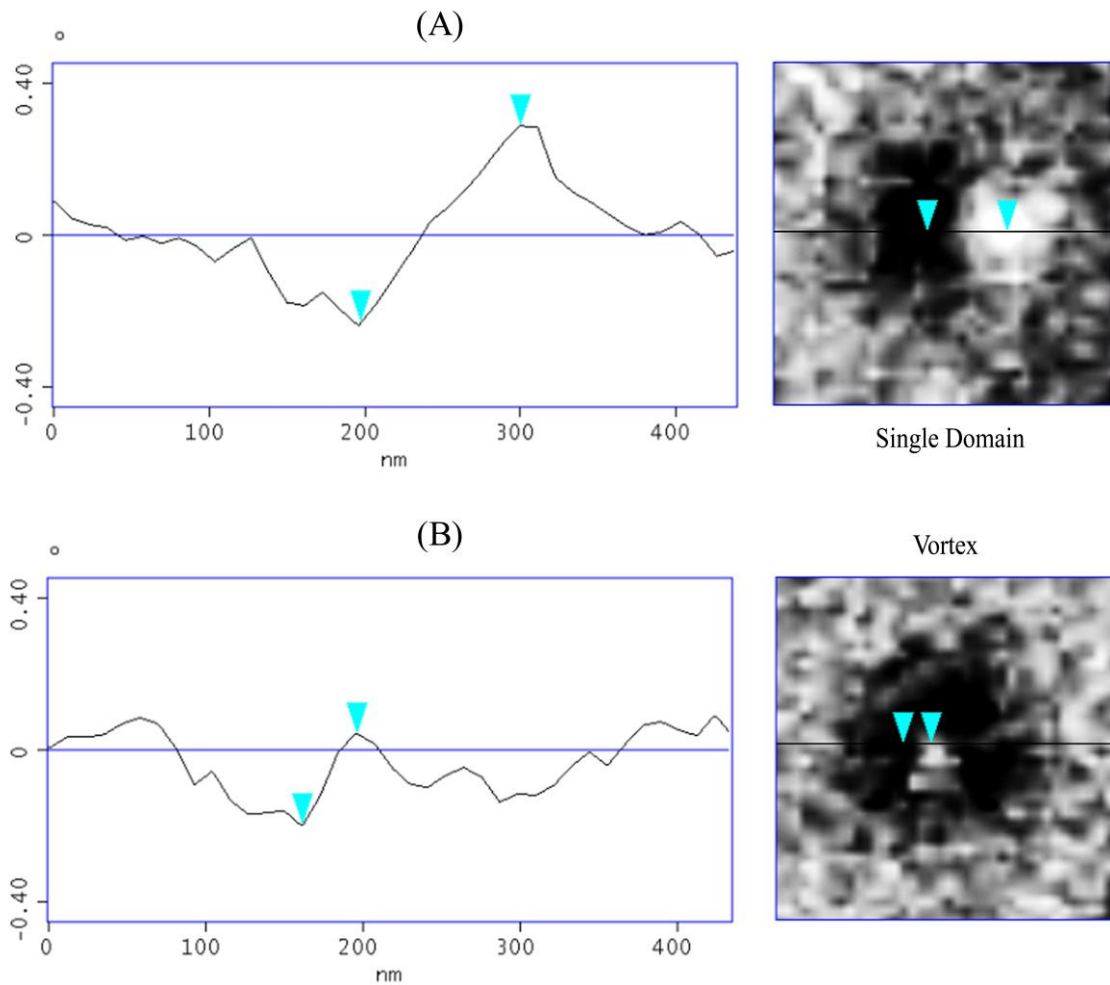
7.4 Results

As mentioned above, the size, spacing, and placement all correlated to features of an image; therefore proper fabrication of a design was imperative. Figure 7-3 (A) and (B) is a CAD design and SEM image, respectively. The purpose of this figure is to demonstrate the degree of accuracy in which the desired layout was fabricated. On a larger scale though, there were instances where some common irregularities associated

85

with the electron beam fabrication process occurred. It was important to explore how all these parameters affect the ability of a MFC system to couple and therefore extract salient features. In this section the possible states of a nano-magnet in the system were discussed and how physical dimensions of a nano-magnetic affected the overall coupling.

The magnetic nano-disks used throughout the experiments were made of permalloy which had uniaxial magnetocrystalline anisotropy. The circular shape combined with the magnetocrystalline anisotropy allowed for a nano-disk to have an easy axis of magnetization of 360 degrees. For the proof of concept, the thickness was reduced to try to induce an in-plane single domain magnetic moment. The in-plane moments would couple with neighbors through magneto-static interactions. Figure 7-4 are MFM phase graphs with the corresponding image of the possible states. There was an interesting dynamic between the formation of a vortex or single domain moment in nano-disks which was a formulation of material, diameter, and thickness. Indeed, a complete implementation of magnetic field computation could benefit from the ability to switch between single domain and vortex states, particularly because the vortex state had no stray field. This would essentially remove any participation of a nano-disk (in the vortex state) from the computational process. For the purpose of these experiments the goal was to create in-plane dipole interactions through single domain magnetic moments.

A simple MFC system was chosen for the first experiment and shown in Figure 7-5. The permalloy nano-disks had a thickness of approximately 32.527 nm and a diameter of a 156.56 nm. The purpose of this experiment was to see if the three leftmost magnets would exhibit strong coupling, while the two rightmost magnets exhibit a

86
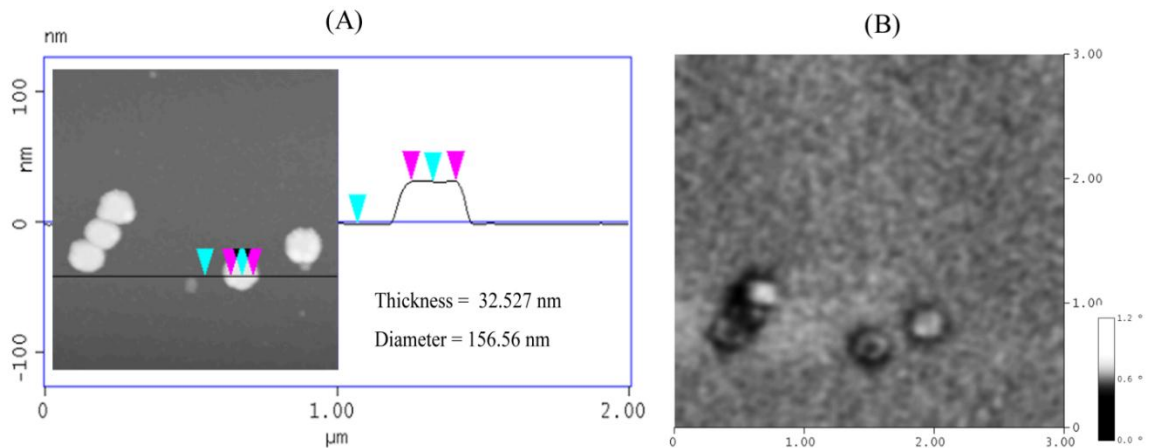
Figure 7-5 (A) is an AFM height amplitude image and corresponding graph. (B) is the MFM image of the first simple MFC system. It was difficult to interpret if any coupling had taken place.

weaker coupling. The stronger coupling would be due to the closer spacing and Figure 7-5 (B) shows the magnetic image of the system. In the MFM image certain magnets were in a vortex state while others were not. It was clear that the desire coupling between the leftmost magnets was not evident. The magnets were expected to be in a similarly oriented single domain magnet moment, which demonstrated the coupling between the states. The fact that there were vortex states in the system, in this situation, was undesired, and was most likely due to the thickness to radius ratio. Although there has been research in the formation of vortex and single domain moments, most of this work was studying the nano-disk as decoupled entities. Indeed most work had spaced the nano-disk far enough apart such that magneto-static interaction from neighbors can be neglected. The interest of the MFC systems presented in this study was to have nano-disk couple though single domain magneto-static interactions. Investigating how the potential energy of a neighboring magnet affected the state of a nano-disk and the formation of vortices was necessary.

87
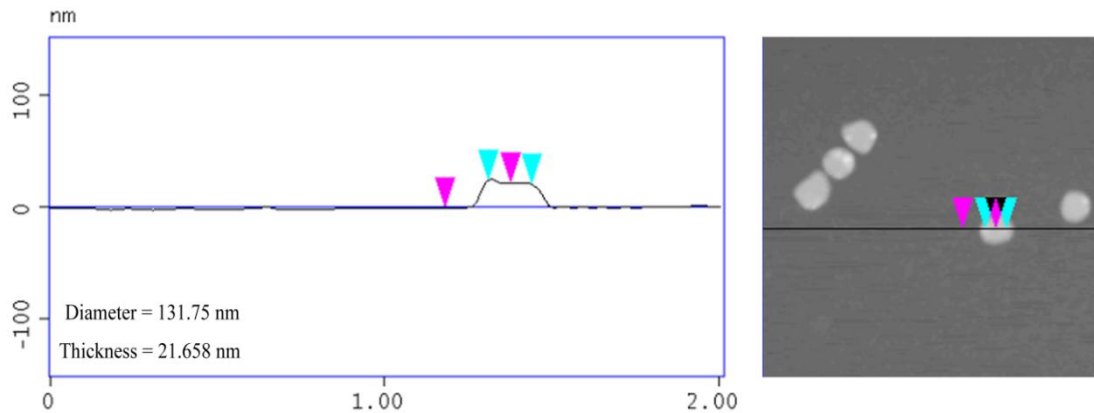
Figure 7-6 is an AFM height amplitude image and corresponding graph of the second simple MFC system. As can be seen in the graph the diameter of the measured nano-disk is 131.75 nm and the thickness is 21.658 nm. This was a 15.8% reduction in diameter and 33.4% reduction of thickness when compared to the first system.

When considering the fabrication layout and dimensions of the next system, the size of the nano-disk was reduced to remove the possible formation of a vortex state. Also, an elongated structure was introduced (magnet 1) to be used as a driver of the coupled magnets (magnets 2 and 3). The shape anisotropy energy of the elongated magnet forces a magnetization direction along the long axis, and therefore if neighboring magnets were coupled they should respond to the driver cell. Figure 7-6 shows a force plot of the AFM amplitude image to the right. The average dimensions of the nano-disks were approximately 130 nm in diameter and 20 nm thick. The reduction of dimensions should reduce or eliminate vortex states in the system and force all the magnetic moments to be single domain. As expected, all the nano-disks were in single domain configurations, with the magnets 1-3 exhibiting strong coupling.

Figure 7-7 are MFM images of the second MFC system scanned in various directions sequentially. Figure 7-7 (A) is a typical MFM scan of the system with the slow scan direction from bottom to top, and the fast scan direction from left to right as depicted by

88
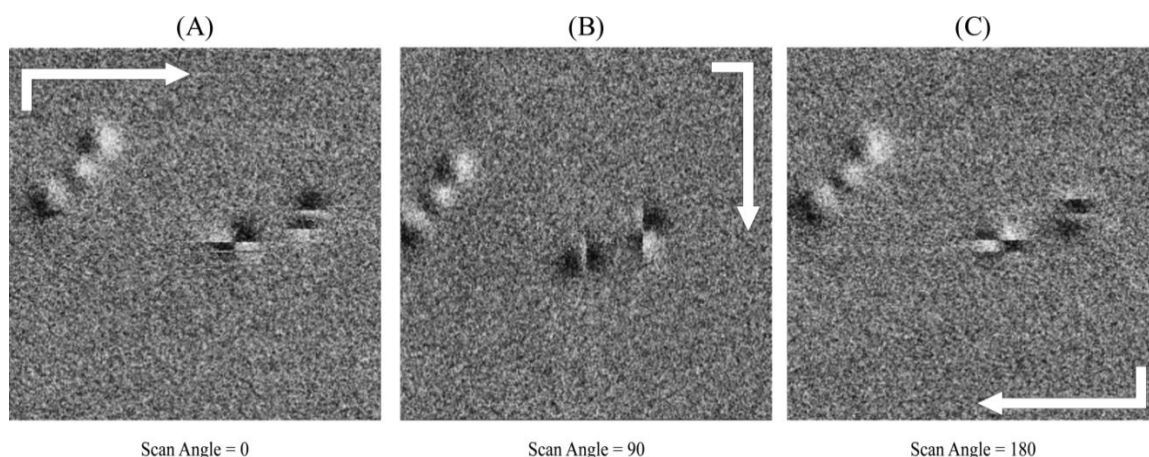
Figure 7-7 (A) is a MFM scan of the second MFC system at a 0 degree scan angle. The images have been rotated to ease interpretation and the arrows represent the scan paths. The slow scan direction was at the tail end and the fast scan direction is depicted by the head of the arrow. The magnets are referred to as magnets 1-5 from left to right. (B) is the same system scanned at 90 degrees. Notice the magnets 1-3 retained their magnetization from (A) while magnets 4 and 5 were altered by the scan. (C) is a scan at 180 degrees. Magnets 1-3 retained their magnetization due to the ferromagnetic coupling between each other.

the arrow. As desired, the three leftmost magnets seemed to be in a single domain state. Moreover, the general angle of the magnetization for magnets 1-3 was in the same direction. This demonstrated ferromagnetic coupling order and therefore magnets 1-3 were considered to be strongly coupled. If a magnetic analysis of the state of the entire system were made, these three magnets would be considered strongly coupled along axis M of Figure 7-2 (C). The high degree of magnetization along the M axis represents a salient relationship. To ensure that the magnetization was not due to the scanning of the MFM tip, meaning that the tip was not significantly altering the state of coupling between neighbors along the scan direction, Figure 7-7 (B) and (C) are images with the scan direction at 90 degrees and 180 degrees, respectively. From these sets of images it was clear that the set of three magnets were strongly coupled and were not

89

Figure 7-8 is a AFM amplitude image of magnet 4 of the second MFC system (right). As can be seen in the graph, the magnet is in fact elliptical. This creates an easy axis of magnetization in the horizontal direction which is along the blue line.

being aligned by the scanning of the tip. This demonstrated the ability of nano-disks to establish single domain moments, and couple based on placement.

When analyzing the two right most magnets (magnets 4 and 5), which should be in a decoupled single domain state due to the distance in between their nearest neighbors, some abnormal magnetic states are depicted in Figure 7-7. Magnet 4 of the two decoupled nano-disks in Figure 7-7 (A) exhibited a pinwheel type magnetization. At first glance it did not appear to be either of the possible magnetic configurations discussed earlier in the chapter, namely single domain or a vortex. This was due to sample tip interaction which caused the nano-disk to flip its magnetization during data acquisition. Even though the tip altered the magnetic state of the nano-disk, the single domain moment could still be extrapolated via the presence of the strong dipoles. By retracing the scanning process of the tip, as represented by the arrow, the single domain moment could be followed as it flips throughout the scan from bottom to top. The stray field from the scanning tip was sufficiently strong to flip the magnetization of the magnet
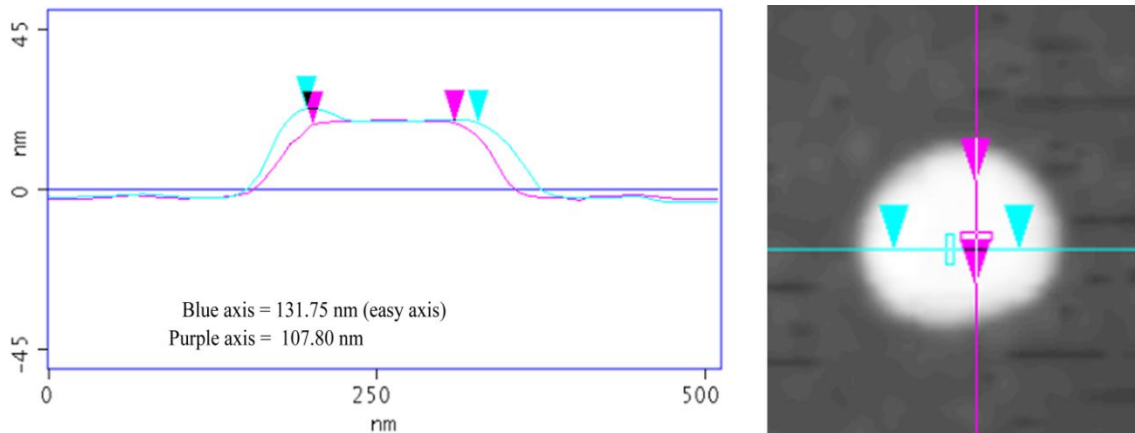
90
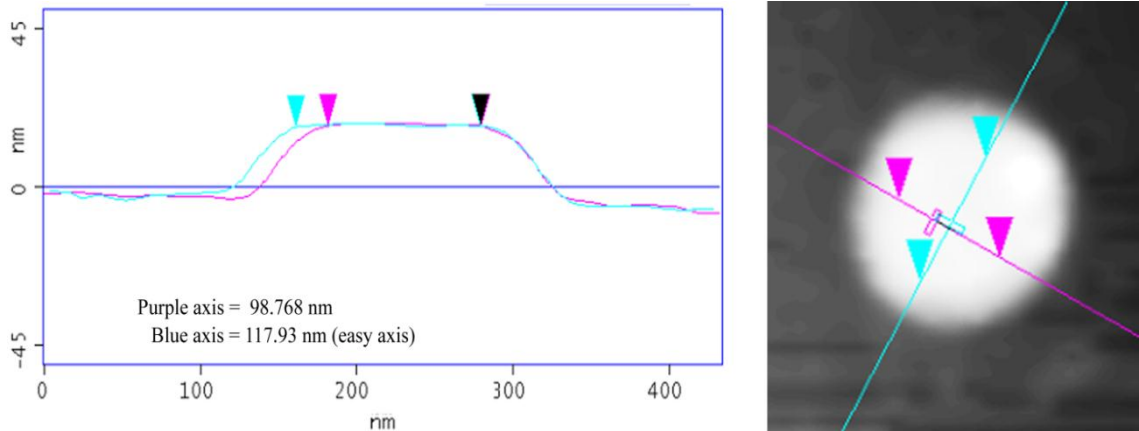
Figure 7-9 is a AFM amplitude image of magnet 5 of the second MFC system (right). As can be seen in the graph the magnet is in fact elliptical. This created an easy axis of magnetization in a vertical direction which is along the blue line.

approximately 3-4 times during the scan. Even though the magnet was in a single domain configuration, because it was decoupled from neighboring elements, the magnetic stray field from the tip was sufficiently strong to alter the state of the nano-disk.

When the leftmost nano-disk was examined (magnet 5) it appeared as if there were two smaller magnets inside of the nano-disk aligned from bottom to top in Figure 7-7 (A). Again, the interpretation of this magnet was not obvious. Figure 7-7 (B) can help deduce what type of magnetic state that magnet 5 was in. By following the scan direction in Figure 7-7 (B) a single domain state could be resolved by using similar logic mentioned in the paragraph above for magnet 4. Although this did explain the situation in Figure 7-7 (B), it did not explain the magnetic state depicted in Figure 7-7 (A) or (C) for the same magnet. It also did not explain the magnetic configuration shown in Figure 7-7 (B) for magnet 4. In order to interpret the magnetization in the aforementioned example, the shape of the magnets must be accounted for as well as the scan direction. Figure 7-8 and Figure 7-9 are AFM amplitude scans of magnets 4 and 5, respectively. In

91

those images the purple line represented the shorter axis and the light blue line was drawn across the longer axis. After closer inspection, the shape was found to be more elliptical than circular. Figure 7-8 shows magnet 4 having a longer horizontal axis by approximately 24 nm, while Figure 7-9 shows magnet 5 to have a longer vertical axis by 19 nm. The elliptical shape created an easy axis of magnetization along the longer axis due to shape anisotropy. When the tip was scanned horizontally along magnet 4 in Figure 7-7 (A) and (C), the single domain moment could be seen before flipping but when scanned along the vertical hard axis, as in Figure 7-7 (B), only one scan of the brighter pole was seen before the magnetization flips. The tip was scanned over one pole several times (the left half of the magnet) and showed the darker profile. Once it reached the opposite pole (the brighter right side) the tip-sample interaction forced the like poles of the tip and nano-disk to flip the magnetization, which made the right half of the disk represent the attractive force (darker) as well. A similar explanation can be used for the magnetization of magnet 5 in Figure 7-7. The reason that more of the repulsive force (bright pole) could be extracted for magnet 5 in Figure 7-7 (A) than magnet 4 in Figure 7-7 (B) can be explained by the smaller difference between the easy and hard axis. The shape of magnet 5 was closer to a circle than magnet 4 by 5 nm. This reduced the shape anisotropy energy which allowed for more of the moment to align in the harder axis before completely flipping the magnetization. With this understanding of the shape anisotropy and scan directions, it was determined that the decoupled magnets were also single domain in nature.

When interpreting the results from the second MFC system some conclusions were drawn. The smaller dimension and ratio of diameter to thickness had created the desired single domain magnetizations. The magnets that were more closely spaced displayed

ferromagnetic coupling, while the magnets that were further apart were more strongly influenced by sample-tip field interactions. The distinction of flipping or not flipping the magnets via tip scanning was in fact a satisfying way to qualify whether or not magnets were strongly coupled, and therefore whether the magnets represented a salient relationship. The successful implementation and new understanding of the coupling and scanning dynamics encouraged the fabrication of a larger more complex system.

A third MFC system was implemented and the layout is given in Figure 7-10 (B). The feature sizes of the system were altered, as shown in Figure 7-10 (A), to investigate changes in the magnetization of the nano-disk. It was evident by the layout that this system was much more complex and more neighbor-neighbor interaction would take place. Figure 7-10 (C) is the corresponding magnetic image of the system where the outlines of the nano-disks have been overlaid in white. During the evaluation of the system, it was evident that as the thickness of the system was reduced it became much more susceptible to the stray field of the tip. This interaction made it more difficult to interpret results. Some important features to point out were that many of the horizontally coupled magnets displayed a ferromagnetic ordering. It also appeared that a row of ferromagnetic coupled nano-disks were coupled to a neighboring row through an anti-ferromagnetic arrangement. There were also several instances of vortex states throughout the system as well as many magnets displaying very weak magnetizations. The current hypothesis is that these weaker magnetizations are in anti-vortex configurations.

Another instance of the pattern was fabricated and shown in Figure 7-11. The graph in Figure 7-11 (A) shows a difference of 32 nm in diameter between the third and fourth system. Interestingly, the sample appeared to be more heavily influenced by the tips

stray field which was demonstrated by the flipping of the nano-disk. Also when comparing the magnetic data from this system to the previous one, more magnets were in a single domain configuration. There were also more magnetic moments that were not resolvable in the previous system with the larger nano-disk. Currently, steps to reduce the tip-sample interaction are being taken, such as exploring alternative magnetic microscopy methods and fabricating custom magnetic tips to reduce the sample tip interaction.

7.5 Conclusion

Magnetic Field-based Computing (MFC) has the potential to provide solutions towards the grouping of low-level segments into relevant features of an image in a unique manner. A proof of concept consisting of 5 nano-magnetic disks that related to low-level edge segments of an image has been provided. The proof of concept was fabricated and strictly adhered to a placement algorithm that correlated magneto-static interactions to the edge affinity energies of an image. The significance of creating nano-disk to specific dimensions was displayed by the undesired formation of preferred axes of magnetization and the formation of magnetic vortices. The strong magneto-static interaction revealed by nano-disks 1-3 was established via the ferromagnetic coupling exhibited by the nano-magnets. Nano-disks 4-5 were strongly influenced by the MFM tip and caused the magnet moments of the magnets to flip during data acquisition. The switching of nano-disk 4-5, and the lack of variation in magnetic dipole moments of nano-disk 1-3 due to the magneto-static coupling, was determined to be a satisfying way of qualifying strong field interactions of magnets. The strong coupling resolved the edges that mapped to nano-disk 1-3 as significant, and could be grouped into a salient feature of an image. The time necessary for the magnetic systems to settle into an

94

energy minimum was the computational time necessary to accomplish the grouping of low-level segments. Two larger systems have also been fabricated and are currently being evaluated to investigate the effectiveness of MFC for perceptual organization in computer vision.

(A)

(B)
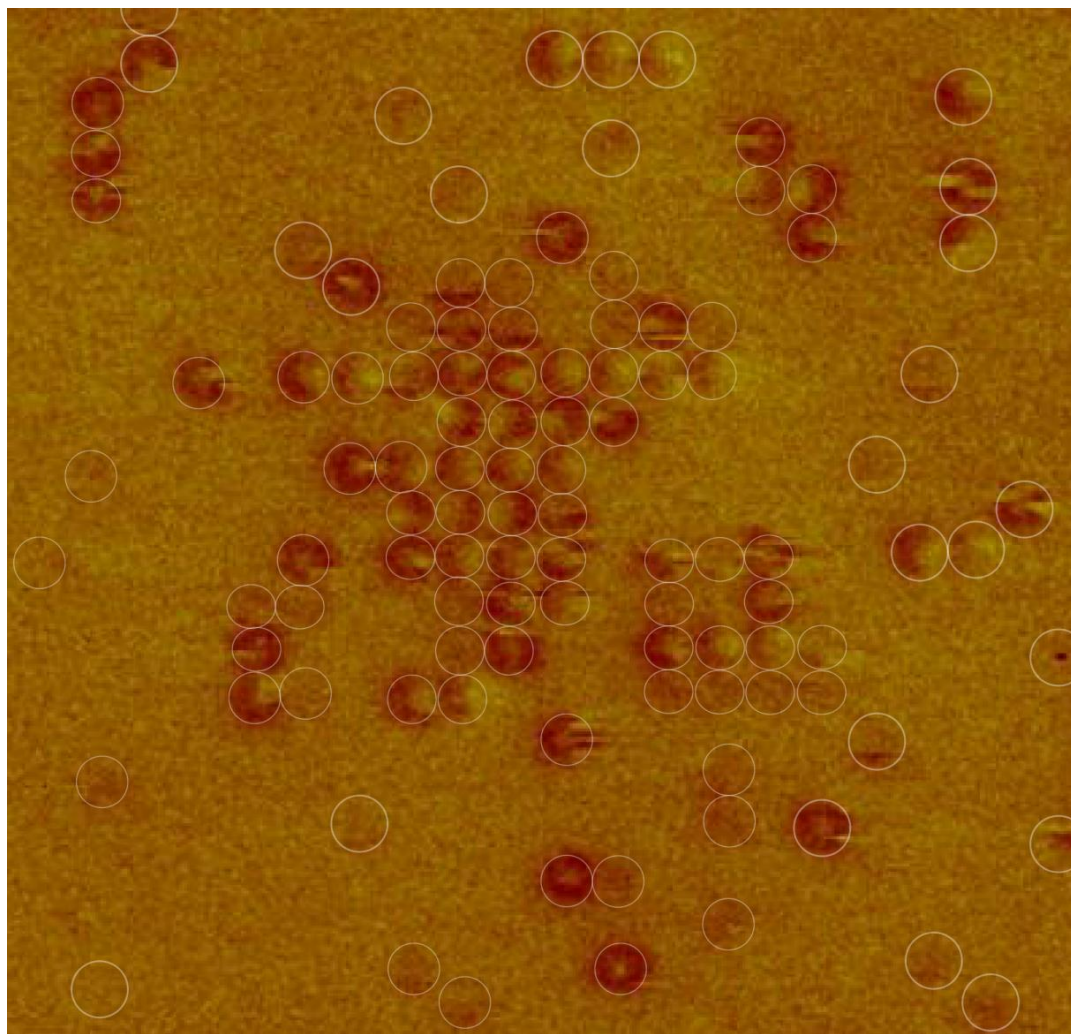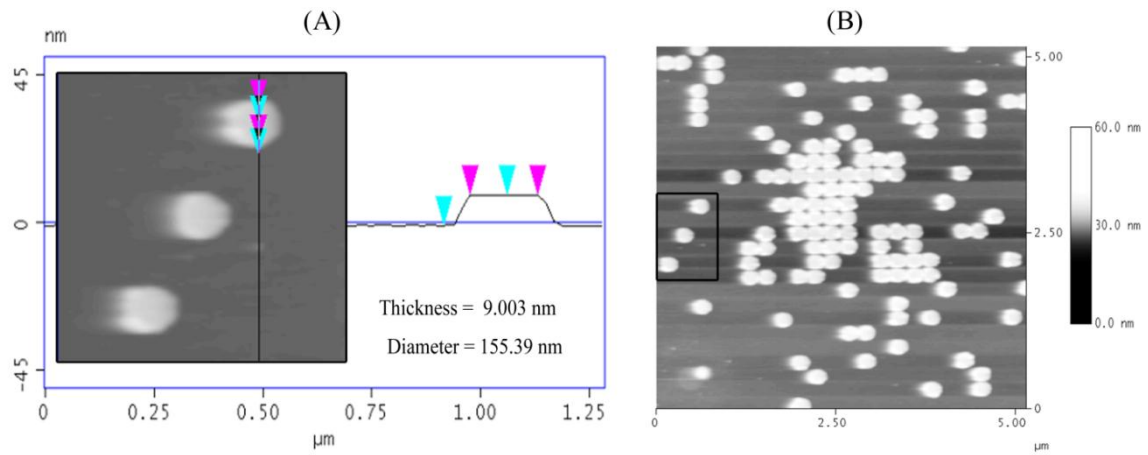
(C)

Figure 7-10 (A) is a AFM height amplitude force plot of MFC system 3. (B) shows the entire arrangement of nano-disk. (C) is the MFM data gathered from the system. White circles were overlaid on the image to relate the physical placement of the nano-disk.
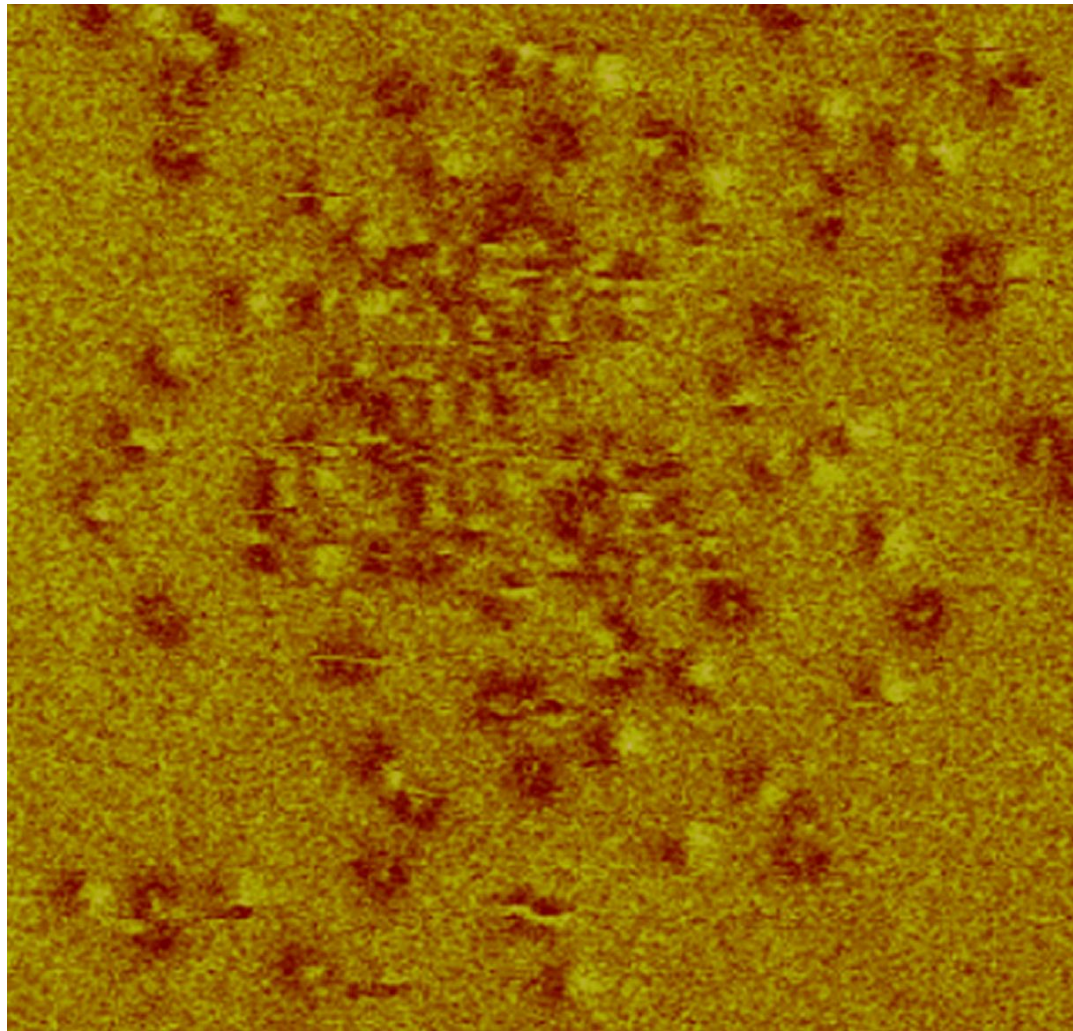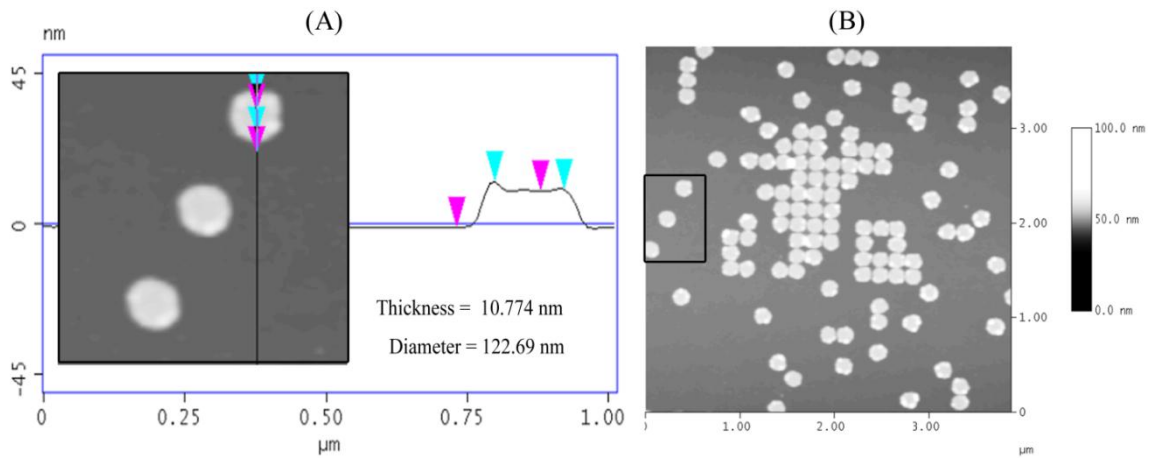
Figure 7-11 (A) is a AFM height amplitude force plot of MFC system 4. (B) shows the entire arrangement of nano-disk. (C) is the MFM data gathered from the system.

Chapter 8

Conclusion

8.1   Synopsis

The use of nano-magnetic switches for computation is a novel application that offers several potential benefits, such as a high density of switches, ultra-low power devices, integration with MRAM, non-volatile operation, and radiation hardness. Corroborative data has been presented regarding the reliability of magnetic coupling through field interactions, and it has been found that nano-magnetic cells were robust to common fabrication defects associated to the electron beam lithography process. The data experimentally verified the functionality of a previously reported Magnetic Cellular Automata (MCA) majority gate, and a larger majority gate system was shown to be operational. Furthermore, a new ferromagnetic coupled majority gate based on the experience of ferromagnetic architectures being less prone to magnetic frustrations was introduced. A working ferromagnetic majority gate was demonstrated and a logic network of two ferromagnetic majority gates feeding into another ferromagnetic majority gate was also presented. Though the results have shown that the ferromagnetic majority gate network always had one magnetic frustration, this could be attributed to the absence of computational synchronization for Magnetic Cellular Automata.

The first comparative study of ferromagnetic and anti-ferromagnetic MCA wire architectures under external clocking fields was also introduced. Four different external

98

magnetic fields to magnetize the system were provided: an in-plane easy axis, an in-plane hard axis, an out-of-plane hard axis, and a spinning field to both a ferromagnetic and anti-ferromagnetic wire with magnetic cells of approximately 100 (l) x 50 (w) x 30 (th) nm^3. The external magnetic energy was removed and the wires were allowed to settle into local magnetic energy minimums and analyzed for magnetic frustrations. The experimental results showed ferromagnetic wires were less susceptible to magnetic frustrations than anti-ferromagnetic wires by up to 67% when magnetized along the in-plane easy axis. The energy associated with two magnetic cells arranged in an anti-ferromagnetic and ferromagnetic coupling scenario was simulated and the high energy meta-stable state (magnetic frustration) and the low energy ground state were compared. The kink energy, which is the energy difference between the meta-stable state and the ground state, was 4,856.35 J/m^3 larger for ferromagnetic wire than the anti-ferromagnetic wire architecture. The improved mitigation of ferromagnetic wires over anti-ferromagnetic wires could be attributed to the larger energy gap between the meta-stable state and ground state of ferromagnetic wires. From these results it was concluded that ferromagnetic wires will likely be the main interconnect for MCA. It was determined that providing an out-of-plane clocking field could eliminate complexities that could arise from having both horizontal and vertical in-plane magnetic interactions for computation. The out-of-plane clocking field could allow for magnetic clocking domains to be established and be insensitive to the in-plane orientation of data propagation in a MCA circuit.

The capacity of having wires cross on the same device plane had been a theorized feature of Quantum Cellular Automata (QCA) yet to be physically realized. The first design and implementation of a Magnetic Cellular Automata coplanar crosswire system

99

was presented here. The system was designed to use the ferromagnetic wire architecture and intersect two wires at a 90 degree angle. The rectangular shape of the magnetic cells created an easy and hard axis of magnetization and the 90 degree angle utilized the in-plane hard magnetization axis to abate any cross talk interference between intersecting wires. Simulations were implemented to verify functionality and analyze coupling dynamics. The coplanar crossing wires were then fabricated in two systems; a simple two crosswire system with a total of 20 magnetic cells and a larger complex system consisting of 6 ferromagnetic coupled wires with 120 nano-magnetic cells. The four possible logic combinations of the smaller system were demonstrated via Magnetic Force Microscopy and results were shown from the larger complex system. The ability for the complex system to settle into a nominal ground state energy, and the validation of all the possible logic combinations of the smaller system, established the feasibility of coplanar crossing wires in Magnetic Cellular Automata.

A novel unconventional mapping of a vision algorithm to the energy minimization of magnetic dipolar interaction was also presented. Magnetic Field-Based Computing (MFC) using circular magnetic nano-disks, were used and correlated to edges of a low level segmented image. The purpose was to use the magnetic nano-disk to solve the quadratic problem of grouping edge segments together. Computing edge affinity through accepted Boolean methods is computationally intensive and is often the bottle neck in the perceptual organization of image processing in the area of computer vision. By placing nano-disks at specific locations, the quadratic edge affinity term of the edge grouping equation, was effectively mapped to the quadratic distance term of magneto-static interactions for nano-disks. The solution of grouping salient edges together was accomplished in the time it takes for the magnetic system to settle into a ground state.

100

A simple 5 nano-disk system was fabricated, and explored how factors such as disk thickness affected the formation of single domain and vortex states. Examples were provided demonstrating that a minimal value of 19 nanometers caused an elliptical shaped nano-disk and formed an easy and hard axis of magnetization due to shape anisotropy energy, which altered the behavior of the MFC system. The correlation of the magnetization vector along a particular axis to the significance of an edge was established and proven to be feasible. The experimental results of larger more complex systems were also presented and are currently in the process of being analyzed.

8.2   Future Endeavors

The synchronization of a larger Magnetic Cellular Automata (MCA) system via a clocking structure has yet to be realized. This essential feature of MCA is an ongoing area of investigation and we are exploring the use of nanowires and multiple metallization planes to create clocking domains. This will allow for the control of data flow from input to output and move the technology closer to a functioning logic device.

Also, the ability to provide inputs in an efficient manner is of pronounced importance. Currently MRAM has employed different methods of writing to a magnetic storage cell. We are presently exploring MRAM writing methods, such as spin torque transfer, as a means of providing inputs to magnetic cells in MCA.

In addition, we are also exploring alternative magnetic microscopy methods to reduce the interaction between the measuring apparatus and the sample, such as Lorentz Microscopy, Electron Holography, and X-ray Magnetometry. Magnetic Force Microscopy can have strong sample-tip interactions with a magnetically soft sample and can alter the state of the nano-magnet, such as described when imaging the Magnetic Field-based Computing systems in Chapter 7. The alternative microscopy methods

101

mentioned above could potentially provide quantitative analysis and yield real time dynamics of a system.

List of References

1. Imre, A., et al., *Majority logic gate for magnetic quantum-dot cellular automata.* Science, 2006. 311(5758): p. 205-208.

2. Moore, G.E., *Cramming More Components Onto Integrated Circuits.* Proceedings of the IEEE, 1998. 86(1): p. 82-85.

3. Kanellos, M. (2005) *New life for Moore's Law.* CNET news.

4. Hei, K., et al. *A new nano-electro-mechanical field effect transistor (NEMFET) design for low-power electronics.* in *Electron Devices Meeting, 2005. IEDM Technical Digest. IEEE International.* 2005.

5. Jang, W.W., et al., *NEMS switch with 30 nm-thick beam and 20 nm-thick air-gap for high density non-volatile memory applications.* Solid-State Electronics, 2008. 52(10): p. 1578-1583.

6. Pruvost, B., H. Mizuta, and S. Oda, *3-D Design and Analysis of Functional NEMS-gate MOSFETs and SETs.* Nanotechnology, IEEE Transactions on, 2007. 6(2): p. 218-224.

7. Appenzeller, J., et al., *Band-to-Band Tunneling in Carbon Nanotube Field-Effect Transistors.* Physical Review Letters, 2004. 93(19): p. 196805.

8. Guangyu, Z., et al. *Carbon Nanotubes: From Growth, Placement and Assembly Control to 60mV/decade and Sub-60 mV/decade Tunnel Transistors.* in *Electron Devices Meeting, 2006. IEDM '06. International.* 2006.

9. Knoch, J. and J. Appenzeller, *Tunneling phenomena in carbon nanotube field-effect transistors.* physica status solidi (a), 2008. 205(4): p. 679-694.

10. Li, H., et al., *Microstructure of cement mortar with nano-particles.* Composites Part B: Engineering, 2004. 35(2): p. 185-189.

11. Ito, A., et al., *Medical application of functionalized magnetic nanoparticles.* Journal of Bioscience and Bioengineering, 2005. 100(1): p. 1-11.

12. Semiconductors, I.T.R.f. (2009) *Emerging Research Devices.*

13. Csaba, G., W. Porod, and A.I. Csurgay, *A computing architecture composed of field-coupled single domain nanomagnets clocked by magnetic field.* International Journal of Circuit Theory and Applications, 2003. 31(1): p. 67-82.

103

14.   Imre, A., et al., *Majority Logic Gate for Magnetic.* Science, 2006. 311: p. 205-208.

15.   Gardner, M., *The fantastic combinations of John Conway's new solitaire game "life".* Scientific American, 1970. 223: p. 120-123.

16.   Conway, J.H., *The game of life.* Scientific American, 1970.

17.   Lent, C.S. and P.D. Tougaw, *Device architecture for computing with quantum dots.* Proceedings of the Ieee, 1997. 85(4): p. 541-557.

18.   Tougaw, P.D. and C.S. Lent, *Effect of Stray Charge on Quantum Cellular-Automata.* Japanese Journal of Applied Physics Part 1-Regular Papers Short Notes & Review Papers, 1995. 34(8B): p. 4373-4375.

19.   Tougaw, P.D. and C.S. Lent, *Quantum Cellular-Automata - Computing with Quantum-Dot Molecules.* Compound Semiconductors 1994, 1995(141): p. 781-786.

20.   Bernstein, G.H., et al., *Practical issues in the realization of quantum-dot cellular automata.* Superlattices and Microstructures, 1996. 20(4): p. 447-459.

21.   Gin, A., et al., *Hierarchical of design of quantum-dot cellular automata devices.* Journal of Applied Physics, 1999. 85(7): p. 3713-3720.

22.   Csaba, G., A. Csurgay, and W. Porod, *Computing architecture composed of next-neighbour-coupled optically pumped nanodevices.* International Journal of Circuit Theory and Applications, 2001. 29(1): p. 73-91.

23.   Imre, A., et al., *Investigation of shape-dependent switching of coupled nanomagnets.* Superlattices and Microstructures, 2003. 34(3-6): p. 513-518.

24.   Bernstein, G.H., et al., *Magnetic QCA systems.* Microelectronics Journal, 2005. 36(7): p. 619-624.

25.   Orlov, A., et al., *Magnetic Quantum-dot Cellular Automata: Recent developments and prospects.* Journal of Nanoelectronics and Optoelectronics, 2008. 3(1): p. 55-68.

26.   Hennessy, K. and C.S. Lent, *Clocking of molecular quantum-dot cellular automata.* Journal of Vacuum Science & Technology B: Microelectronics and Nanometer Structures, 2001. 19(5): p. 1752-1755.

27.   Momenzadeh, M., M. Ottavi, and F. Lombardi. *Modeling QCA defects at molecular-level in combinational circuits*. in *Defect and Fault Tolerance in VLSI Systems, 2005. DFT 2005. 20th IEEE International Symposium on*. 2005.

28.   Walus, K. and G.A. Jullien, *Design tools for an emergng SoC technology: Quantum-dot cellular automata.* Proceedings of the Ieee, 2006. 94(6): p. 1225-1244.

104

29.   Alam, M.T., et al. *On-Chip Clocking Scheme for Nanomagnet QCA*. in *Device Research Conference, 2007 65th Annual*. 2007.

30.   Alam, M.T., et al. *Clocking scheme for nanomagnet QCA*. in *Nanotechnology, 2007. IEEE-NANO 2007. 7th IEEE Conference on*. 2007.

31.   Karim, F., et al., *Modeling and Evaluating Errors Due to Random Clock Shifts in Quantum-Dot Cellular Automata Circuits.* Journal of Electronic Testing-Theory and Applications, 2009. 25(1): p. 55-66.

32.   Parish, M.C.B. and M. Forshaw, *Physical constraints on magnetic quantum cellular automata.* Applied Physics Letters, 2003. 83(10): p. 2046-2048.

33.   Parish, M.C.B. and M. Forshaw, *Magnetic cellular automata (MCA) systems.* Circuits, Devices and Systems, IEE Proceedings -, 2004. 151(5): p. 480-485.

34.   Bhanja, S. and N. Ranganathan. *Modeling switching activity using cascaded Bayesian networks for correlated input streams*. in *Computer Design: VLSI in Computers and Processors, 2002. Proceedings. 2002 IEEE International Conference on*. 2002.

35.   Bhanja, S. and S. Sarkar. *Switching Error Modes of QCA Circuits*. in *Nanotechnology, 2006. IEEE-NANO 2006. Sixth IEEE Conference on*. 2006.

36.   Bhanja, S. and S. Sarkar, *Probabilistic Modeling of QCA Circuits Using Bayesian Networks*, in *Nanotechnology, IEEE Transactions on*. 2006. p. 657-670.

37.   Saket, S. and B. Sanjukta, *Hierarchical Probabilistic Macromodeling for QCA Circuits*, in *Computers, IEEE Transactions on*. 2007. p. 174-190.

38.   Bhanja, S., et al., *QCA Circuits for Robust Coplanar Crossing.* Journal of Electronic Testing, 2007. 23(2): p. 193-210.

39.   Bhanja, S. and S. Sarkar, *Thermal Switching Error Versus Delay Tradeoffs in Clocked QCA Circuits.* Very Large Scale Integration (VLSI) Systems, IEEE Transactions on, 2008. 16(5): p. 528-541.

40.   Sarkar, S. and S. Bhanja. *Direct Quadratic Minimization Using Magnetic Field-Based Computing*. in *Design and Test of Nano Devices, Circuits and Systems, 2008 IEEE International Workshop on*. 2008.

41.   Srivastava, S., S. Sarkar, and S. Bhanja. *Error-Power Tradeoffs in QCA Design*. in *Nanotechnology, 2008. NANO '08. 8th IEEE Conference on*. 2008.

42.   Srivastava, S., S. Sarkar, and S. Bhanja, *Estimation of Upper Bound of Power Dissipation in QCA Circuits.* Nanotechnology, IEEE Transactions on, 2009. 8(1): p. 116-127.

43.   Cowburn, R.P. and M.E. Welland, *Room Temperature Magnetic Quantum Cellular Automata.* Science, 2000. 287: p. 1466-1468.

105

44.   Csaba, G., et al., *Nanocomputing by field-coupled nanomagnets.* Ieee Transactions on Nanotechnology, 2002. 1(4): p. 209-213.

45.   Cowburn, R.P., A.O. Adeyeye, and M.E. Welland, *Configurational anisotropy in nanomagnets.* Physical Review Letters, 1998. 81(24): p. 5414-5417.

46.   Cowburn, R.P. and M.E. Welland, *Micromagnetics of the single-domain state of square ferromagnetic nanostructures.* Physical Review B, 1998. 58(14): p. 9217-9226.

47.   Cowburn, R.P., et al., *Designing nanostructured magnetic materials by symmetry.* Europhysics Letters, 1999. 48(2): p. 221-227.

48.   Cowburn, R.P. and M.E. Welland, *Analytical micromagnetics of near single domain particles.* Journal of Applied Physics, 1999. 86(2): p. 1035-1040.

49.   Cowburn, R.P., et al., *Single-Domain Circular Nanomagnets.* The American Physical Society, 1999. 83(5): p. 1042-1045.

50.   Cowburn, R.P., et al., *Sensing magnetic fields using superparamagnetic nanomagnets.* Journal of Applied Physics, 2000. 87(9): p. 7082-7084.

51.   Cowburn, R.P., et al., *Lateral interface anisotropy in nanomagnets.* Journal of Applied Physics, 2000. 87(9): p. 7067-7069.

52.   Cowburn, R.P., *Where Have All the Transistors Gone?* Science, 2006. 311: p. 183-184.

53.   Cowburn, R.P., et al., *Single-domain circular nanomagnets.* Physical Review Letters, 1999. 83(5): p. 1042-1045.

54.   Imre, A., et al., *Controlled domain wall motion in micron-scale permalloy square rings.* Physica E-Low-Dimensional Systems & Nanostructures, 2003. 19(1-2): p. 240-245.

55.   Csaba, G., P. Lugli, and W. Porod. *Power dissipation in nanomagnetic logic devices*. in *Nanotechnology, 2004. 4th IEEE Conference on*. 2004.

56.   Imre, A., et al., *Flux-closure magnetic states in triangular cobalt ring elements.* Ieee Transactions on Magnetics, 2006. 42(11): p. 3641-3644.

57.   Csaba, G., et al., *Activity in field-coupled nanomagnet arrays.* International Journal of Circuit Theory and Applications, 2007. 35(3): p. 281-293.

58.   Becherer, M., et al., *Magnetic ordering of focused-ion-beam structured cobalt-platinum dots for field-coupled computing.* Ieee Transactions on Nanotechnology, 2008. 7(3): p. 316-320.

59.   Tougaw, P.D., C.S. Lent, and W. Porod, *Bistable Saturation in Coupled Quantum-Dot Cells.* Journal of Applied Physics, 1993. 74(5): p. 3558-3566.

60.   Alam, M.T., et al. *Magnetic Logic Based on Coupled Nanomagnets: Clocking Structures and Power Analysis*. in *Nanotechnology, 2008. NANO '08. 8th IEEE Conference on*. 2008.

61.   Niemier, M., et al., *Clocking structures and power analysis for nanomagnet-based logic devices*, in *Proceedings of the 2007 international symposium on Low power electronics and design*. 2007, ACM: Portland, OR, USA. p. 26-31.

62.   Kumari, A. and S. Bhanja, *Landauer Clocking for Magnetic Cellular Automata (MCA) Arrays*. Very Large Scale Integration (VLSI) Systems, IEEE Transactions on, 2010. PP(99): p. 1-4.

63.   Niemier, M., M. Crocker, and X.S. Hu. *Fabrication Variations and Defect Tolerance for Nanomagnet-Based QCA*. in *Defect and Fault Tolerance of VLSI Systems, 2008. DFTVS '08. IEEE International Symposium on*. 2008.

64.   Carlton, D.B., et al., *Simulation Studies of Nanomagnet-Based Logic Architecture*. Nano Letters, 2008. 8(12): p. 4173-4178.

65.   Casta, et al., *Metastable states in magnetic nanorings*. Physical Review B, 2003. 67(18): p. 184425.

66.   Landeros, P., et al., *Stability of magnetic configurations in nanorings*. Journal of Applied Physics, 2006. 100(4): p. 044311-6.

67.   Yang, T., et al., *Magnetic characterization and switching of Co nanorings in current-perpendicular-to-plane configuration*. Applied Physics Letters, 2007. 90(2): p. 022504-3.

68.   Zhu, F.Q., et al., *Magnetic Bistability and Controllable Reversal of Asymmetric Ferromagnetic Nanorings*. Physical Review Letters, 2006. 96(2): p. 027205.

69.   Klaui, M., et al., *Vortex circulation control in mesoscopic ring magnets*. Applied Physics Letters, 2001. 78(21): p. 3268-3270.

70.   Klaui, M., et al., *Domain wall coupling and collective switching in interacting mesoscopic ring magnet arrays*. Applied Physics Letters, 2005. 86(3): p. 032504.

71.   Zhu, X., *Magnetic force microscopy studies of submicron and nanoscale magnet arrays. Ph.D. dissertation*. 2002, McGill University (Canada).

72.   Imre, A., *EXPERIMENTAL STUDY OF NANOMAGNETS FOR MAGNETIC QUANTUMDOT CELLULAR AUTOMATA (MQCA) LOGIC APPLICATIONS*. 2005, University of Notre Dame.

73.   Allwood, D.A., et al., *Magnetic Domain-Wall Logic*. Science, 2005. 309(5741): p. 1688-1692.

74.   Atkinson, D., et al., *Magnetic domain-wall dynamics in a submicrometre ferromagnetic structure*. Nat Mater, 2003. 2(2): p. 85-87.

75.   Faulkner, C.C., et al., *Controlled switching of ferromagnetic wire junctions by domain wall injection.* Magnetics, IEEE Transactions on, 2003. 39(5): p. 2860-2862.

76.   Hayashi, M., et al., *Current-Controlled Magnetic Domain-Wall Nanowire Shift Register.* Science, 2008. 320(5873): p. 209-211.

77.   Xu, P., et al., *An all-metallic logic gate based on current-driven domain wall motion.* Nat Nano, 2008. 3(2): p. 97-100.

78.   Allwood, D.A., et al., *Submicrometer Ferromagnetic NOT Gate and Shift Register.* Science, 2002. 296(5575): p. 2003-2006.

79.   Vernier, N. and et al., *Domain wall propagation in magnetic nanowires by spin-polarized current injection.* EPL (Europhysics Letters), 2004. 65(4): p. 526.

80.   Thiaville, A., et al., *Domain wall motion by spin-polarized current: a micromagnetic study.* Journal of Applied Physics, 2004. 95(11): p. 7049-7051.

81.   Hu, W., et al., *Sub-10 nm electron beam lithography using cold development of poly(methylmethacrylate).* Journal of Vacuum Science & Technology B: Microelectronics and Nanometer Structures, 2004. 22(4): p. 1711-1716.

82.   [cited 2010 11/11]; Nanometer Pattern Generation System, a direct write lithography system for Electron or Ion Beam Microscopes]. Available from: http://www.jcnabity.com/.

83.   Moreau, W.M., *Semiconductor Lithography Principles, Practices, and Materials*. Microdevices Physics and Fabrication Technologies, ed. J.J.M.a.I. Brodie. 1988, New York and London: Plenum Press.

84.   MicroChem *PMMA datasheet*.

85.   Zheng, C., *Micro-Nanofabrication: Technologies and Applications*. 1 ed. 2006: Springer. 300.

86.   Herring, C. and M.H. Nichols, *Thermionic Emission.* Reviews of Modern Physics, 1949. 21(2): p. 185.

87.   Nonogaki, S., *Microlithography Fundementals in Semiconductor Devices and Fabrication Technology*. 1998, New York: Dekker.

88.   Leavitt, J.A., et al., *Permalloy stoichiometry by nuclear backscattering.* Nuclear Instruments and Methods in Physics Research Section B: Beam Interactions with Materials and Atoms, 1985. 10-11(Part 2): p. 719-721.

89.   Jeager, R.C., *Introduction to Microelectronic Fabrication*. Modular Series on Solid State Devices, ed. Second. Vol. V. 2002, Upper Saddle River Prentice Hall.

90.   Kasap, S.O., *Principles of Electronic Materials and Devices*. 2002: McGraw-Hill.

108

91.   Pulecio, J.F. and S. Bhanja. *Reliability of bi-stable single domain nano magnets for Cellular Automata*. in *Nanotechnology, 2007. IEEE-NANO 2007. 7th IEEE Conference on*. 2007.

92.   Gilbert, T.L., *A phenomenological theory of damping in ferromagnetic materials*. Magnetics, IEEE Transactions on, 2004. 40(6): p. 3443-3449.

93.   Amlani, I., et al., *Experimental demonstration of a leadless quantum-dot cellular automata cell.* Applied Physics Letters, 2000. 77(5): p. 738-740.

94.   Tougaw, P.D. and C.S. Lent, *Logical Devices Implemented Using Quantum Cellular-Automata.* Journal of Applied Physics, 1994. 75(3): p. 1818-1825.

95.   Walus, K., G. Schulhof, and G.A. Jullien. *High Level Exploration of Quantum-Dot Cellular Automata (QCA)*. in *Signals, Systems and Computers, 2004. Conference Record of the Thirty-Eighth Asilomar Conference on*. 2004.

96.   Bryan, M.T., D. Atkinson, and R.P. Cowburn, *Experimental study of the influence of edge roughness on magnetization switching in Permalloy nanostructures.* Applied Physics Letters, 2004. 85(16): p. 3510-3512.

97.   Kikuchi, R., *On the Minimum of Magnetization Reversal Time.* Journal of Applied Physics, 1956. 27(11): p. 1352-1357.